

GROWTH AND STUDIES OF SUPERCONDUCTOR/FERROMAGNETIC HETEROSTRUCTURES

By

Champa Lal Prajapat

(Enroll. No. PHYS01200704007)

Bhabha Atomic Research Centre, Mumbai

Under the guidance of
Prof. G. Ravi Kumar

*A thesis submitted to the
Board of Studies in Physical Sciences
In partial fulfillment of requirements
For the Degree of*

DOCTOR OF PHILOSOPHY

Of

HOMI BHABHA NATIONAL INSTITUTE

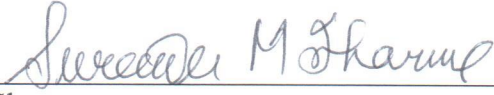


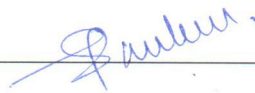
May 2015

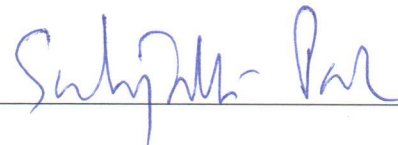
Homi Bhabha National institute

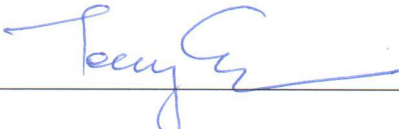
Recommendation of the Viva Voce Board

As members of the Viva Voce Board, we certify that we have read the dissertation prepared by Shri. Champa Lal Prajapat entitled "Growth and studies of superconductor/ferromagnetic heterostructures" and recommended that it may be accepted as fulfilling the dissertation requirement for the Degree of Doctor of Philosophy,


Chairman- Prof. S. M. Sharma Date: 1st May, 2015


Guide- Prof. G. Ravi Kumar Date: 1st May, 2015


External Examiner- Prof. S. Patnaik Date: 1st May, 2015


Member-1: Prof. C. V. Tomy Date: 1st May, 2015

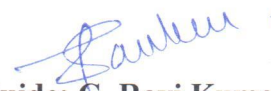

Member-2: Prof. S. M. Yusuf Date: 1st May, 2015

Final approval and acceptance of this dissertation is contingent up on the candidate's submission of the final copies of the dissertation to HBNI.

I hereby certify that I have read this dissertation prepared under my direction and recommend that it may be accepted as fulfilling the dissertation requirement.

Date: 01/05/2015

Place: Mumbai


Guide: G. Ravi Kumar

STATEMENT BY AUTHOR

This dissertation has been submitted in partial fulfillment of requirements for an advanced degree at Homi Bhabha National Institute (HBNI) and is deposited in the Library to be made available to borrowers under rules of the HBNI.

Brief quotations from this dissertation are allowable without special permission, provided that accurate acknowledgement of source is made. Requests for permission for extended quotation from or reproduction of this manuscript in whole or in part may be granted by the Competent Authority of HBNI when in his or her judgment the proposed use of the material is in the interests of scholarship. In all other instances, however, permission must be obtained from the author.

Champa Lal Prajapat

DECLARATION

I, hereby declare that the investigation presented in the thesis has been carried out by me. The work is original and has not been submitted earlier as a whole or in part for a degree/diploma at this or any other Institution/University.

Champa Lal Prajapat

Dedicated to

My Parents

Late Shri Duli Chand Prajapat

Smt. Rameshwari Prajapat

My Wife

Smt. Renuka Prajapat

And

My Daughter and Son

Miss. Saumyaa Prajapat & Advik Prajapat

ACKNOWLEDGEMENTS

First and foremost I would like to express my sincere gratitude to my research guide **Prof. G. Ravi Kumar** (Head, SIRD, BARC) for his valuable guidance and support during the course of this thesis work. I sincerely express my grateful thanks to **Prof. S. K. Gupta**, Head, TPD and **Prof. D. K. Aswal**, TFDS, TPD for their encouragements to finish the thesis within the timeframe. I express my deep gratitude to **Sh. M. R. Singh**, Head, LTPS, TPD for his valuable suggestions in conducting several experiments.

I sincerely thank **Dr. S. Basu**, **Dr. S. Singh**, **Dr. P. U. Sastry** and **Dr. D. Bhattacharya**, SSPD, BARC for helping me in the XRD, XRR and PNR measurements and analyses. I am thankful to **Dr. S. Bhattacharya**, TFDS, TPD and **Dr. M. R. Gonal** for SEM measurements and PLD targets respectively.

I am extremely grateful to **Dr. P. K. Mishra**, **Dr. T. V. C. Rao**, **Dr. H. G. Salunke** and **Dr. D. Karmakar** for their continuous support during the course of the work. I also thank **Sh. V. Dube**, **Sh. K. M. Rajbhoj**, **Sh. S. Gamre** and **Sh. I. B. Thapa** for extending support and help at various stages of the thesis work.

Last but not least, I would like to offer my whole-hearted indebtedness to my **family and friends**, who have always motivated and supported me.

Champa Lal Prajapat

CONTENTS

	Page No.
SYNOPSIS	i
LIST OF PUBLICATIONS	vii
LIST OF FIGURES	ix
LIST OF TABLES	xvii
CHAPTER 1 INTRODUCTION	1
1.1 Introduction to the superconductors	2
1.1.1 Conventional superconductors	2
1.1.2 High T_{SC} superconductors	4
1.2 Introduction to the ferromagnets	8
1.2.1 Metallic ferromagnets	9
1.2.2 Oxide ferromagnets	10
1.3 Antagonistic properties of superconductors and ferromagnets	12
1.4 Techniques for artificial ferromagnetic/superconductor multilayers	14
1.4.1 Molecular beam epitaxy	15
1.4.2 DC and RF Magnetron Sputtering	16
1.4.3 Pulsed Laser Deposition (PLD)	16
1.5 Proximity effects in artificial ferromagnet /superconductor multilayers	17
1.4.1 Metallic multilayers	17
1.4.2 Oxide multilayers	21
1.6 Scope of the thesis work	23

CHAPTER 2	EXPERIMENTAL TECHNIQUES	26
2.1	Introduction	27
2.2	Thin film and multilayer deposition techniques	27
2.2.1	DC magnetron sputtering	27
2.2.2	Pulsed laser deposition system	30
2.3	Structural and morphological characterization	34
2.3.1	X-ray diffraction	34
2.3.2	X-ray and polarized neutron reflectivity	37
2.3.3	Scanning electron microscopy	41
2.4	Transport and magnetic characterization	44
2.4.1	Four-probe resistivity measurement	44
2.4.2	DC magnetization	47
CHAPTER 3	Metallic superconducting/ferromagnetic multilayers: Growth and proximity effects	51
3.1	Introduction	42
3.2	Metallic thin films by DC magnetron sputtering	42
3.2.1	Magnetic thin films	42
3.2.2	Superconducting films	62
3.3	Metallic SC/FM bilayers	67
3.3.1	Ferromagnetic/ non ferromagnetic bilayers	67
3.3.2	Proximity effect in Nb (500 Å)/Ni (500 Å) bilayers	71
3.3.3	Domain wall superconductivity in Nb(500 Å)/Gd(300 Å) bilayers	74
3.4	Proximity effect in NbN/NbO/Co trilayers	81
3.5	Conclusions	84

CHAPTER 4	Oxide superconducting/ferromagnetic heterostructures: Growth and proximity effects	86
4.1	Introduction	87
4.2	Growth of Perovskite manganite films	88
4.2.1	Thin films of $\text{La}_{2/3}\text{Sr}_{1/3}\text{MnO}_3$ (LSMO)	88
4.2.2	Thin films of $\text{La}_{2/3}\text{Ca}_{1/3}\text{MnO}_3$ (LCMO)	102
4.3	Growth of $\text{YBa}_2\text{Cu}_3\text{O}_{7-\delta}$ (YBCO) films	104
4.4	Growth and characterization of LCMO/STO/YBCO heterostructures	106
4.2.1	X-Ray Diffraction	108
4.2.2	X-Ray Reflectivity	110
4.2.3	Magnetic Properties	111
4.5	Investigation of magnetic proximity effect in LCMO/STO/YBCO heterostructures using PNR	112
4.6	Conclusions	121
CHAPTER 5	Summary & Conclusions	122
	Bibliography	128

SYNOPSIS

Ferromagnetism and superconductivity are antagonistic phenomena, which is manifested in their response to a magnetic field i.e. a superconductor expels a magnetic field (Meissner effect), whereas a ferromagnet concentrates the force lines inside its volume (effect of magnetic induction). Ferromagnetism is characterized by an order parameter known as magnetization (i.e. order of spins), whereas the order parameter characterizing the superconductivity is the energy gap corresponding to the formation of singlet spin Cooper pairs (i.e. two electrons of opposite spins and momentum coupled via phonons). This antagonism is understandable from the microscopic theory: attraction between electrons creates Cooper pairs in a singlet state, whereas exchange interaction that produces ferromagnetism, tends to arrange electron spins in parallel to one another. Therefore, when the Zeeman energy of the electrons of a pair in an exchange field I exceeds the coupling energy (i.e. superconducting gap Δ), the superconducting state is destroyed. For the above reasons, the coexistence of the superconducting and ferromagnetic order parameters is unlikely in a uniform system. However, in nature there are few materials, such as, (RE)Rh₄B₄ and (RE)Mo₆X₈ (RE- rare earth, X- S, Se), RuSrGdCu₂O₈, and UGe₂, URhGe etc. in which magnetism and superconductivity coexist. It has been demonstrated that s-pairing superconductivity coexists with antiferromagnetism (e.g. in (RE)Rh₄B₄ and (RE)Mo₆X₈ (RE- rare earth, X- S, Se)), and the triplet-pairing superconductivity coexists with ferromagnetism (e.g. UGe₂, URhGe, RuSrGdCu₂O₈).

In literature, however the coexistence of ferromagnetism and superconductivity has been mainly investigated in artificially prepared ferromagnetic (FM) /superconductor (SC)

heterostructures consisting of alternating FM and SC layers e.g. Fe/Nb/Fe, Nb/Gd, NbN/Co, $\text{YBa}_2\text{Cu}_3\text{O}_{7-\delta}$ (YBCO)/ $\text{La}_{2/3}\text{Ca}_{1/3}\text{MnO}_3$ (LCMO), YBCO/ $\text{La}_{2/3}\text{Sr}_{1/3}\text{MnO}_3$ (LSMO) etc. In these heterostructures, owing to the proximity effect, a superconducting order parameter can be induced in the FM layer; on the other hand, the neighboring pair of FM layers can interact with one another via the SC layer. Such systems have exhibited rich physics: (i) oscillations in superconducting transition temperature with increasing thickness of ferromagnetic layer in three-layer structures (FM/SC/FM), which were ascribed to the appearance of π -phase superconductivity; (ii) in SC/FM/SC trilayer junctions the relative phase is equal to π instead of the usual zero (known as π -junction). It has been observed that the interplay between superconductivity and magnetism can be investigated by growing bilayers and trilayers in controlled manner i.e. the thicknesses of the layers can be varied in controlled manner to change the relative strengths of two order parameters. Therefore, this thesis work is aimed at growth of various FM/SC heterostructures comprising of metallic (Nb/Gd, Nb/Ni and NbN/NbO/Co) and oxide (YBCO/ SrTiO_3 (STO)/LCMO, YBCO/STO/LSMO) multilayers. Our main emphasis was to introduce an insulating layer between superconducting and ferromagnetic layers so that the proximity effect can be controlled. Several new results have been obtained during the thesis work. The thesis is organized into following five chapters.

Chapter 1: Introduction

In this chapter, we begin with a brief overview of metallic (Nb, NbN etc.) and oxide superconductors ($\text{YBa}_2\text{Cu}_3\text{O}_{7-\delta}$) as well as magnetic materials (Fe, Co, Ni, Gd, and

$\text{La}_{2/3}\text{Ca}_{1/3}\text{MnO}_3$). We briefly describe the antagonistic properties of superconductor and ferromagnetism and present some of the natural bulk materials in which both coexist. We describe various methods of growing artificial ferromagnet/superconductor multilayers, such as, molecular beam epitaxy, sputtering, pulsed laser deposition. We review the theoretical and experimental results on the proximity effects in artificial ferromagnetic/superconductor multilayers. The chapter is concluded by bringing out the scope of the thesis work.

Chapter 2: Experimental techniques

This chapter describes the experimental techniques used during the thesis work. The details of DC magnetron sputtering system are described to deposit metallic thin films and multilayers such as Nb/Gd, Nb/Ni and NbN/NbO/Co. The configuration of the pulsed laser deposition (PLD) setup used for deposition of oxide superconductor/ ferromagnetic multilayers like YBCO/STO/LCMO and YBCO/STO/LSMO are presented. An overview of various techniques used for the characterization of thin films and multilayers, such as scanning electron microscopy (SEM), X ray diffraction (XRD), X ray reflectivity (XRR) and polarized neutron reflectivity (PNR) are described. The details of the Superconducting Quantum Interference Device (SQUID) setup used for magnetic measurements are presented. The four probe method used for the electric transport measurements is also described.

Chapter 3: Metallic superconductor/ferromagnetic multilayers: Growth and proximity effects

In this chapter we describe the results on the sputter growth and characterization of following metallic systems: (i) Fe/Au multilayers; (ii) Nb/Gd and Nb/Ni bilayers; and NbN/NbO/Co trilayer.

Fe/Au multilayers were selected to establish the growth of metallic multilayers by DC sputtering. For this purpose two series of Fe/Au multilayers were deposited on Si substrate by sputtering: one series with varying Fe layer thickness, $t_{\text{Fe}} = 30\text{-}100 \text{ \AA}$, and another series with varying Au layer thickness $t_{\text{Au}} = 50\text{-}150 \text{ \AA}$. The multilayer interface structure and magnetic properties investigated by specular x-ray reflectometry and polarized neutron reflectometry indicated their high quality. The results show that magnetoresistance and remnant magnetization increases with increasing thickness of Fe thickness.

Nb (500 \AA)/Gd (300 \AA) bilayers were prepared on Si substrate. Transport measurements revealed a two step superconducting transition, which is attributed to domain wall superconductivity due to the proximity of ferromagnetic Gd. History dependent R-T and V-I characteristics confirmed the domain wall superconductivity. Possible explanation of this observation may be that the superconducting region right below a domain wall exhibits a higher transition temperature compared to the one below a ferromagnetic domain. Nb/Ni bilayers exhibited anomalous V-I characteristics near superconducting transition temperature.

Detailed transport studies were carried out on the trilayer NbN/NbO/Co deposited by sputtering. The sample exhibited superconducting transition at 6.5 K. In the superconducting state, a dip in the resistance was observed at a temperature referred to as T_{MIN} . Below T_{MIN} , resistance reappears, with a magnitude of about 1% of the normal state resistance. The observed resistance is found to decrease on increasing the applied current. A possible reason for re-entrant resistance might be the vortex dynamics in NbN superconducting layer due to the stray fields created by Co layer. A detailed measurement is carried out comparison, the temperature dependent resistance at different currents and the current dependent resistance at different temperatures in close vicinity of T_{SC} .

Chapter 4: Oxide superconductor/ferromagnet heterostructures:

Growth and proximity effects

This chapter deals with a detailed study on growth of thin films of high T_{SC} cuprate superconductor YBCO and perovskite manganite LCMO and/or LSMO and their multilayers by pulsed laser deposition. Results on the growth of YBCO, LCMO and LSMO are presented. A change in magnetic properties by producing strain in different ways like varying the oxygen deposition pressure (P_{O_2}), lattice mismatch with substrate and varying the film thickness in LSMO were studied.

The magnetic proximity effect in YBCO/STO/LCMO multilayers has been investigated by polarized neutron reflectivity (PNR). PNR measurements were carried out across both superconducting and ferromagnetic transitions. We have made a rare observation of the suppression of ferromagnetic order in a LCMO layer which is separated

by insulating STO from YBCO. The PNR analysis suggested an emergence of a thin magnetic “dead” layer in LCMO adjacent to the STO layer below the superconducting transition temperature of the trilayer. The dead layer is seen even for STO layer as thick as 50 Å, suggesting a possible tunneling of the superconducting order parameter through the insulating barrier thereby modifying the magnetic state of LCMO.

Chapter 5: Summary & conclusions

The summary of the thesis work and main conclusions have been presented in this chapter. The chapter is concluded by bring out the future scope.

List of Publications

1. Effect of oxygen partial pressure on the magnetic properties of $\text{La}_{2/3}\text{Sr}_{1/3}\text{MnO}_3$ films grown on SrTiO_3 (111) substrates by pulsed laser deposition, **C. L. Prajapat**, P. Kalita, P. U. Sastry, M. R. Singh, S. K. Gupta and G. Ravikumar, *Physica B* **448** (2014)100.
2. Magnetic properties on strained manganite thin film, **C. L. Prajapat**, M. R. Singh, S. K. Gupta, D. Bhattacharya, S. Basu, and G. Ravikumar, *AIP Conf. Proc.* **1591** (2014) 1624.
3. Depth dependent structure and magnetic properties and their correlation with magnetotransport in Fe/Au multilayers, S. Singh, S. Basu, **C.L. Prajapat**, M. Gupta, A. K. Poswal, D. Bhattacharya, *Thin Solid Films*, **550** (2013) 326.
4. Effect of substrate on magnetic properties of $\text{La}_{2/3}\text{Sr}_{1/3}\text{MnO}_3$ Films, **C. L. Prajapat**, D. Bhattacharya, R. B. Tokas, B. K. Roul, M. R. Singh, P. K. Mishra, S. Basu, S. K. Gupta, and G. Ravikumar *AIP Conf. Proc.* **1512** (2013) 656.
5. Effect of annealing on structure and magneto-transport properties of Fe/Au multilayer, S. Singh, S. Basu, **C.L. Prajapat**, M. Gupta, *AIP Conf. Proc.* **1512** (2013) 730.
6. Observation of Re-entrant Resistance in NbN/NbO/Co Trilayer, **C. L. Prajapat**, G. Yashwant, M. R. Singh, S. K. Gupta, G. Ravikumar, *J. Supercond. Nov. Magn.* **25** (2012) 1455.

7. Magnetic proximity effect in $\text{La}_{2/3}\text{Ca}_{1/3}\text{MnO}_3/\text{SrTiO}_3/\text{YBa}_2\text{Cu}_3\text{O}_{7-\delta}$ heterostructures, **C. L. Prajapat**, S. Singh, A. Paul, D. Bhattacharya, M. R. Singh, G. Ravikumar and S. Basu (under review).
8. Observation of two-step superconducting transition in superconductor-ferromagnet Nb/Gd bilayers - **C.L. Prajapat**, M.R. Singh, S. K. Gupta, and G. Ravikumar (Manuscript under preparation).

List of publication not included in thesis work

1. Magnetic response of ferromagnet-superconductor-ferromagnet(Gd/Nb/Gd) Trilayer, **C.L. Prajapat**, M.R. Singh, S. K. Gupta, and G. Ravikumar *J. Supercond. Nov. Magn.* **27** (2013) 379.
2. Magnetic response of ferromagnet–superconductor bilayers, G. Yashwant, **C.L.Prajapat**, G. Ravikumar, S. Soltan, G. Christiani, H. -U.Habermeier, *J. Magn. Mater.* **324** (2012) 1406.
3. Effect of fast neutron irradiation induced defects on the metamagnetic transition in $\text{Ce}(\text{Fe}_{0.96}\text{Ru}_{0.04})_2$, **C.L. Prajapat**, V. Dube, A. K. Rajarajan, S. V. Thankare, K. C. Jagadeesan, P. K. Mishra, M.R. Singh, S. K. Gupta, and G. Ravikumar, *J. Appl. Phys.* **112** (2012) 063922.

LIST OF FIGURES

Fig.1.1: (a) Schematic of a Cooper pair, (b) Schematic of cooper pair at Fermi surface.

Fig. 1.2: Schematic showing the crystal structure of $\text{YBa}_2\text{Cu}_3\text{O}_6$ and $\text{YBa}_2\text{Cu}_3\text{O}_7$.

Fig. 1.3: (a) Ideal perovskite unit cell showing the oxygen octahedron, (b) Undistorted oxygen octahedron around Mn^{4+} ion and distorted Octahedron around a Mn^{3+} ion. The distortion causes ab -plane contraction (shown by inward arrows) of the Mn-O bond length and along c -axis elongation of Mn-O bond length (shown by outward arrows) (c) The distortion yielding long and short Mn-O bonds in ac -plane.

Fig. 1.4: A schematic diagram of paramagnetic effect of Cooper pair in the presence of exchange field.

Fig. 1.5: Schematic diagram of basic principle of molecular beam epitaxy

Fig. 1.6: Schematic behavior of the superconducting order parameter near the superconductor-normal metal interface. Superconducting order parameter and coherence length in normal are $\psi_N \sim \exp\left(-x/\xi_N\right)$ and coherence length is $\xi_N = \sqrt{\hbar D/kT}$. Here D is the diffusion coefficient of charge carriers and T is temperature.

Fig. 1.7: Schematic behavior of the superconducting order parameter near the superconductor-ferromagnetic metal interface.

Fig. 1.8: Schematic behavior of the superconducting order parameter in SC/FM/SC trilayers in 0 phase and π - phase.

Fig. 1.9: Schematic diagram of FM and AFM coupling in FM/SC/FM trilayers.

Fig. 2.1 Schematic diagram of DC magnetron sputtering system

Fig. 2.2: Photograph of DC sputtering system.

Fig. 2.3: Photograph of the PLD system.

Fig. 2.4: Schematic diagram of the PLD system.

Fig. 2.5: schematic diagram showing how strain affects XRD peaks. (a) Shows relaxed film, (b) Film with uniform strain and (c) Film with non uniform strain.

Fig 2.6: Geometry for specular reflectivity.

Fig. 2.7: Schematics of the polarized neutron reflectometer.

Fig. 2.8: Block diagram of a typical SEM setup.

Fig. 2.9: Interaction of incident electron beam with sample surface.

Fig. 2.10: Photograph of SEM (model: Tescan VEGA MV2300T/40).

Fig. 2.11: Schematic diagram of linear two probe and four probe measurements.

Fig. 2.12: Schematic diagram of temperature control system in MPMS5.

Fig. 2.13: Schematic diagram of measurement unit in MPMS5.

Fig. 3.1: XRR measurements on Co film, open circles and solid line are measured and fitted data, respectively. Inset shows two layer model used for the fitting.

Fig. 3.2: SEM images of the sputter deposited Co films annealed at different temperatures (under a vacuum of 5×10^{-6} mbar for 1 h).

Fig. 3.3 The normalized magnetic moment (m/m_{2kOe}) versus applied field (H) hysteresis loop recorded at 300 K for Co-films annealed at different temperatures T_{an} .

Fig. 3.4: Variation in H_C (10 K and 300 K) for Co-films annealed at different temperatures T_{an} .

Fig. 3.5: H_C variation with temperature for Co films as deposited (open circles) and Annealed at 700 °C (closed circles).

Fig. 3.6: SEM images of Ni films of different thicknesses deposited by sputtering.

Fig. 3.7: The normalized magnetic moment (m/m_s) versus applied field (H) hysteresis loop recorded at 300 K for Ni-films of different thickness. The full hysteresis loop for 20000 Å Ni films is shown in inset.

Fig. 3.8: H_C and S plotted with different thickness of sputtered deposited Ni.

Fig. 3.9: Magnetic moment (m) with temperature (T) is measured in ZFC and FC mode at 100 Oe and 1000 Oe for 300 Å Gd film.

Fig. 3.10: Magnetic moment (m) with applied magnetic field (H) at different temperature for Gd film (300 Å) deposited by sputtering.

Fig. 3.11: Variation in H_C with temperature for Gd film (300 Å) deposited by sputtering.

Fig. 3.12: Superconducting transition transport electrical resistance with temperature in Nb film.

Fig. 3.13: Superconducting transition magnetic moment with temperature in Nb film.

Fig. 3.14: XRD patterns are recorded for all films of NbN (50nm) deposited at different sputtering power from 54 W to 135W.

Fig. 3.15: A temperature dependent resistance is measurement from 4.2 K to 300 K. Inset the superconducting transition.

Fig. 3.16: XRD patterns are recorded for all films of NbN (500 Å) deposited at different substrate temperature T_{Sub} , from room temperature to 800 °C.

Fig. 3.17: Superconducting transition in films of NbN (500 Å) deposited at different substrate temperature T_{Sub} , from room temperature to 800 °C.

Fig. 3.18: (a): Specular X-ray reflectivity measurements from as-deposited multilayer (open circles) and sample annealed at 100°C (open squares) and 150°C (open triangles). (b) shows the normalized SLD profiles at interfaces extracted from fit to XRR data.

Fig 3.19: (a): $M(H)$ hysteresis curves (open circles) and magnetoresistance (open triangles) as function of applied magnetic field for $[\text{Fe}(50 \text{ \AA})/\text{Au}(100 \text{ \AA})]_{10}$ multilayer after annealing at $100 \text{ }^\circ\text{C}$ for one hours. (b): MR vs H for as-deposited (b) and sample annealed at $100 \text{ }^\circ\text{C}$ (c) and $150 \text{ }^\circ\text{C}$ (d).

Fig.3.20: $M(H)$ hysteresis curves for $[\text{Fe}(50 \text{ \AA})/\text{Au}(50 \text{ \AA})]_{10}$ multilayer sample at 5 K (open triangles) and 300 K (open circles). (b): variation of M_r/M_s ratio with thickness of Fe (closed circles) and Au (closed triangles) layers. (c): MR vs H plot for $[\text{Fe}(50 \text{ \AA})/\text{Au}(50 \text{ \AA})]_{10}$. (d): variation of MR with thickness of Fe (closed circles) and Au (closed triangles) layer.

Fig. 3.21: XRR measurement on Nb/Ni bilayers

Fig. 3.22: magnetic moment measured with temperature in ZFC mode at 50 Oe for Nb/Ni bilayers. Inset show the superconducting transition in transport measurements.

Fig. 3.23: The m - H hysteresis loops for the Nb/Ni bilayers were recorded at 10 K ($> T_{\text{SC}}$) and at 5.5 K ($< T_{\text{SC}}$).

Fig. 3.24: Two step V-I curves of Nb/Ni bilayer at different temperatures.

Fig. 3.25: Magnetic moment (m) with temperature (T) is measured in ZFC and FC mode at 100 Oe for bilayers of Nb/Gd.

Fig. 3.26: Magnetic moment (m) with applied field measured at 10 K for bilayers of Nb/Gd.

Fig. 3.27: Superconducting transition in transport electrical resistance measured with increasing temperature from 4.5 K to 10 K for Nb Film and bilayer of Nb/Gd.

Fig. 3.28: Schematic diagram of nucleation of domain wall superconductivity in the Nb layer of Nb/Gd bilayer where ferromagnetic Gd layer have magnetic domains with domain walls.

Fig. 3.29: Field dependent superconducting transition in bilayer of Nb/Gd.

Fig. 3.30: History dependent resistances versus temperature (R-T) curves are recorded with same field (400 Oe) in two different magnetic domains structures.

Fig. 3.31: History dependent Voltage -current (V-I) curves are recorded with same field (400 Oe) in two different magnetic domains structures.

Fig. 3.32: Resistance versus temperature plot of a NbN/NbO/Co trilayer and NbN film measured at applied current of 200 μ A. Inset shows magnetization hysteresis curve measured at 10 K showing ferromagnetic nature of the film.

Fig. 3.33: Temperature dependence of resistance of NbN/NbO/Co trilayers measured at different probe currents.

Fig. 3.34: Schematically diagram of production of vortex and anti vortex in NbN due to stray field of Cobalt layer.

Fig. 4.1: XRD pattern on LSMO film deposited at 1.0 mbar oxygen pressure. Inset shows the enlarged view of (111) doublets of STO and LSMO fitted to lines corresponding to the X-ray source used.

Fig 4.2: (111) peaks of STO/LSMO samples deposited under different P_{O_2} . Arrow shows the peak position.

Fig. 4.3: FC and ZFC m (normalized by $m(T=5\text{ K})$) vs T data in 100 Oe field. T_{FM} is marked by an arrow.

Fig. 4.4: $m(T)$ normalized by field cooled moment at 5K vs T/ T_{FM} for different films.

Fig. 4.5: $m - H$ loops measured at 5K for different values of P_{O_2} .

Fig.4.6: XRD pattern of 500Å LSMO thin films on a) STO(100), b) MgO(100) and c) YBCO substrates.

Fig. 4.7: ZFC and FC m vs T in a field of 100 Oe. T_{FM} is marked by arrow.

Fig. 4.8: $m - H$ loops measured at 100 K for different LSMO films on different substrates.

Fig. 4.9: H_C vs T in LSMO films deposited on different substrates.

Fig.4.10: XRR patterns of LSMO films with different thickness on MgO (100) substrates.

Fig.4.11: XRD pattern of LSMO films with different thickness on a) MgO(100) and b) STO(100) substrates.

Fig.4.12: Non uniform strain with LSMO thickness on MgO(100) substrates.

Fig.4.13: m vs T for LSMO film of different thickness on MgO Substrate.

Fig. 4.14: $m - H$ loops measured at 5K for LSMO film with different thicknesses on a) STO(100) and b) MgO(100) substrates.

Fig. 4.15: Variation in H_C with LSMO film thickness deposited on STO(100) and MgO(100) substrates.

Fig. 4.16: XRR pattern of LCMO film with on MgO (100) substrates.

Fig. 4.17: ZFC and FC m vs T of LCMO films on STO (100) and MgO (100) substrates.

Fig. 4.18: XRD pattern of YBCO films on MgO (100) and STO (100) substrates.

Fig. 4.19: XRR pattern of YBCO film with on MgO (100) substrates.

Fig. 4.20: Superconducting transition on YBCO film on STO (100) substrates.

Fig. 4.21: X-ray diffraction data from STO/YBCO bilayer on STO (100) substrate.

Fig. 4.22: X-ray reflectivity (XRR) pattern from STO/YBCO heterostructures. Inset show the corresponding thickness and roughness of each layer which gave best fit to XRR data.

Fig. 4.23: X-ray diffraction data from LCMO/STO/YBCO trilayer on STO (100) substrate.

Fig. 4.24: X-ray reflectivity (XRR) pattern from two heterostructures LCMO (300 Å)/STO (25 Å)/YBCO (300 Å) and LCMO (200 Å)/STO (50 Å)/YBCO (200 Å).

Fig. 4.25: FC Magnetization of LCMO (300 Å)/STO (25 Å)/YBCO (300 Å) trilayer in 300 Oe field showing the FM transition at around 130 K. Inset show ZFC showing $T_{SC} \sim 60$ K.

Fig. 4.26: (a) Polarized neutron reflectivity (PNR) measurements and their modeling. a, PNR (spin up, R^+ and spin down, R^-) data from the LCMO (300 Å)/STO (25 Å)/YBCO (300 Å) trilayer at 300 K and 10 K. Reflectivity data at different temperature are shifted by a factor of 20 for the sake of clarity. (b) Spin difference ($R^+ - R^-$) data at 300 K (upper panel) and 10 K (lower panel). (c) Nuclear scattering length density (SLD) depth profile extracted from fitting PNR data at 300 K as shown in a, b. (d) Magnetization (M) depth profile corresponding to PNR data shown in (a) and (b). Two magnetization models, with and without magnetic dead (MD) layer at LCMO/STO interface, at 10 K are depicted in d and the corresponding fits to PNR data are shown in b (lower panel).

Fig. 4.27: (a) PNR (spin up, R^+ and spin down, R^-) data from the LCMO (300 Å)/STO (25 Å)/YBCO (300 Å) sample at 10 K. upper panel show the spin difference ($R^+ - R^-$) data at 10 K. (b) shows the corresponding magnetization depth profiles which fitted PNR data at 10 K.

Fig. 4.28: Polarized neutron reflectivity (PNR) measurements and their modeling across superconducting transition temperature. (a) Spin difference ($R^+ - R^-$) data the LCMO (300 Å)/STO (25 Å)/YBCO (300 Å) sample at 100 K (upper panel) and 50 K (lower panel). (b) Magnetization (M) depth profile at 100 K (upper panel) and 50 K (lower panel)

corresponding to spin difference data shown in a. Two magnetization models at 100 K are depicted in the upper panel of (b) and the corresponding fits to PNR data are shown in upper panel of (a).

Fig. 4.29: Polarized neutron reflectivity (PNR) measurements and their modeling from the sample with double thickness of insulator layer. (a) Spin difference data from the LCMO (200 Å)/STO (50 Å)/ YBCO (200 Å) trilayer at 300 K (upper panel) and 10 K (lower panel). (b) Nuclear scattering length density (NSLD) depth profile (upper panel) and magnetization depth profile (lower panel) extracted from fitting PNR data at 300 K and 10 K as shown in a. Two magnetization models at 10 K are depicted in the lower panel of (b) and the corresponding fits to PNR data are shown in lower panel of (a).

Fig. 4.30: Variation of magnetization (M) as a function of temperature for field cooled condition in a magnetic field of 300 Oe using SQUID (open circle) and PNR (open star) for LCMO (300 Å)/STO (25 Å)/YBCO (300 Å) trilayer.

Fig. 4.31: Fitting of magnetization depth profile of $\text{YBa}_2\text{Cu}_3\text{O}_{7-\delta}$ (300 Å)/ SrTiO_3 (25 Å)/ $\text{La}_{2/3}\text{Ca}_{1/3}\text{MnO}_3$ (300 Å) sample at 10 K obtained from PNR data using Eq. 4.1.

LIST OF TABLES

Table 1.1 Selected conventional type-I superconductors and their T_{SC} .

Table 1.2 Selected conventional type-II superconductors and their T_{SC} .

Table 1.3 Important HTSC cuprate systems and their T_{SC} .

Table 1.4 The characteristic parameters of YBCO

Table 1.5 Properties of elemental ferromagnets.

Table 1.6 Oxide ferromagnetic materials and their maximum T_{FM}

Table 1.7 Coexistence of magnetism and superconductivity in bulk materials.

Table 2.1: Salient features of DC magnetron sputtering system.

Table 2.2: Salient features of PLD system set-up at TPD, BARC.

Table 4.1: Parameters obtained from XRR measurements on YBCO/STO/LCMO heterostructures.

Introduction

1.1 Superconductivity

The phenomenon of superconductivity in which the electrical resistivity of a material abruptly drops to zero below a critical temperature was first discovered in Hg by Kamerlingh Onnes in 1911 [1]. The temperature at which resistance drops to zero is the superconducting transition temperature T_{SC} , a characteristic feature of all superconductors. Another fundamental property of the superconducting state was discovered in 1933 when Walther Meissner and Robert Ochsenfeld [2] demonstrated that superconductors exhibit *perfect diamagnetism* below T_{SC} , i.e. they expel the magnetic field, the effect known as Meissner effect. Till date several materials are found to exhibit superconductivity, which can broadly be classified into two categories: conventional and high-temperature superconductors.

1.1.1 Conventional superconductors

Conventional superconductors are essentially metallic and metallic compounds or alloys. These superconductors based on their response to applied magnetic field are classified into Type-I (a single critical magnetic field) and Type-II (exhibit a mixed state with two critical magnetic fields) as summarized in Table 1.1 and Table 1.2 respectively. Type-I superconductors are characterized by the inequality $\lambda < \xi / \sqrt{2}$, while for Type-II superconductors $\lambda > \xi / \sqrt{2}$, where λ and ξ are the magnetic penetration depth and coherence length respectively. Among these, type-II superconductors such as Nb is employed for

accelerator RF cavities and NbTi and Nb₃Sn are extensively used in high magnetic field applications. Nb in thin film form is also used for making SQUIDs.

Table 1.1 Selected conventional type-I superconductors and their T_{SC}

System	Maximum T_{SC}
Pb	7.2 K
Hg	4.2 K
Sn	3.7 K
Al	1.2 K
Mo	0.9 K
W	0.02 K

Table 1.2 Selected conventional type-II superconductors and their T_{SC}

System	Maximum T_{SC}
V	5.4 K
Tc	7.8 K
Nb	9.2 K
NbTi	10.0 K
Nb ₃ Sn	18.0 K
NbN	16.5 K
Nb ₃ Ge	23.1 K
MgB ₂	39.0 K

The mechanism of superconductivity was theoretically established by Bardeen, Cooper and Schrieffer (BCS) in 1957 [3]. The basis of this theory is that conduction electron of a given momentum and spin gets weakly coupled to another electron of the opposite momentum and spin into pairs (i.e. $\mathbf{k}\uparrow, -\mathbf{k}\downarrow$) through an attractive interaction mediated by phonons, known as *Cooper pairs* as shown in Fig. 1.1. Cooper pairs are

pseudo Bosons and can flow without any dissipation. The formation of the bound states creates instability in the ground state of the Fermi sea of electrons resulting in energy gap $\Delta(T)$ opening up at the Fermi level. The minimum energy E_g required to break a Cooper pair to create two quasi-particle excitations is $E_g = 2\Delta(T)$. Within BCS theory, zero temperature energy gap is given as

$$\Delta(0) = 2 \cdot \hbar \omega_D \cdot e^{-\frac{1}{N(0) \cdot V}}$$

where $N(0)$ is density of states at Fermi level, V - Interaction potential, ω_D is Debye frequency.

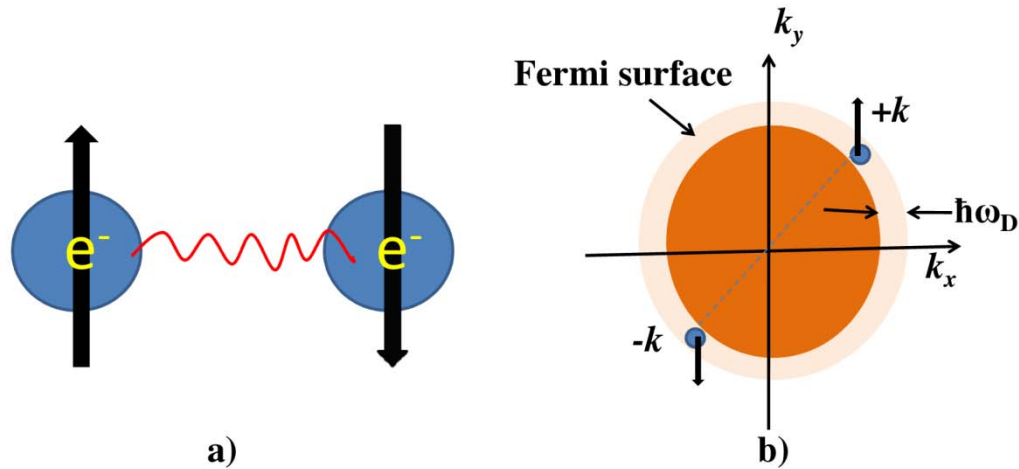


Fig.1.1: (a) Schematic of a Cooper pair, (b) Schematic of cooper pair at Fermi surface

1.1.2 High temperature superconductors

Bednorz and Muller in 1986 discovered superconductivity in La-Ba-Cu-O at a temperature 29 K in, for which they were awarded Nobel Prize in 1987 [4]. Soon it was

followed by the discovery of superconductivity in $\text{YBa}_2\text{Cu}_3\text{O}_7$ at around 90 K. As shown in Table 1.3, highest T_{SC} achieved in cuprates was 135 K. These cuprate superconductors are known as High Temperature Superconductors (HTSC). The large value of T_{SC} in cuprates implied that the mechanism of superconductivity might be different from that in the conventional phonon-mediated electron pairing of BCS type superconductors. Possibility of applications at liquid nitrogen temperature (77 K) prompted fabrication of HTSCs in different forms such as discs, wires, tapes, thin films, etc. However, progress on developing commercial devices is somewhat slow owing to various material issues.

Table 1.3: Important HTSC cuprate systems and their T_{SC}

System	Maximum T_{SC}
$(\text{La}_{1-x}\text{Sr}_x)_2\text{CuO}_4$	37 K [5]
$\text{YBa}_2\text{Cu}_3\text{O}_7$	92 K [6]
$\text{YBa}_2\text{Cu}_4\text{O}_8$	80 K [7]
$\text{Bi}_2\text{Sr}_2\text{Ca}_1\text{Cu}_2\text{O}_6$	84 K [5]
$\text{Bi}_2\text{Sr}_2\text{Ca}_2\text{Cu}_3\text{O}_{10}$	110 K [5]
$\text{Tl}_2\text{Ba}_2\text{Ca}_2\text{Cu}_3\text{O}_{10-\delta}$	128 K [8]
$\text{Hg Ba}_2\text{Ca}_2\text{Cu}_3\text{O}_8$	135 K [9]

As shown in Table 1.3, cuprate superconductors are available in a series of compounds based on Y, Bi, Tl, and Hg. Among these, $\text{YBa}_2\text{Cu}_3\text{O}_{7-\delta}$ (YBCO) system is one of the most studied as it has the least anisotropy. The crystal structure of YBCO depends on the oxygen content. The crystal structures for oxygen contents equal to 6 and 7 are shown in Fig. 1.2. The salient feature of the YBCO crystal structure is that it is composed

of three perovskite unit cells (SrTiO_3 -type) stacked along the c -axis. In the first and third cells Ba is the body-centered atom, while in the second cell it is Y atom. The Ti atoms of perovskite structures are replaced by Cu, which forms CuO_2 layers or planes with two oxygen atoms per Cu.

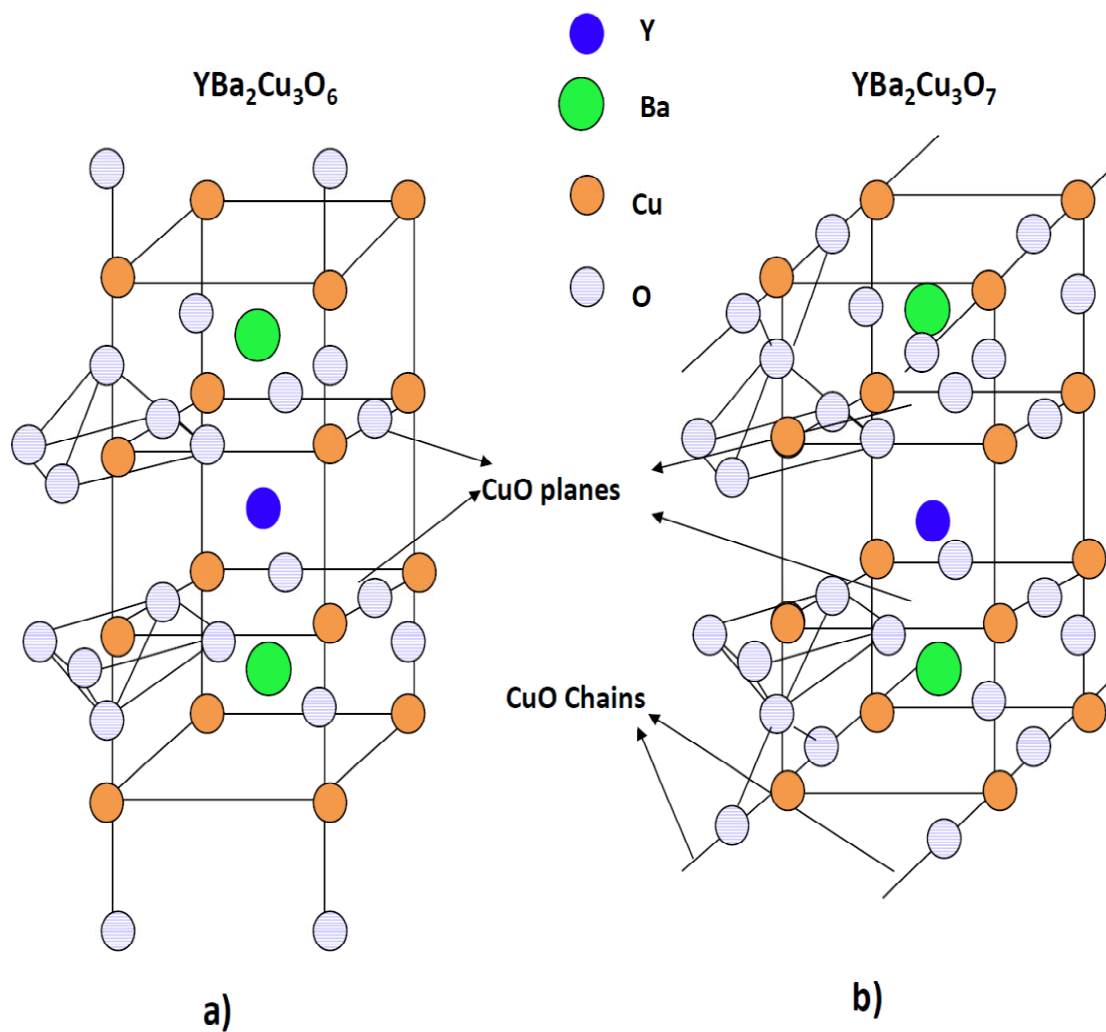


Fig. 1.2: Schematic showing the crystal structure of $\text{YBa}_2\text{Cu}_3\text{O}_6$ and $\text{YBa}_2\text{Cu}_3\text{O}_7$.

The presence of CuO₂ layers - known to be responsible for superconductivity - is a key feature in all HTSC compounds. Thus, all HTSC compounds exhibit a uniform lattice size in *ab*-plane. However, the lattice size along *c*-axis depends upon the number of CuO₂ layers.

Table 1.4: The characteristic parameters YBCO

Physical Parameter		Value
Coherence length	ξ_{ab}	15 Å
	ξ_c	3 Å
Penetration depth	λ_{ab}	1400 Å
	λ_c	7000 Å
G-L ratio ($\kappa = \lambda / \xi$)	κ_{ab}	~ 90
	κ_c	~ 2300
Lower critical field	H_{c1ab}	~ 20 mT
	H_{c1c}	~100 mT
Gap parameter	$(2\Delta/kT)_{ab}$	~ 6 meV
	$(2\Delta/kT)_c$	~ 3.6 meV

The lattice parameter and the crystal structure of YBa₂Cu₃O_{6+ δ} depend on oxygen content (δ). For $\delta = 0$ i.e. YBa₂Cu₃O₆, the crystal structure is tetragonal with lattice parameters $a = b = 3.86$ Å and $c = 11.816$ Å. As δ increases, a tetragonal - to - orthorhombic transition takes place around $\delta = 0.35$. The additional oxygen is

accommodated in the form of Cu-O chains as shown Fig. 1.2(b). For fully oxygenated $\text{YBa}_2\text{Cu}_3\text{O}_7$ i.e. $\delta = 1$, lattice parameters of the orthorhombic structure are $a = 3.8227$, $b = 3.8872$ and $c = 11.6802$ Å [10]. Owing to layered crystal structure HTSC compounds are anisotropic in character. The T_{SC} of YBCO strongly depends on the oxygen content. For $6 < \delta < 6.4$ the material is insulating. The T_{SC} increases rapidly to 60 K as the δ increases from 6.4 to 6.5 and remains constant for δ in the range of 6.5 to 6.7. The T_{SC} further increases to 92 K for $\delta > 6.9$. The characteristics parameters YBCO are anisotropic owing to its crystal structure and their typical values are summarized in Table 1.4.

A large value for the ratio λ/ξ , as seen from Table 1.4, suggests YBCO is an extreme Type-II superconductor. The value of $2\Delta/kT_{SC}$ measured along the c-axis matches well with the BCS value of 3.5. However, $2\Delta/kT_{SC}$ along ab -plane is much higher and cannot be accounted by BCS theory. The value of $\Delta C/\gamma T_{SC}$ obtained from the specific heat measurements matches well with the value of 1.43 given by BCS theory [3].

1.2 Introduction to the Ferromagnetic Materials

Ferromagnetic materials are characterized by spontaneous magnetization below Curie temperature T_{FM} . In order to minimize magnetic energy, a ferromagnet breaks up into macroscopic domains, over which magnetization is uniform and is a characteristic of the ferromagnet. Ferromagnetic materials are broadly categorized as metallic and oxide ferromagnetic materials.

1.2.2 Metallic ferromagnetic materials

Traditionally ferromagnetism has been observed in metallic systems, which has been understood by the phenomenological theories (a) the Curie-Weiss localized-moment theory [11] and (b) the Stoner band theory of ferromagnetism [12]. During the last few decades ferromagnetism has also been observed in the oxide systems. A list of metallic ferromagnets, their T_{FM} and saturation magnetization M_S are given in Table 1.5. In this thesis, we study effect of ferromagnetic domain structure of a metallic ferromagnetic film deposited on superconducting film on the transport properties in the superconducting state of the bilayer. Essentially, the magnetic flux emanating from the domain boundaries of the ferromagnetic film crucially influences the transport behavior of the superconducting film. Further, there exists a possibility of the domain walls acting as pinning centers for the vortices in the underlying superconducting film. We discuss such issues in detail in chapter 3.

Table 1.5 Properties of elemental ferromagnets.

Element	T_{FM}	M_S
Co	1388 K	1.72 μ_B
Fe	1043 K	2.22 μ_B
Ni	637 K	0.61 μ_B
Gd	293 K	7.63 μ_B
Dy	88 K	10.2 μ_B

Weiss postulated a strong internal “molecular field” in ferromagnets, which acts to align the magnetic moments. The molecular field originates from the quantum mechanical exchange energy that causes electrons with parallel spins to have a lower energy than those with anti-parallel spins. Below T_{FM} , the molecular field is strong enough to magnetize the substance even without any applied external field. However, this theory is unable to account for the measured values of the magnetic moment per atom in some ferromagnetic materials accurately. Band theory of ferromagnetism proposed by Stoner successfully accounts for the magnetic moments in various ferromagnetic materials.

1.2.2 Oxide ferromagnetic materials

The discovery of high-temperature superconductivity in cuprates has strongly renewed the interest in magnetic oxides. A large part of recent studies has been devoted to the mixed-valence manganese oxides exhibiting a metal–insulator transition accompanied by the so-called colossal magnetoresistance (CMR) effects [13, 14]. These oxides have a rich and complex physics related to the predominance of electron-lattice and electron–electron interactions. Their structural, magnetic and transport properties are intricately related. In addition, the CMR effects and the occurrence of metallic phases with a fully spin-polarized conduction band are promising for applications. It is therefore necessary to master the growth of high quality thin films with well controlled tailored properties. Progress in the growth of epitaxial thin films opens the way to all oxide or oxide-metal and ferromagnetic oxide – superconducting oxide devices. Historically, the mixed-valence perovskites $\text{La}_{1-x}\text{A}_x\text{MnO}_3$ ($\text{A} = \text{Ca}, \text{Sr}, \text{Ba}$) were studied in the fifties [15, 16].

The compounds of the form $R_{1-x}A_xMnO_3$ fall in the class of distorted ABO_3 type perovskites, as schematically shown in Fig. 1.3 a. The distortion of the ideal perovskite cell is caused by the mismatch between the sizes of the A and B site cations (Fig. 1.3 b). In $R_{1-x}A_xMnO_3$, the Mn-O-Mn bonds form a three dimensional network, with Mn ion sitting inside the oxygen octahedron (Fig. 1.3 c).

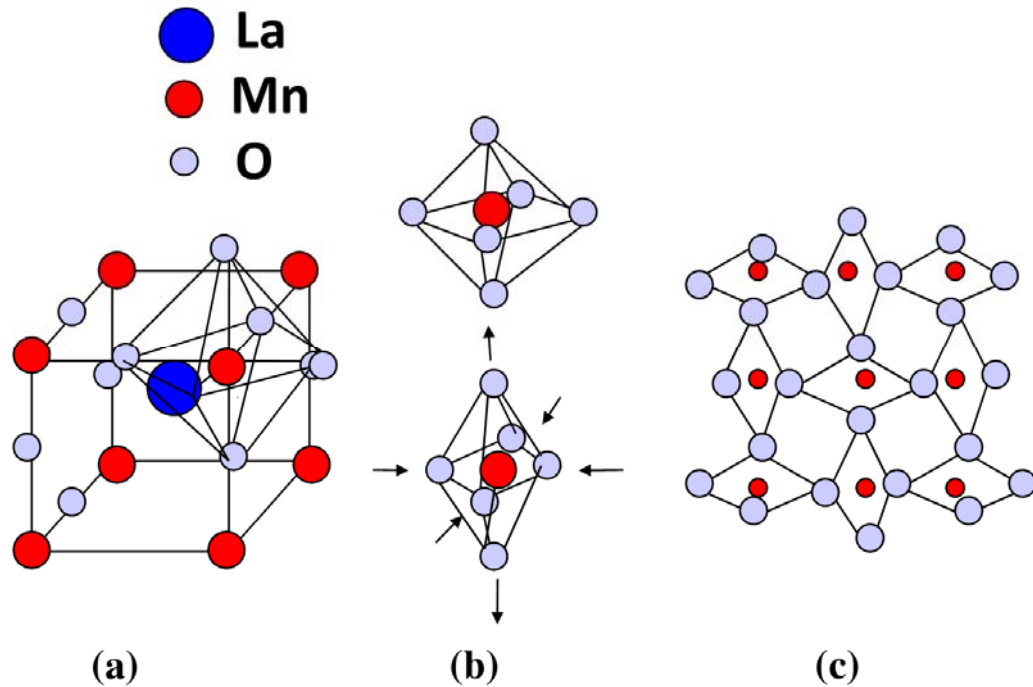


Fig. 1.3: (a) Ideal perovskite unit cell showing the oxygen octahedron, (b) Undistorted oxygen octahedron around Mn^{4+} ion and distorted Octahedron around a Mn^{3+} ion. The distortion causes ab -plane contraction (shown by inward arrows) of the Mn-O bond length and along c -axis elongation of Mn-O bond length (shown by outward arrows) (c) The distortion yielding long and short Mn-O bonds in ac -plane.

These materials exhibit antiferromagnetic behavior for low and high values of x and ferromagnetic behavior in some range of x around 0.33. A list of commonly known

oxide ferromagnets along with their maximum T_{FM} are given in Table 1.4. Among these, $\text{La}_{1-x}\text{A}_x\text{MnO}_3$ ($\text{A}=\text{Ca}^{2+}, \text{Sr}^{2+}$) is interesting as the lattice parameters in the ab plane are close to those of YBCO thus enabling preparation of epitaxial multilayers such as LCMO/YBCO. Further epitaxial bilayers and trilayers with very high quality interfaces employing manganites and YBCO are ideal candidates to study coexistence and interaction of ferromagnetic and superconducting orders in artificial structures. Studies on these structures are presented in chapter 4.

Table 1.4 Properties of oxide ferromagnetic materials

Compound	$T_{FM}(\text{maximum})$
CrO_2	386 K
Fe_3O_4	858 K
$\text{La}_{1-x}\text{Ca}_x\text{MnO}_3$	270 K
$\text{La}_{1-x}\text{Sr}_x\text{MnO}_3$	350 K
$\text{Y}_3\text{Fe}_5\text{O}_{12}$	560 K

1.3 Coexistence of superconductivity and magnetism

Superconductivity and ferromagnetism are distinct, mutually antagonistic ordered states. As discussed in Section 1.2, superconductivity is based on attractive interaction between electrons of opposite spin (singlet pair). Ferromagnetic exchange field tends to break up the singlet pairs by aligning the spins (Fig. 1.4). However, study for coexistence of magnetism and superconductivity has been being pursued for decades.

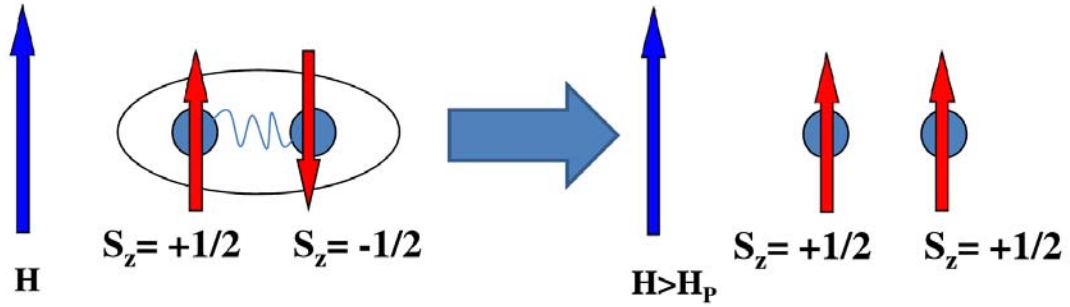


Fig. 1.4: A schematic diagram of paramagnetic effect of Cooper pair in the presence of exchange field.

Table 1.5 Coexistence of magnetism and superconductivity in bulk material [17-18]

Bulk Material	Superconductivity	Magnetism	Remarks
NdRh ₄ B ₄	Singlet SC (< 5.3 K)	AFM (< 1.3 K)	
TmRh ₄ B ₄	Singlet SC (< 9.8 K)	AFM (< 0.4 K)	
ErRh ₄ B ₄	SC (< 8.7K, & < 0.7K)	AFM (< 0.8 K)	Re-entrant SC < 0.7K
GdMo ₆ S ₈	Singlet SC (< 1.4 K)	AFM (< 0.8 K)	
DyMo ₆ S ₈	Singlet SC (< 2 K)	AFM (< 0.4 K)	
ErMo ₆ S ₈	Singlet SC (< 2.2 K)	AFM (< 0.2 K)	
HoMo ₆ S ₈	SC (< 1.8K, & < 0.7K)	AFM (< 0.74 K)	Re-entrant SC < 0.7K
GdMo ₆ Se ₈	Singlet SC (< 5.6 K)	AFM (< 0.8 K)	
ErMo ₆ Se ₈	Singlet SC (< 6 K)	AFM (< 1.1 K)	
ErNi ₂ B ₂ C	Singlet SC (< 10.5 K)	AFM (< 6.8 K)	
TmNi ₂ B ₂ C	Singlet SC (< 11 K)	AFM (< 1.5 K)	
HoNi ₂ B ₂ C	Singlet SC (< 8 K)	AFM (< 5 K)	
URhGe	Triplet SC (< 0.3 K)	FM (< 9.5 K)	
UGe ₂	Triplet SC (< 0.4 K)	FM	
Sm _{1.85} Ce _{0.15} CuO ₄	SC (< 23.5)	FM in layers	Natural FM/SC multilayer System
RuSr ₂ GdCu ₂ O ₈	SC (~30-50K)	Weak FM	Natural FM/SC multilayer System

A large family of materials (Table 1.5) were discovered where superconductivity and magnetism cohabit. There exist several compounds where superconductivity coexists with antiferromagnetism (AFM) as the exchange field averaged over superconducting coherence length is zero. However, coexistence of ferromagnetism and superconductivity is rather rare. Some compounds such as UGe_2 and UGeRh which are ferromagnetic (FM) but support a rare phenomenon of superconductivity based on triplet pairing. Even where they exist, it has been seen that these two orders are spatially separated in the layered lattice structure as in the case of $\text{Sm}_{1.85}\text{Ce}_{0.15}\text{CuO}_4$ and $\text{RuSr}_2\text{GdCu}_2\text{O}_8$. In these systems the relative strength of the superconducting and ferromagnetic orders is predetermined by the separation between the FM and SC sub-lattice structures. These limitations can be easily overcome in artificial heterostructures where there is freedom of choice of materials and their individual layer thicknesses. Advancement of thin film technology has made it possible to prepare high quality artificially layered epitaxial structures involving ferromagnetic manganites and superconducting cuprates. In the next section we briefly discuss some of the thin film and multilayer deposition techniques employed for these studies.

1.4 Artificial ferromagnet/superconductor multilayer deposition

In this section, basic concepts of some of the techniques such as, molecular beam epitaxy, sputtering, and pulsed laser deposition used for the growth of artificial ferromagnet/superconductor multilayers are presented.

1.4.1 Molecular beam epitaxy

Molecular Beam Epitaxy (MBE) is carried out in ultra high vacuum (UHV), to grow high quality epitaxial structures with monolayer (ML) control. MBE technique is widely used techniques for producing metallic as well as insulating epitaxial layers. The principle underlying MBE growth is relatively simple: atoms or clusters of atoms, which are produced by heating up a solid source are allowed to migrate and impinge on a hot substrate surface, where they can diffuse and eventually incorporate into the growing film. A schematic diagram of MBE is shown in Fig. 1.5. The conceptual of the technique is very simple but it requires great effort to produce high quality epitaxial structures.

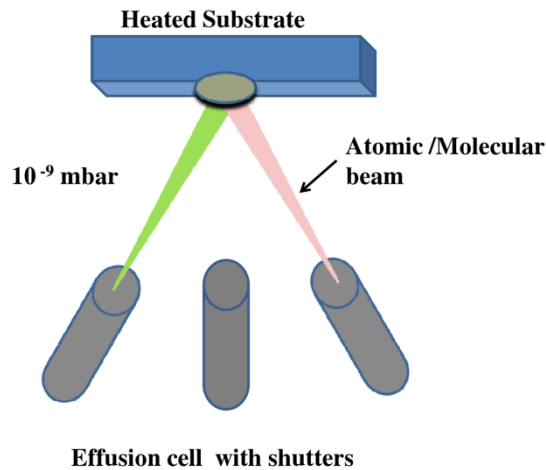


Fig. 1.5: Schematic diagram of basic principle of molecular beam epitaxy.

For beam type feature for the molecules evaporated from a source requires that the mean free path (λ) of the molecules is much larger than the source-to substrate distance. λ increases with decreasing pressure (P) in vacuum chamber i.e. improving by

vacuum thus high vacuum of 10^{-9} mbar order is required. Other than high vacuum, main key component is effusion cells because it must provide excellent flux stability and uniformity, material purity the highest temperatures (up to 1400°C) for the longest periods.

1.4.2 DC and RF Magnetron Sputtering

Sputtering is process in usually argon ions (Ar^+) are accelerated towards a target consisting of the material to be deposited. To accelerate the positive ions towards the targets, a negative DC or RF potential is applied to target. The value of potential can vary the acceleration rate. Material is sputtered from the target due to collision of ions with target atoms and afterwards deposited on a substrate in the vicinity. The process is realized in a closed chamber, which is pumped down to a vacuum base pressure before deposition starts. Initially, to enable the ignition of plasma usually argon is fed into the chamber up to a pressure ranging between 0 to 10^{-2} mbar. In Ar gas there is always some ionized Ar^+ ions available due to natural cosmic radiation. Further ions are generated by electrons-Ar atoms collisions. This technique is suitable for preparation of metallic multilayers, and further details are presented in Chapter 2.

1.4.3 Pulsed Laser Deposition (PLD)

Pulsed laser deposition (PLD) is simple and versatile experimental method that is widely used in the areas of thin film deposition and multi-layer research. In this technique, a UV pulsed laser beam is focused onto the surface of a solid target of interest. Due to

intense energy absorption in short area of target (few J/cm^2) with short duration (order of few tens of nanosecond), the solid surface of target leads to rapid evaporation of the target materials which raised surface temperature up to few thousand K. The evaporated materials consist of highly excited and ionized species. A glowing plasma plume is immediately generated in front of the target surface. PLD can be carried out in vacuum as well as in presence of some dilute background reactive gas i.e. O_2 , N_2 , etc, which is used for modification of the composition of the thin films. This technique is very suitable for oxide multilayers and is described in Chapter 2.

1.5 Proximity effects in artificial ferromagnet/superconductor multilayers

1.5.1 Metallic SC/FM multilayers

Let us first see what happens at the SC/N (N is normal metal) interface. In this case, Cooper pairs from superconductor diffuse into normal metal and induce superconductivity, a phenomenon known as proximity effect. At the same time, superconductivity weakens in the superconductor near the interface due to leakage of Cooper pairs. A decrease of the superconducting transition temperature T_{SC} in a thin superconducting layer in contact with a normal metal was studied in early 1960 [19]. T_{SC} was observed to decrease with increasing thickness of normal metal in SC/N bilayer. Further, for the thickness of the superconducting layer smaller than a critical value, T_{SC} is totally suppressed [20].

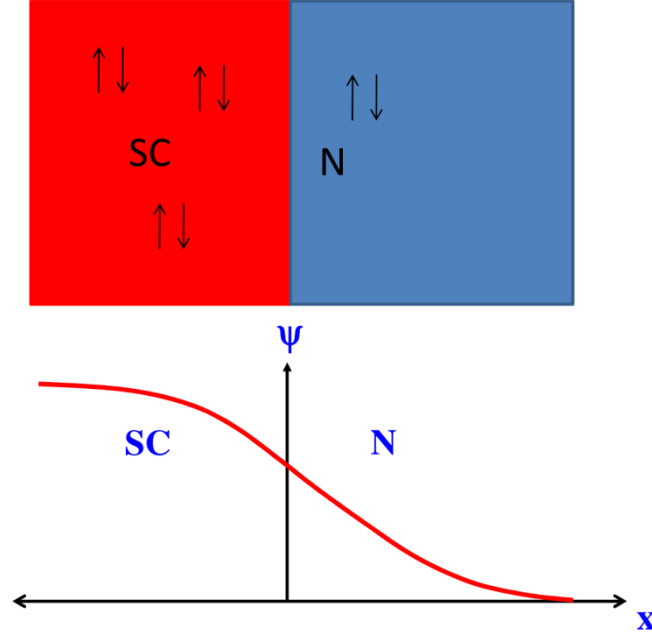


Fig. 1.6: Schematic behavior of the superconducting order parameter near the superconductor-normal metal interface. Superconducting order parameter and coherence length in normal are $\psi_N \sim \exp(-x/\xi_N)$ and coherence length is $\xi_N = \sqrt{\hbar D/kT}$. Here D is the diffusion coefficient of charge carriers and T is temperature.

Superconducting order parameter in the normal metal obeys the relation $\psi_N \sim \exp(-x/\xi_N)$ where $\xi_N = \sqrt{\hbar D/kT}$ is the coherence length determined by the diffusion coefficient of charge carriers in the metal (D) and temperature (T) as schematically shown in Fig. 1.6. This change in order parameter across the interface is continuous if potential barrier is absent.

When the normal metal is replaced by ferromagnetic metal, superconducting order parameter not only decays but exhibits oscillatory behaviour in the ferromagnet as shown in Fig. 1.7. When a Cooper pairs encounters the exchange field H_{EX} in the ferromagnet it

acquires a net momentum proportional to H_{EX} . For the total momentum to be conserved, probability of a pair with a net momentum \mathbf{p} and $-\mathbf{p}$ are the same. A linear superposition of the pair wave functions of opposite momenta gives rise to oscillatory behaviour of the order parameter. In addition, the decay of the order parameter is again governed by diffusion coefficient D and the exchange energy H_{EX} as given by $\xi_{FM} = \sqrt{\hbar D / H_{ex}}$. This phenomenon is responsible for the non-monotonic behavior of T_{SC} as a function of the thickness of the ferromagnetic layer in SC/FM multilayers [21-24]. Such an oscillatory behavior is also observed in bilayers of Nb/Ni [25], trilayers of Fe/Nb/Fe [26], Fe/V/Fe [27] and Fe/Pb/Fe [28].

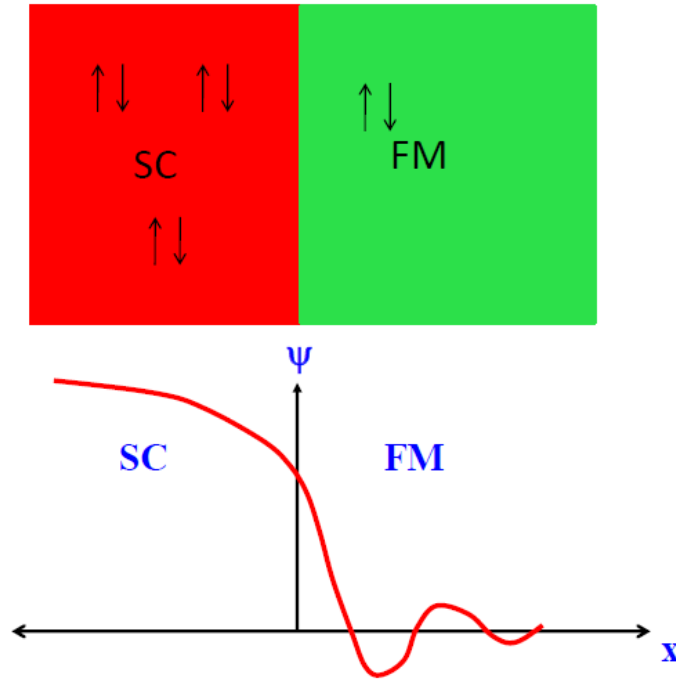


Fig. 1.7: Schematic behavior of the superconducting order parameter near the superconductor-ferromagnetic metal interface.

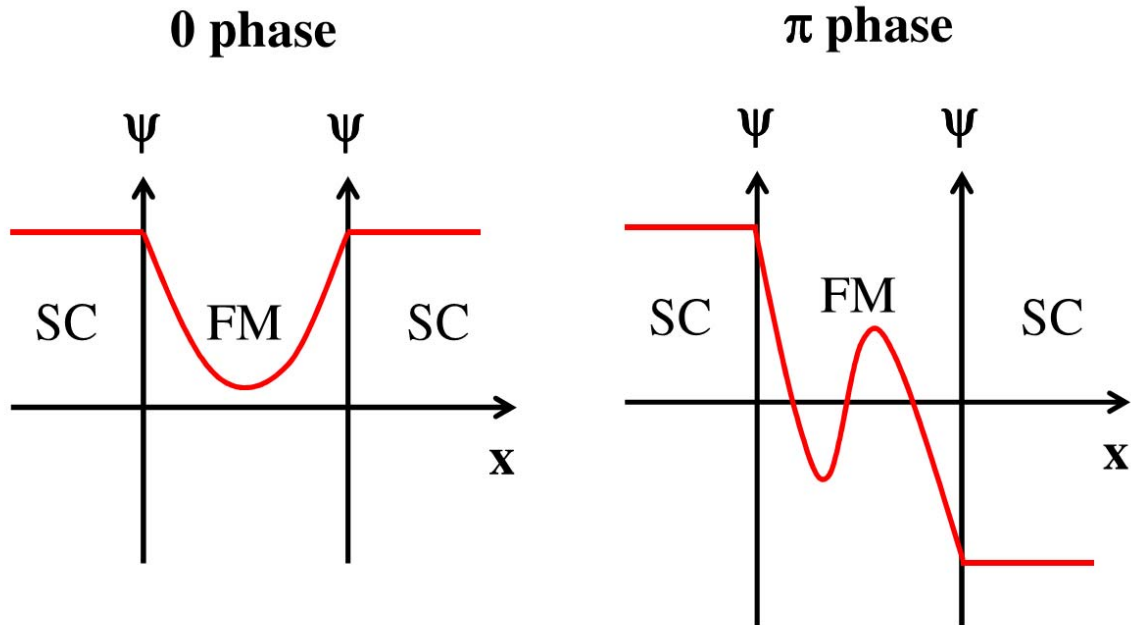


Fig. 1.8: Schematic behavior of the superconducting order parameter in SC/FM/SC trilayers in 0 phase and π - phase.

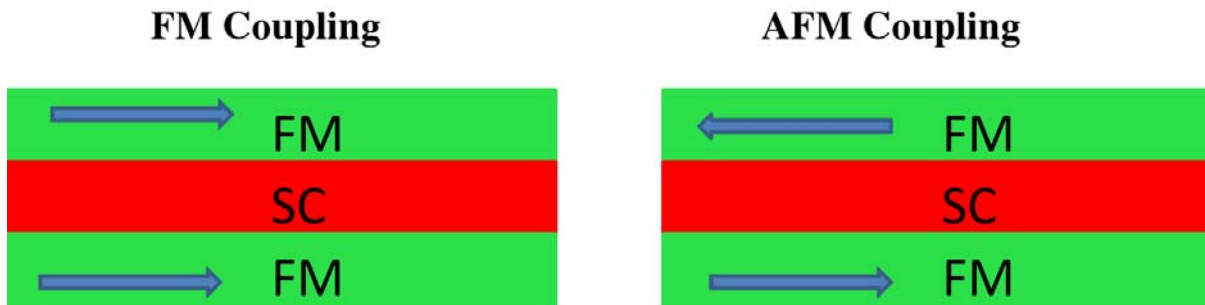


Fig. 1.9: Schematic diagram of FM and AFM coupling in FM/SC/FM trilayers.

In SC/FM/SC trilayer, depending on the thickness of the FM layer, there is possibility to couple the two SC layers with either zero-phase difference or π - phase difference as shown in Fig 1.8.

On the other hand, in FM/SC/FM trilayers it is observed that T_{SC} is determined by the relative magnetization orientation in the two FM layers as shown by schematic diagram in Fig 1.9 [29, 30]. Parallel orientation of the magnetic moments in the two FM layers (FM coupling) results in a lower T_{SC} than that in an anti-parallel configuration (AFM coupling). This observation was experimentally confirmed by Hauser in $\text{Fe}_3\text{O}_4/\text{In}/\text{Fe}_3\text{O}_4$ [31].

1.5. 2 Oxide multilayers

YBCO/LCMO heterostructures with high quality interfaces are ideal candidates for investigating the interaction between mutually antagonistic superconducting and ferromagnetic orders. While competition between the two ordered ground states [17,18,32-36], viz., superconductivity and ferromagnetism, in heterostructures of superconducting cuprates and perovskite manganites leads to suppression of both superconducting and magnetic transition temperatures [35,36], a variety of exotic phenomena have been seen in these heterostructures [37] and several phenomena have been predicted theoretically [30,38]. In fact, giant magnetoresistance originating from superconducting state of YBCO has recently been observed in trilayers comprising LCMO and YBCO [37]. Further, it is theoretically predicted [29] that the critical current at junctions depends on the relative polarity of the magnetic layers thus giving an additional degree of freedom in spintronic applications. From basic research viewpoint, their antagonistic ground states result in the suppression of the superconducting order parameter in close proximity to a ferromagnetic entity with the possibility of coexistence of superconductivity and magnetism. Artificially

grown superstructures of ferromagnetic and superconducting materials enable a systematic study of the coexisting orders.

Recently, from polarized neutron reflectivity measurements on a multilayer of LCMO and doped YBCO, Hoppler et al [39] inferred a giant modulation of the in-plane magnetization taking place in LCMO layers below the superconducting transition of the multilayer. It was observed that the magnetization in alternate LCMO layers is strongly suppressed while it is equally enhanced in the remaining LCMO layers. There also exist experimental studies which indicated depletion of magnetization (magnetic dead layer) in the region of LCMO lying adjacent to the YBCO/LCMO interface [40, 41] in addition to an induced moment on Cu ions in YBCO [40]. Magnetic dead layers are known to result from chemical inter-diffusion/alloying or interface roughness [42, 43] close to the interfaces in multilayers of transition metals. Scattering techniques [39-41, 44, 45] and electron spectroscopy [46] have ruled out these factors in YBCO/LCMO heterostructures. While it is experimentally established that two cuprate superconductors can be coupled over long distances through a manganite layer such as LCMO, there appears to be a lack of consensus on the theoretical mechanism to understand this.

In heterostructures of superconducting cuprates and ferromagnetic manganites, there is sufficient evidence to suggest that superconducting order persists over much longer length scales upto 100 Å [47, 48], which in the first place is very surprising. Some experiments in these heterostructures even indicated the proximity of a superconductor suppressing or significantly modifying the FM order in the ferromagnet [39-41, 44, 45].

1.6 Scope of the thesis work

In literature, the coexistence of ferromagnetism and superconductivity has been mainly investigated in artificially prepared ferromagnet/superconductor (FM/SC) heterostructures consisting of alternating FM and SC layers e.g. Fe/Nb/Fe, Nb/Gd, NbN/Co, $\text{YBa}_2\text{Cu}_3\text{O}_x/\text{La}_{1-x}\text{Ca}_x\text{MnO}_3$, $\text{YBa}_2\text{Cu}_3\text{O}_x/\text{La}_{1-x}\text{Sr}_x\text{MnO}_3$ etc [18, 49-51]. As discussed earlier, in these heterostructures, owing to the proximity effect, a superconducting order parameter can be induced in the FM layer. In other words, neighboring pair of FM layers can be coupled through a SC layer. Such systems have exhibited rich physics: (i) oscillations in superconducting transition temperature with increasing thickness of ferromagnetic layer in three-layer structures (FM/SC/FM), which were ascribed to the appearance of π -phase superconductivity; (ii) in SC/FM/SC trilayer junctions the relative phase is equal to π instead of the usual zero (known as π -junction). It has been observed that the interplay between superconductivity and magnetism can be investigated by growing bilayers and trilayers in controlled manner, i.e. the thicknesses of the layers can be varied in controlled manner to change the relative strengths of the two order parameters.

This thesis work is aimed at growth of various FM/SC heterostructures comprising of both metallic (Nb/Gd, Nb/Ni and NbN/NbO/Co) as well as oxides ($\text{YBa}_2\text{Cu}_3\text{O}_x/\text{SrTiO}_3/\text{LaCaMnO}_3$). The main emphasis is to introduce an insulating layer between superconducting and ferromagnetic layers so that the proximity effect can be controlled e.g. NbO between NbN and Co, and SrTiO_3 layer between $\text{YBa}_2\text{Cu}_3\text{O}_x$ and LaCaMnO_3 . High quality metallic heterostructures were fabricated using magnetron DC sputtering technique, while oxide heterostructures were fabricated using pulsed laser

deposition. The grown heterostructures were characterized by a host of techniques, providing several new results. The experimental details and the obtained results are organized as follows.

In *Chapter 2*, we describe the experimental techniques used during the thesis work. The details of DC magnetron sputtering system are described to deposit metallic thin films and multilayers such as Nb/Gd, Nb/Ni and NbN/NbO/Co. The configuration of the pulsed laser deposition (PLD) setup used for deposition of oxide superconductor/ ferromagnetic multilayers like $\text{YBa}_2\text{Cu}_3\text{O}_x/\text{SrTiO}_3/\text{LaCaMnO}_3$, $\text{YBa}_2\text{Cu}_3\text{O}_x/\text{SrTiO}_3/\text{LaSrMnO}_3$ is presented. An overview of various techniques used for the characterization of thin films and multilayers, such as scanning electron microscopy (SEM), X-ray diffraction (XRD), X-ray reflectivity (XRR) and polarized neutron reflectivity (PNR) are described. The details of the Superconducting Quantum Interference Device (SQUID) setup used for magnetic measurements are presented. The four probe method used for the electric transport measurements is also described.

In *Chapter 3*, the results on the sputter growth and characterization of Fe/Au[52] multilayers, Nb/Gd and Nb/Ni bilayers and NbN/NbO/Co [53] trilayer are presented. The results on Fe/Au multilayers show that magnetoresistance and remanent magnetization increases with increasing thickness of Fe thickness. The results on Nb/Gd and Nb/Ni bilayers revealed a two step superconducting transition, which is attributed to domain wall superconductivity due to the proximity of ferromagnet. Furthermore, the history dependent temperature dependent resistance characteristics confirmed the domain wall superconductivity. Possible explanation of this observation may be that the superconducting region right below a domain wall exhibits a higher transition temperature

compared to the one below a ferromagnetic domain. Detailed transport studies carried out on the trilayer NbN/NbO/Co revealed that in the superconducting state the resistance reappears. A possible reason for re-entrant resistance might be the vortex dynamics in NbN superconducting layer due to the stray fields created by Co layer.

In *Chapter 4*, results on the growth and characterization of thin films of YBCO, LCMO and LSMO as well as YBCO/SrTiO₃/LCMO trilayers is presented. The films and multilayers are thoroughly investigated using XRD and XRR measurements. Observation of only (00n) reflections and clear thickness fringes confirm the epitaxy and high quality of the films. XRR measurements have been used to estimate the interface roughness of the films. Such characterization has been carried out on several films and trilayers of YBCO/SrTiO₃/LCMO and few of them have been chosen for further investigation of proximity effect using polarized neutron reflectivity (PNR). The results show that below the superconducting transition temperature of the trilayer, a thin magnetic “dead layer” is formed in LCMO adjacent to the SrTiO₃ layer, which could be as thick as 5 nm. These results suggested a possible tunneling of the superconducting order parameter through the insulating barrier thereby modifying the magnetic state of LCMO.

The summary of the thesis along with future scope of the work are presented in *Chapter 5*.

Experimental techniques

2.1 Introduction

In this Chapter we describe the experimental techniques used during the thesis work. In the next section (i) The details of DC magnetron sputtering system to deposit metallic thin films and multilayers such as Nb/Gd, Nb/Ni and NbN/NbO/Co and (ii) configuration of the pulsed laser deposition (PLD) setup used for deposition of oxide superconductor/ ferromagnet multilayers like $\text{YBa}_2\text{Cu}_3\text{O}_x/\text{SrTiO}_3/\text{La}_{2/3}\text{Ca}_{1/3}\text{MnO}_3$, $\text{YBa}_2\text{Cu}_3\text{O}_x/\text{SrTiO}_3/\text{La}_{2/3}\text{Sr}_{1/3}\text{MnO}_3$ are described. In section 2.3, an overview of various techniques used for the characterization of thin films and multilayers, such as scanning electron microscopy (SEM), X- ray diffraction (XRD), X-ray reflectivity (XRR) and Polarized Neutron Reflectivity (PNR) are described. In section 2.4, details of the Superconducting Quantum Interference Device (SQUID) based magnetometer used for magnetic measurements and the four probe method used for the electric transport measurements are described.

2.2 Thin film and multilayer deposition techniques

2.2.1 DC magnetron sputtering

Sputtering is a process in which inert gaseous ions are accelerated towards a target material of interest to be deposited [54-57]. Momentum transfer from the ions to the target atoms is sufficient to overcome the binding energy and move towards the substrate to be deposited on. The process is realized in a closed chamber pumped down (by Turbo pump)

to a high base vacuum before deposition. The chamber is then filled with ultra-high pure Argon to maintain a pressure between 0 to 10^{-2} mbar. A schematic diagram of dc magnetron sputtering system is shown in Fig. 2.1.

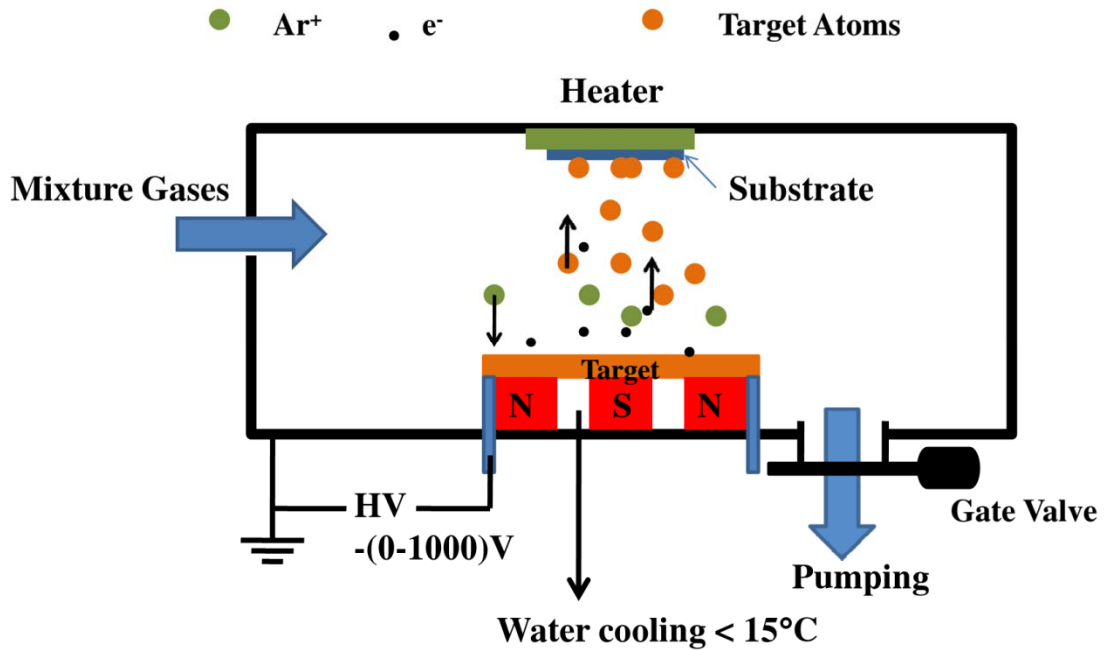


Fig. 2.1 Schematic diagram of DC magnetron sputtering system.

When few hundred volts of negative voltage U is applied across the target-cathode and substrate-anode, the stray charges present in Ar are accelerated towards respective electrodes producing secondary electrons, which initiate further ionization of Ar atoms. Plasma is generated and a self sustaining glow discharge starts at a breakdown voltage U_D given [58] by

$$U_D = \frac{A \cdot p \cdot d}{(\ln(pd) + B)}$$

where, p is the gas pressure and d is electrode distance, A and B are constants characteristic of the target materials. The ionization probability rises with an increase in pressure. Hence number of ions and the conductivity of the gas also increase, resulting in a drop in breakdown voltage.

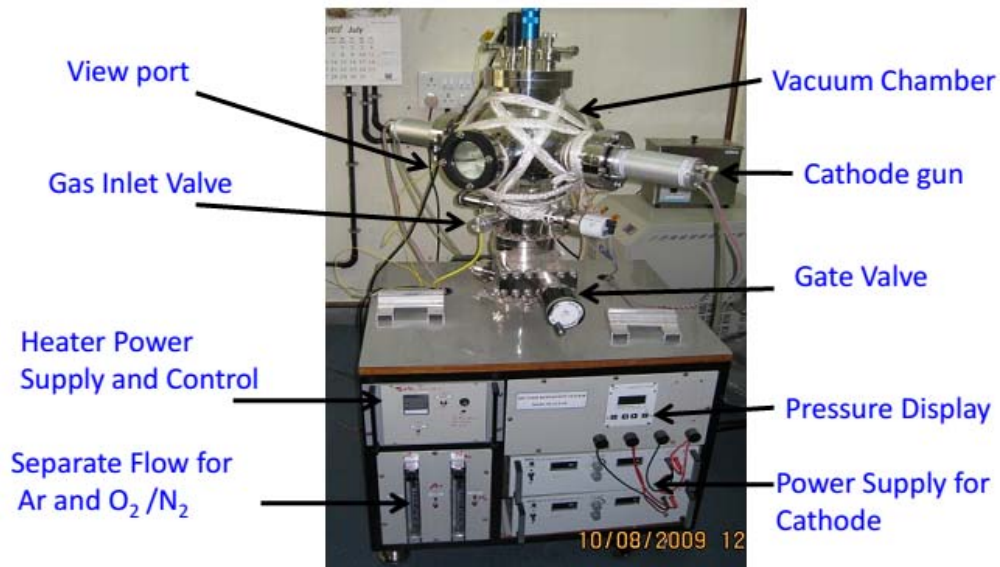


Fig.2.2: Photograph of DC sputtering system.

The ionization rate can be further increased by set of magnets configured below the target in such a way that the magnetic field above the target is perpendicular to the electric field so that the electron path length increases, causes making plasma discharge at lower gas pressures. The process is called the magnetron sputtering. This leads to higher deposition rate, the sputtered atoms encounter fewer collisions on the way to the substrate and the kinetic energy at the impact on the substrate is higher [59]. DC-sputtering is however, restricted to conducting materials like metals or doped semiconductors. An insulating target would soon be charged by positive ions leading to a shielding of the electrical field and a rapid decay of ion current. However, RF-sputtering enables sputtering

of insulating and non-conducting materials. For reactive sputtering other gases like oxygen or nitrogen are mixed into the sputter chamber in addition to argon, to produce metallic oxides or nitrides. A photograph of the DC magnetron sputtering system (Excel Instruments make) used for metallic thin film and multilayer deposition in the present study is shown in Fig. 2.2. Sputtering parameters of our system are summarized in Table 2.1. Sputtering process enables deposition of uniform films over large area. But the use of external gases which always contain impurities is a major disadvantage especially while depositing reactive metals.

Table 2.1: Salient features of DC magnetron sputtering system

Parameter	Range
DC Power supply of Cathode	Up 1000 Volt, 1 A
Best Vacuum	1×10^{-7} mbar
No. Cathodes	Three at angle of 0° , 45° , 180°
Co-sputtering	Yes
Substrate heating	Up 850°C
Background gas	Ar, N_2 , O_2 with manual controlling by flow meter

2.2.2 Pulsed laser deposition system

During this thesis work, a pulsed laser deposition (PLD) system was set up and its photograph is shown in Fig. 2.3. The main components of a PLD system are a pulsed laser, optics, and a vacuum system. PLD [60-62] is employed for preparation of complex multi-component oxides (YBCO, LSMO, LCMO and STO) thin films and their heterostructures [63-65]. In this technique the energy source (pulsed laser) is located outside the vacuum

chamber. A pulsed laser beam is focused onto the surface of a target which has to ablate. The strong absorption of the electromagnetic radiation (laser pulse) by the solid surface leads to rapid evaporation of the target material with raised surface temperature up to few thousand K. A schematic of the PLD system is shown in Fig. 2.4. The evaporated materials consist of highly excited and ionized species. A glowing plasma plume is immediately generated in front of the target surface, if the ablation is carried out in vacuum. PLD can be carried out in vacuum as well as in presence of a dilute background of a reactive gas such as O_2 , which are used for modification of the composition of the grown films.



Fig. 2.3: Photograph of the PLD system.

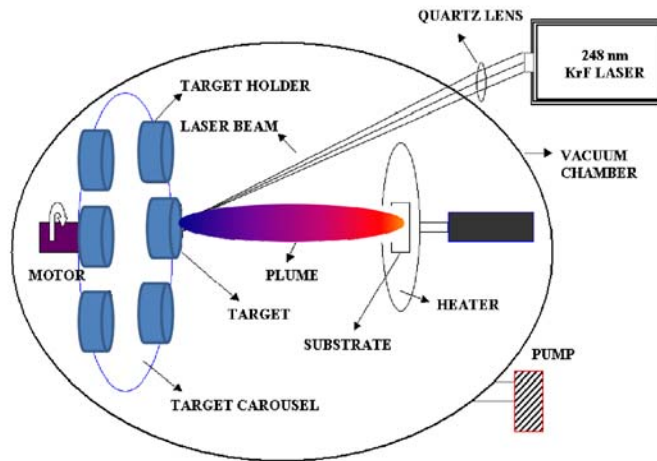


Fig. 2.4: Schematic diagram of the PLD system

Table 2.2: Salient features of PLD system developed at TPD, BARC

Parameter	Range
Wavelength of Laser	248 nm (KrF:Excimer Laser)
Per pulse energy	Upto 750 mJ
Fluence per pulse	7.5 J/cm ²
Pulse duration	30 n sec
Pulse Repetition rate	Up to 50 Hz
Pre-deposition Vacuum	1 × 10 ⁻⁶ mbar
No. Targets	Up to six
Target roasting	Yes
Target rotation	10 rpm
Substrate heating	Up 850°C
Background gas	Ar, N ₂ , O ₂ by flow meter

PLD is a easy technique for the growth of thin films as it requires only a few experimental parameters i.e. laser intensity and pulse repetition rate to be controlled. The targets used in PLD are smaller as compared to those required in sputtering technique. Also it is quite easy to produce multi-layered films of different materials by sequential ablation of assorted targets. By controlling the number of pulses, a fine control of film thickness down to atomic monolayer can be achieved. The most important feature of PLD is that the stoichiometry of the target is retained in the deposited films as a result of extremely rapid heating of the target surface (10^{12} K/s typically up to temperatures of more than 5000 K within a few ns) to few thousand of Kelvin depending on the target material [61,62]. PLD technique has even been used to synthesize nanotubes [66] and nanoparticles [67]. Though the technique offers several advantages, there are some associated shortcomings such as reproducibility, difficulty in depositing over large area, which restrict its utilization for commercial purpose [68, 69]. Another problem often encountered in PLD is the splashing of particulates on the films due to sub-surface boiling, expulsion of the liquid layer by shock wave recoil pressure and exfoliation. The size of particulates may be as large as a few micrometers. Such particulates can greatly affect the growth of the subsequent layers as well as the electrical properties of the films.

One of the basic requirements for growing high quality thin films using PLD is the availability of single-phase dense targets. We have synthesized polycrystalline $\text{YBa}_2\text{Cu}_3\text{O}_{7-\delta}$ (YBCO), $\text{La}_{2/3}\text{Sr}_{1/3}\text{MnO}_3$ (LSMO), $\text{La}_{2/3}\text{Ca}_{1/3}\text{MnO}_3$ (LCMO) and SrTiO_3 (STO) targets using solid-state reaction route. Synthesis of ceramic oxides using solid-state reaction

method involves several steps, such as grinding the constituents (taken in the form of oxides, carbonates or nitrates), calcination (to decompose the carbonates and nitrates into oxides), sintering and oxygen annealing. In order to obtain single-phase homogeneous material, repeated grinding, calcinations and sintering are essential. Targets are then prepared by pressing the synthesized powder into pellets (25 mm diameter and 3 mm thickness) and again sintered under atmospheric oxygen pressure O_2 at 960°C for 4 h. During the cooling schedule, pellets are annealed at 450°C for 24 h to obtain fully oxygenated YBCO targets.

In order to deposit heterostructures, laser beam is alternately focused on respective targets. Otherwise the deposition process remains same as described above. The details of optimization of parameters for YBCO, LSMO, LCMO, STO films and their heterostructures are given in Chapter 4.

2.3 Structural and morphological characterization

2.3.1 X-ray diffraction

The determination of crystal structure is an essential part of any work involving epitaxial thin films. For that X-ray diffraction (XRD) is the most powerful non destructive technique. XRD data can provide information like phase purity, crystal structure, lattice parameters, crystal orientations, average grain size, and uniform & non-uniform strain. X-ray diffraction (XRD) patterns were recorded using a rotating anode type diffractometer with $Cu-K_\alpha$ radiation. In particular, to study the strain and grain size and their distribution,

the profile of the diffraction need to be analyzed. Both of them are reflected in the width and asymmetry of the diffraction profile.

Strain in a thin film can originate from the lattice mismatch, defects and deposition conditions. These strains are of two types: (i) uniform strain and (ii) non- uniform strain. Effect of these strains [70] on XRD peak positions and broadening are described in the schematic (Fig 2.5). Change in XRD peak position with respect to the peak position in bulk material as shown in Fig. 2.5 (b) indicates uniform stain in the film. The shift comes from changing the lattice spacing in direction perpendicular to film plane. If d reduces (increases) from its bulk value, peak shifts to higher (lower) 2θ . In unit cell volume conserving deformation, d decreases in case of tensile strain in ab plane (expansion of lattice parameters in ab plane) and d increases in case of compressive strain in ab plane.

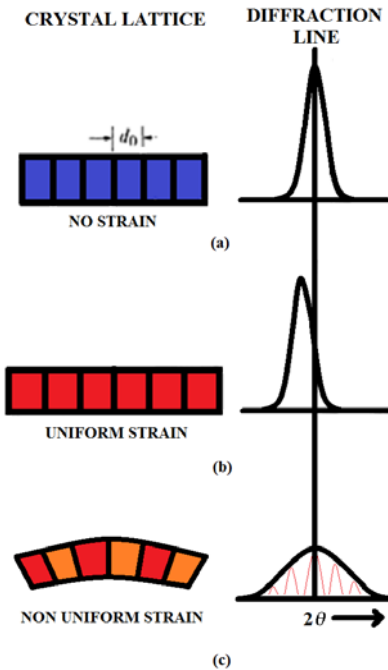


Fig. 2.5: Schematic diagram showing how strain affects XRD peaks. (a) Shows relaxed film, (b) Film with uniform strain and (c) Film with non uniform strain.

Strain (ε) can be calculated using

$$\% \varepsilon = \frac{(a_{thin} - a_{bulk})}{a_{bulk}} \times 100$$

Further, overall broadening in XRD peak β is determined by instrument broadening β_i , broadening due to finite crystallite size β_G and non-uniform strain β_S and is given by

$$\beta^2 = \beta_i^2 + \beta_G^2 + \beta_S^2$$

$$\beta^2 = \beta_i^2 + \left\{ \frac{K\lambda}{D\cos\theta} \right\}^2 + (4\varepsilon\tan\theta)^2$$

Where, D and ε are grain size and non-uniform strain respectively.

In case of c-oriented film, simple XRD pattern can provide information about the thickness of the film. Amplitude of diffracted x-rays from one-dimensional array of atoms is given by

$$A = e^{0iQd} + e^{iQd} + e^{2iQd} + \dots + e^{(N-1)iQd}$$

Here d is spacing between atoms and Q momentum transfer vector. A is written as

$$A = \frac{1 - e^{iNQd}}{1 - e^{iQd}}$$

Intensity of reflected beam from thin film is thus given as square of the amplitude of scattered beam and is most commonly given as

$$I = AA^*$$

$$I \propto \left| \frac{\sin(NQd)}{\sin(Qd)} \right|^2$$

In this course work, thickness of epitaxial YBCO, LSMO, and LCMO was estimated by fitting the XRD peak to the above equation, which was found to be very close to that measured using X-ray reflectivity.

2.3.2 X-ray and polarized neutron reflectivity

Specular reflectivity involves measurement of the radiation (x-ray /neutron) reflected from a sample (Fig. 2.6) as a function of wave vector transfer $Q_z [= \frac{2\pi}{\lambda} (\sin(\theta_i) + \sin(\theta_f))]$, perpendicular to the sample surface where λ is x-ray or neutron wavelength. The specular reflectivity is quantitatively related to the Fourier transform of the scattering length density (SLD) depth profile $\rho(z)$ [71, 72] averaged over the sample area. In case of x-ray, SLD is electron density where as in neutron it is some of nuclear and magnetic. In this thesis work, both Polarised Neutron Reflectivity (PNR) and X-Ray Reflectivity are used to characterize the multilayer samples. Here detail description of PNR is described.

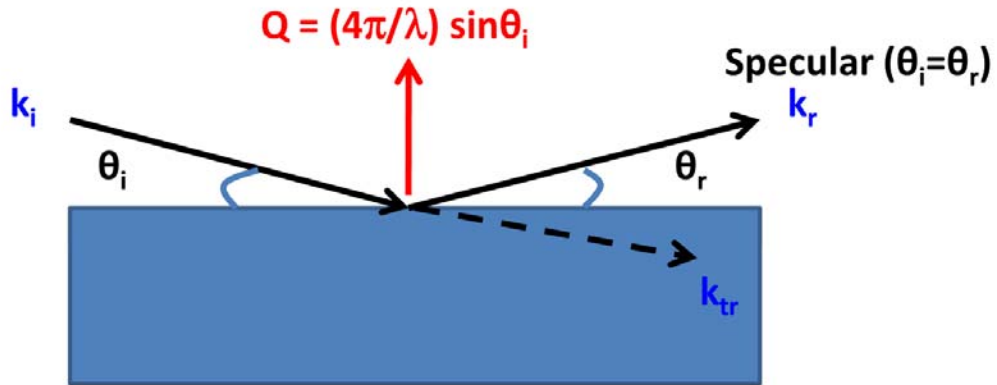


Fig 2.6: Geometry for specular reflectivity

Polarized Neutron Reflectivity (PNR) is an important technique to investigate the magnetic and structural properties of thin magnetic films and multilayers [73-76]. PNR can determine the depth profile of magnetization the vector in magnetic thin film structures. Counting the number of neutrons elastically and specularly (angle of reflection equal to angle of incidence) reflected as a function of glancing incident angle can provide the in-plane average of the scattering density. From this scattering length density profile, concentration of atoms of a given type at a particular depth can be inferred. Furthermore, if the incident neutrons are polarized and the resultant polarization of the reflected neutron beam is analyzed, possible magnetic contributions to the scattering density can be distinguished in microscopic detail.

In polarized neutron reflectivity, neutron spin is aligned either parallel or anti-parallel to the magnetic field. Interaction of neutron occurs by two ways (i) the interaction of the neutron with the nuclei and (ii) the interaction of neutron with magnetic moment of species. Potential energy of neutron

$$V = \frac{2\pi\hbar^2}{m}(\rho_N + \rho_M)$$

Where ρ_N and ρ_M are nuclear and magnetic scattering length density respectively.

Reflectivity for can be expressed by following equations

$$R^\pm = \left| \frac{Q - \sqrt{Q^2 - 16\pi(\rho_N \pm \rho_M)}}{Q + \sqrt{Q^2 - 16\pi(\rho_N \pm \rho_M)}} \right|^2$$

Where R^+ and R^- are PNR for up spin and down spin neutrons, respectively.

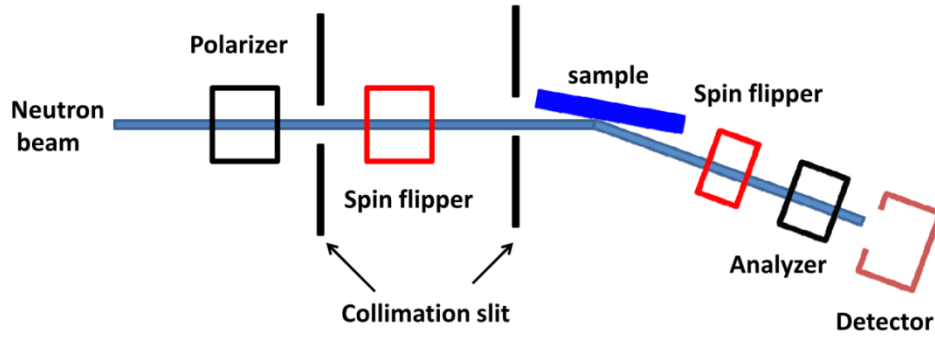


Fig. 2.7: Schematics of the polarized neutron reflectometer

The critical wave vector (above that complete external reflection take place) is defined as

$$Q_c^\pm = 4\sqrt{\pi(\rho_N \pm \rho_M)}$$

In the case of multilayer (having several interfaces), at each individual interface the boundary conditions must be fulfilled and for a stratified medium the total reflectivity is composed of the contributions from each interface. The Parratt formalism [77] is one method to calculate the reflected intensity of a stratified medium. PNR measurements are carried out at Dhruva, BARC (India) and FRM-II (Germany). Standard set-up of polarized neutron reflectometer is shown in Fig. 2.7.

The angle of incidence was varied by a precise tilting of the sample surface relative to the fixed collimated neutron beam. Using a polarizing supermirror and a spin flipper, polarized spin-down or spin-up neutrons were obtained. A guide field was applied throughout the beam path using special constructions of permanent magnets supplying a magnetic field along the horizontal direction, perpendicular to the beam path.

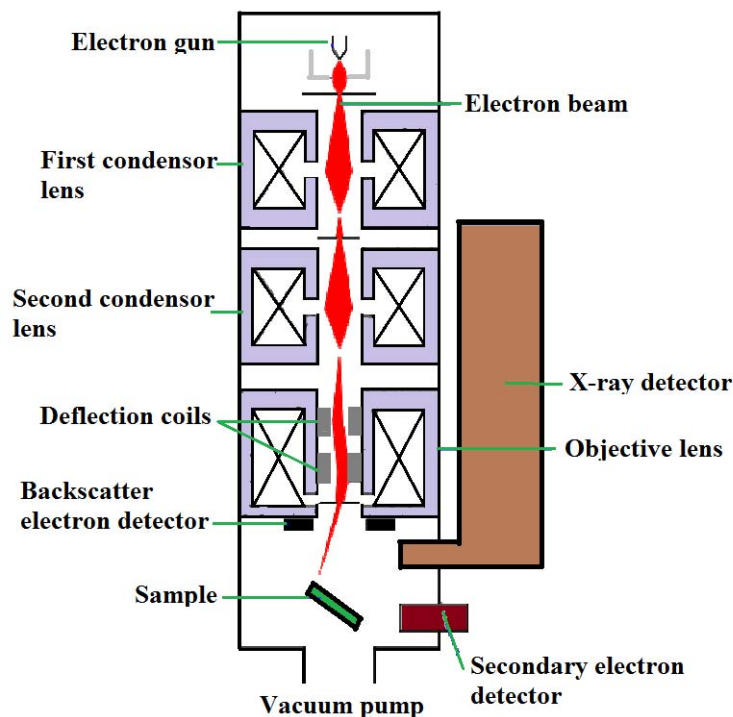


Fig. 2.8: Block diagram of a typical SEM setup.

2.3.3 Scanning electron microscopy

A scanning electron microscope is a type of electron microscope where a beam of focused electrons is scanned on the sample to image its surface. The operation of SEM consists of applying voltage difference between the conductive surface and the filament under a vacuum environment of 10^{-4} to 10^{-10} Torr. The electron emitted from the filament are accelerated to about 2-40 kV which then are guided and focused onto the sample surface by a series of electromagnetic lenses. Schematic representing operation of SEM is shown in Fig. 2.8.

The electrons interact with the sample within a few nanometers to several microns of the surface depending on the beam parameters and sample type [78]. Incident electrons interact with the specimen surface by two types of scattering, i) elastic scattering in which the electrons change indirection without any change in energy (backscattered electrons) and ii) inelastic in which the striking electrons collide with and displace electrons (secondary electrons) from their orbits around nuclei of atoms (Fig. 2.9).

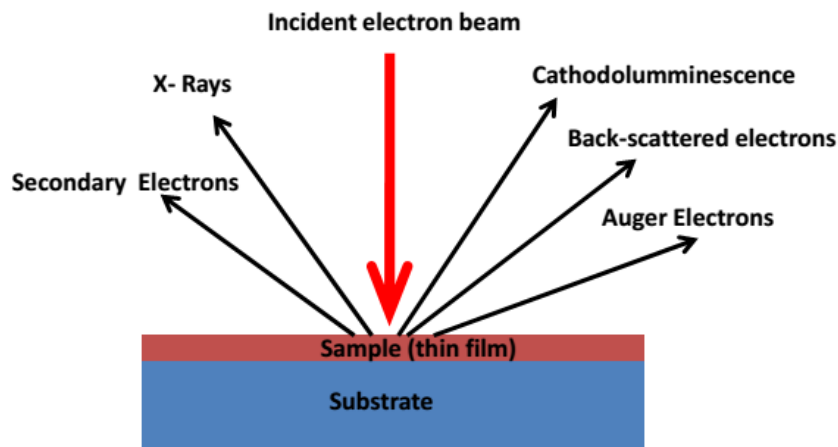


Fig. 2.9 Interaction of incident electron beam with sample surface.

When the vacancy created by these ejected electrons is filled by an electron from a higher orbit level, X-ray characteristic of the energy transition is emitted. Auger electrons and Cathodo luminiscense are other two phenomena occurring due to electron specimen interactions. Auger electrons are ejected by radiationless excitation of the target atom of the sample by the incident electron beam while Cathodoluminescence is the emission of photons of characteristic wavelength from the material.

Secondary electrons are mostly used for imaging the surface of a sample with the best resolution of the image close to 10 nm. Since secondary electrons have low energy (<50eV) only those emitted from the first few nanometers on the surface have enough energy to escape and be typically detected by an Evert-Thornley Scintillator photomultiplier detector. The SEM image formed is the result of the intensity variation of secondary electrons from each xy position from the surface during scanning of electron beam over the surface.

The Evert-Thornley detector consists of a scintillator, collector, guiding pipe and a photomultiplier tube. Electrons striking the positively biased scintillator are converted to a bunch of electrons that travel through the pipe to a photomultiplier tube. Here the photons are converted to a voltage signal depending on the intensity of striking secondary electrons. This voltage signal is then amplified to generate a point of brightness on the cathode ray tube screen. Contrast in the brightness of the pixels on the screen is due to the difference in intensity arising from the varying surface profile of the sample with respect to the incident electron beam, and therefore directly represents the morphology of the sample surface.

Backscattered electrons are high energy electrons (>50eV) that are reflected or backscattered out of the specimen interaction volume. Intensity of backscattered electrons

varies with the specimen's atomic number. This differing intensity makes higher atomic number elements to appear brighter than the lower atomic number elements. This interaction is utilized to differentiate parts of the specimen that have different average atomic number.



Fig. 2.10: Photograph of SEM (model: Tescan VEGA MV2300T/40).

Energy of X-rays emitted from the sample surface when incident electron beam interacts with it is characteristic of the element producing it and therefore can be utilized to identify the chemical composition of the sample. EDX detector measures the number of emitted X-rays as a function of their energy. The photograph of SEM (model: Tescan VEGA MV2300T/40) that has been used in this thesis is shown in Fig. 2.10.

2.4 Transport and magnetic characterization

Superconducting and ferromagnetic properties of thin films and heterostructures are characterized by transport and dc magnetization measurement.

2.4.1 Four-probe resistivity measurement

Resistivity, an intrinsic property, tells about the electrical transport properties of the material. In metals it decreases as a function of temperature and saturates at some value, known as residual resistivity that gives information on the imperfections in the material. Geometry dependent resistance in GMR and CMR materials were found to show dramatic changes due to the magnetic field. Measurement of resistance as function of temperature is the most common method of finding the transition (or critical) temperature T_{SC} of the superconductors.

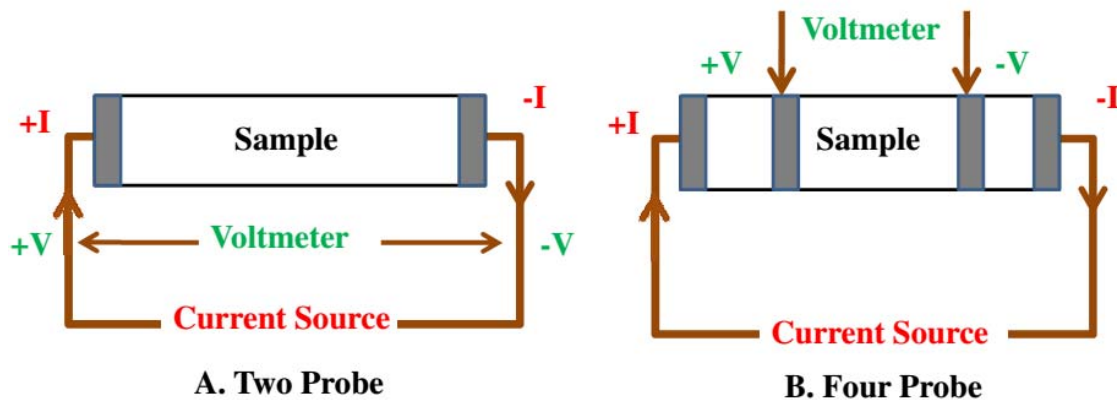


Fig. 2.11: Schematic diagram of linear two probe and four probe measurements.

At temperatures below T_{SC} , the resistance of the superconductor becomes very small; values less than $10^{-23}\Omega$ cm have been measured in conventional low temperature superconductors (Nb, NbN etc). Therefore the criteria of *zero resistance* need to be defined. Zero resistance is sometimes defined as a resistivity less than that of Cu at the same temperature, ($\sim 10^{-8}\Omega$ cm). The American Society for Testing and Materials (ASTM) has suggested a criterion four orders of magnitude lower than this value, i.e., $10^{-12}\Omega$ cm.

Measurement of resistance ($R = V/I$ or dV/dI) can be done either ratio of the voltage drop across a specimen (V) when a current (I) of known magnitude is passed or differentiation of drop voltage with respect current flow through sample. Measurement of resistance set can be two ways – two probes and four probes as shown by schematic diagram in Fig. 2.11. In case of low voltage or low resistance measurement the two probe geometry will not work because the contact resistance and lead resistance will dominate.

In any accurate transport measurement at low level, the environment is essential which may affect the accuracy of low level measurements [79]. Change in temperatures can affect low level measurements in several ways, including causing thermal expansion or contraction of insulators and producing noise currents. Also, a temperature rise can cause an increase in the input bias current of the meter. It is always better to minimize errors due to temperature variations by operating the entire system in a thermally stable environment. Use the instrument's zero or suppress feature to null offsets once the system has achieved thermal stability. Repeat the zeroing process whenever the ambient temperature changes. To ensure optimum accuracy, zero the instrument on the same range as that to be used for the measurement.

Excess humidity can reduce insulation resistance on PC boards and in test connection insulators. Reductions in insulation resistance have a serious effect on high impedance measurements. In addition, humidity or moisture can combine with any contaminants present to create electrochemical effects that can produce offset currents. This effect can be minimize by reduce the humidity in the environment (ideally <50%). Further this effect can be minimizing to putting instrument on 2-4 hour before actual measurements.

In low voltage measurement, offset voltages and noise sources pay significant errors which can normally be ignored when measuring higher voltage levels. Ideally, when a voltmeter is connected to a relatively low impedance circuit in which no voltages are present, it should read zero. However, a number of error sources in the circuit may be seen as a non-zero voltage offset. These sources include thermoelectric voltages, offsets generated by rectification of RFI (radio frequency interference), and offsets in the voltmeter input circuit. Thermoelectric voltages (thermoelectric EMFs) are the most common source of errors in low voltage measurements. These voltages are generated when different parts of a circuit are at different temperatures and when conductors made of dissimilar materials are joined together. Joint of dissimilar material can produce few μV , microvolt (Cu-Pb/Sn \sim 1-3) to 1000 μV (Cu-CoO) [79]. It can be reduced by using the single wire from specimen to measurement units (Nanovoltmeter). In our case these error are minimized by following ways

- (i) Single copper leads are used to measure the drop voltage.
- (ii) Leads connection to instrument, Copper leads always freshly cleaned to remove the CuO.

- (iii) Average voltage (difference of Voltages for current in both direction) is used for resistance measurements

Magnetic fields generate error voltages, which is basically due to change in flux through voltage measure lead close circuits area. This voltage error caused by two reasons; i) Variation in magnetic field with time, and ii) Relative motion between the circuit in the field. Voltages in conductors can be generated from the motion of a conductor in a magnetic field. This error can be minimized using the twisting of voltage leads.

The resistance measured is not necessarily a bulk property. Provided applied currents are small, a fiber of superconducting region in a specimen may give rise to the resistivity discontinuity in superconductors. Conversely, circuits can be broken by cracks and contact failure caused by thermal stress arising during a measurement. These can cause discontinuities in the voltage signal, which may give the illusion of superconductivity, but can usually be checked by monitoring the simultaneous current flow.

2.4.2 DC magnetization

The magnetic properties of our samples (in bulk and thin film form) were measured using SQUID (Superconducting Quantum Interference Device) magnetometer. The heart of the SQUID magnetometer is Josephson junction [80], which in a superconducting loop and acts as a magnetic flux to voltage transducer. These junctions are tunnel junctions comprised of two superconducting thin films with an insulator or normal metal layer between them. Quantum Design Magnetic Property Measurement System (MPMS) is widely used for magnetic characterization of materials. MPMS SQUID magnetometer [81]

generally consists of following five sections. i) A superconducting magnet, ii) The SQUID detector, iii) The temperature control module, iv) The sample handling system and v) Liquid helium (L-He). The system goes down to 2.25 K in temperature and maximum of 5.5 Tesla in magnetic field generated by NbTi magnet. Temperature stability in the whole range of temperature is achieved by simultaneously controlling cold gas around the sample chamber and heating the gas with heater wire wound around the sample chamber shown by schematic diagram in Fig. 2.12.

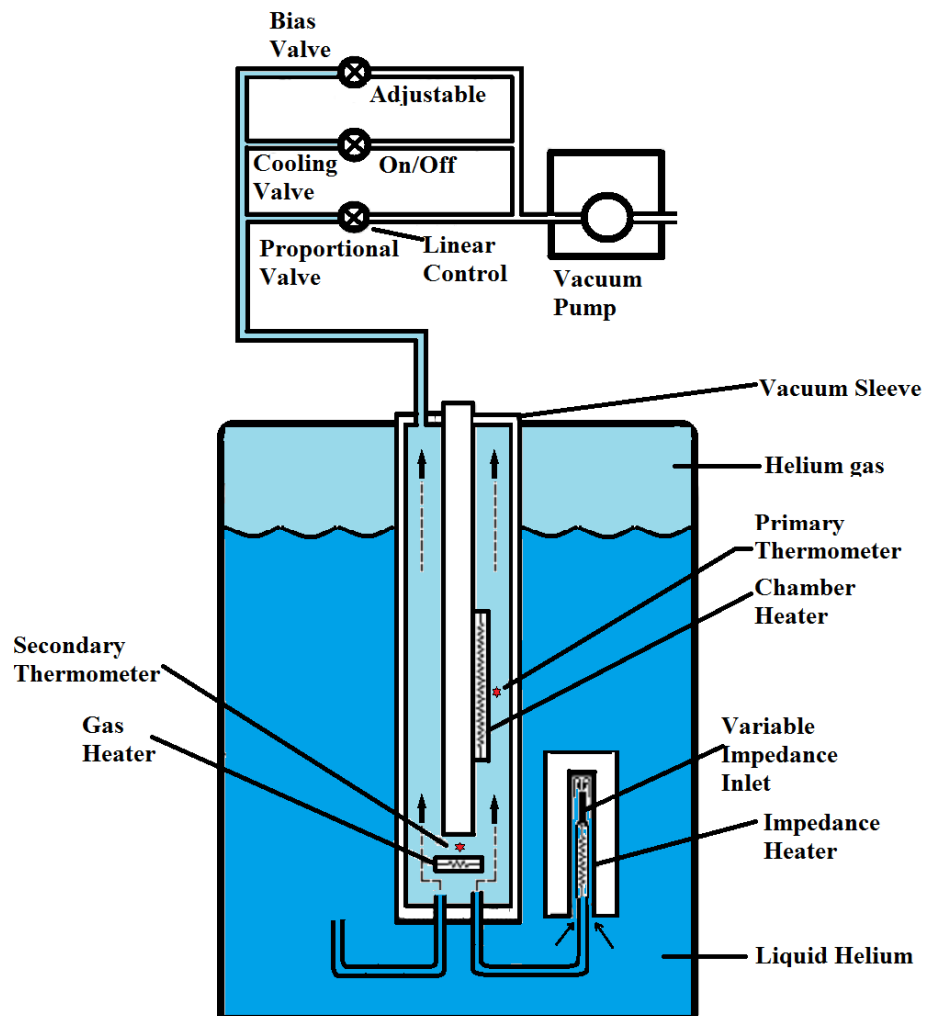


Fig. 2.12: Schematic diagram of temperature control system.

The heart of the MPMS is the mechanism of measurement of magnetic moment shown in Fig. 2.13. The main components here are second derivative gradiometer coil (pick up coil), single junction SQUID loop and radio frequency resonant circuit. All of them are inductively coupled to each other.

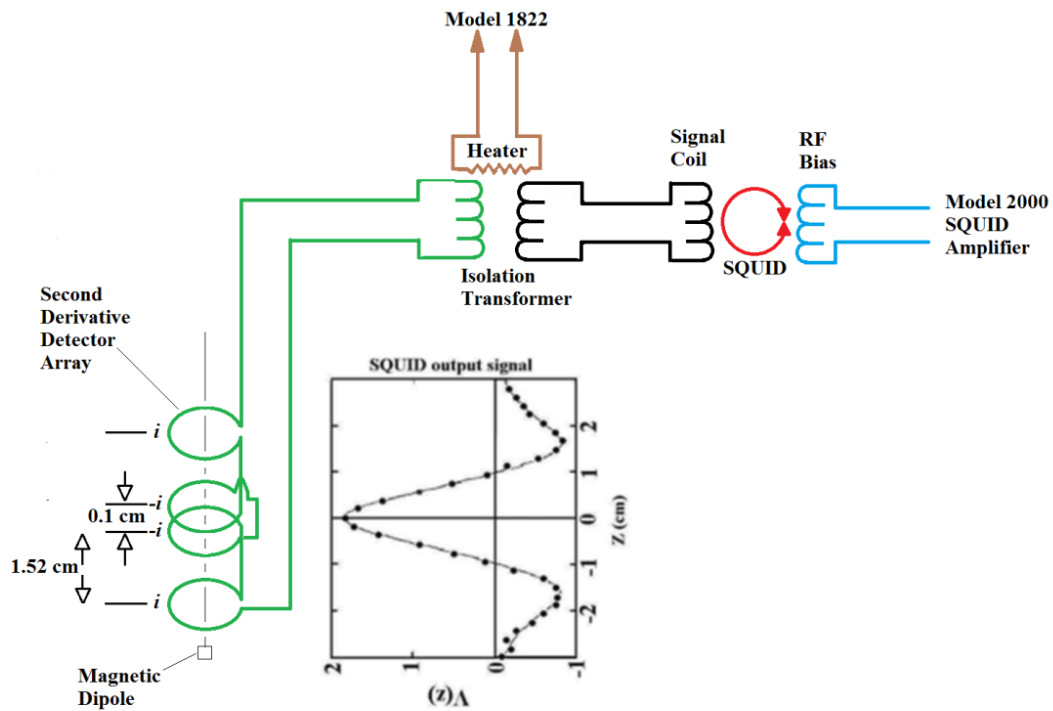


Fig. 2.13: Schematic diagram of measurement unit.

Sample whose magnetic moment is to be measured is scanned through the second order gradiometer pick up coil which is symmetrically in magnetic field. The total distance of the scan is known as scan length. Current induced in the gradiometer due to the scan is felt by the SQUID sensor through the inductively coupled coils. The voltage across the rf biased tank circuit which is also coupled to the SQUID sensor will reflect the flux induced

by the sample. The magnetic flux in gradiometer as a function of the position of a unit magnetic dipole moment is given by

$$\phi(z) = \frac{\mu_0 R^2}{2} \left\{ -\frac{1}{[R^2 + (z + Z)^2]^{3/2}} + \frac{2}{[R^2 + z^2]^{3/2}} - \frac{1}{[R^2 + (z - Z)^2]^{3/2}} \right\}$$

Where R ($= 0.97$ cm) is the gradiometer coil radius, $2Z$ ($= 3.04$ cm in our QD MPMS5 magnetometer) is the distance between the two outer turns of the gradiometer coil and z is the sample distance measured from the center of the gradiometer coil. An ideal SQUID response of a point dipole moment is given by

$$V(z) = c\phi(z)$$

where, the c is the calibration factor of the instrument. Inclusion of usually present constant offset a and a linear drift bz modify the SQUID response to the form

$$V^{modified}(z) = a + bz + mV(z - z_0)$$

here z_0 is correction for off centering of the sample. When the actual sample is measured, SQUID response is fitted to the above expression by the software to obtain the magnetic moment. In order to destroy the prior history of the measurement the heater in the isolation transformer is switched on to make the superconducting primary and secondary coil normal. During the measurement the heater is switched off by the software. This heater is switched on during the charging of the superconducting magnet to eliminate the induced currents in the circuit. The figure also shows a typical SQUID voltage response as a function of the sample position.

Chapter -3

**Metallic superconductor/ferromagnet
multilayers: Growth and proximity effects**

3.1 Introduction

In this Chapter we present investigation of the proximity effects in the metallic SC/FM thin film heterostructures by transport and magnetic measurements. In order to fabricate the metallic SC/FM heterostructures by DC magnetron sputtering, we have first optimized the growth conditions of individual superconducting (Nb and NbN) and magnetic (Fe, Co, Ni and Gd) thin films. The following heterostructures were grown and characterized (i) Fe/Au multilayers; (ii) Nb/Gd and Nb/Ni bilayers; and NbN/NbO/Co trilayers. The obtained results are analyzed in the following Sections.

3.2 Metallic thin films by DC magnetron sputtering

Here we describe the growth and characterization of thin films of various ferromagnetic (i.e. Co, Ni and Gd) and superconducting (Nb and NbN) materials by DC magnetron sputtering. The idea is to optimize the growth conditions parameters such as Ar pressure, sputtering power, substrate temperature and post annealing process parameters, etc., so that bilayer, superlattices and multilayers can be grown easily.

3.2.1 Magnetic thin films

(a) Co films

In order to estimate the deposition rate of Co by DC magnetron sputtering, films were deposited on Si (111) substrate at room temperature under argon partial pressure of

$\sim 5 \times 10^{-3}$ mbar, with sputtering power of 30 W (500 V, 60 mA) for 180 s. The nominal thickness of the films was 1000 Å. In order to confirm the thickness of these films, specular X-Ray Reflectivity (XRR) measurements were carried out using Cu K_α radiation as a function of wave vector transfer $Q = (4\pi/\lambda) \sin \theta$, where θ is the incident angle on the film and λ is the wavelength of the probe. A typical result is shown in Fig. 3.1. The experimental data were theoretically best fitted to a two layer model as depicted in the inset of Fig. 3.1, which assumes that a CoO layers forms on the surface of the Co film.

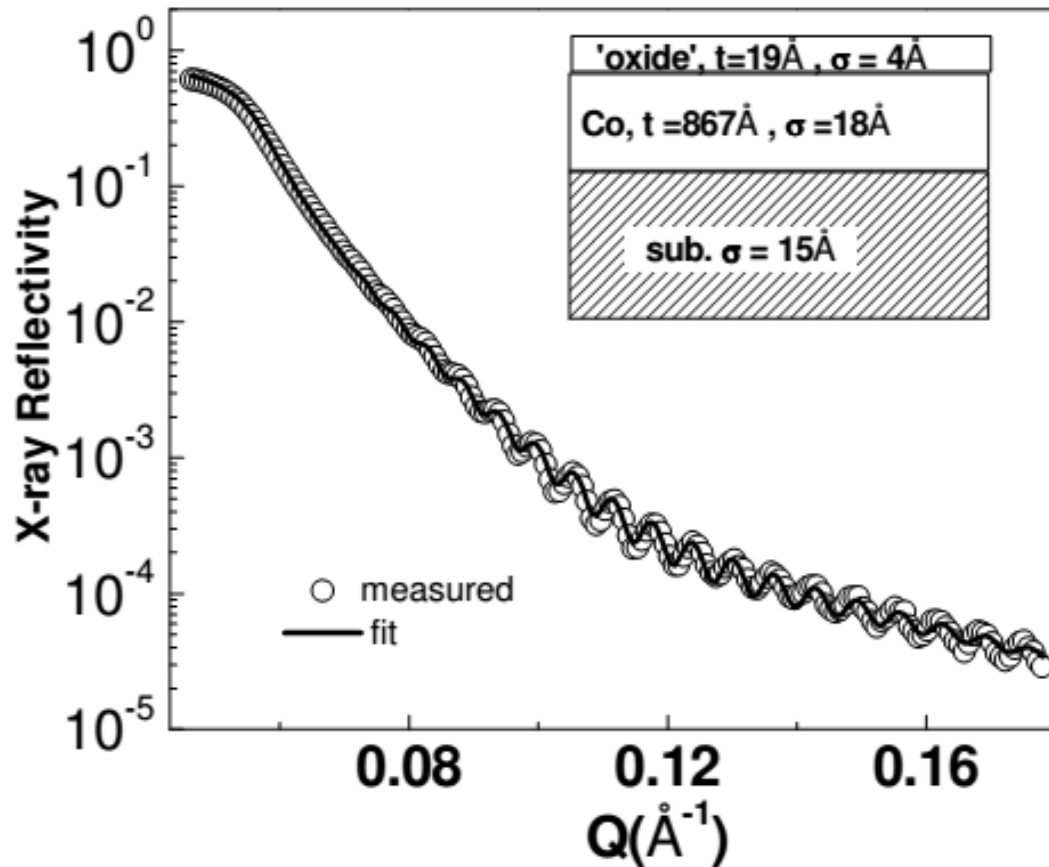


Fig. 3.1: XRR measurements on Co film, open circles and solid line are measured and fitted data, respectively. Inset shows two layer model used for the fitting.

It is evident that the thicknesses of Co and CoO layers obtained from the fits are $867\pm 18 \text{ \AA}$ and $19\pm 4 \text{ \AA}$ respectively. This result indicated that: (i) the deposition rate of the Co (under the given sputtering parameters) is 5 \AA/s , (ii) the surface Co layer gets readily oxidized. Using this deposition rate, Co films of various thicknesses were grown and the XRR data showed that the actual thickness is within $\pm 5\%$ of the nominal thickness estimated from the deposition time.

In order to observe the evolution of the morphology of the film with annealing temperature, 100 \AA Co thin films were annealed immediately after deposition (inside the sputtering deposition

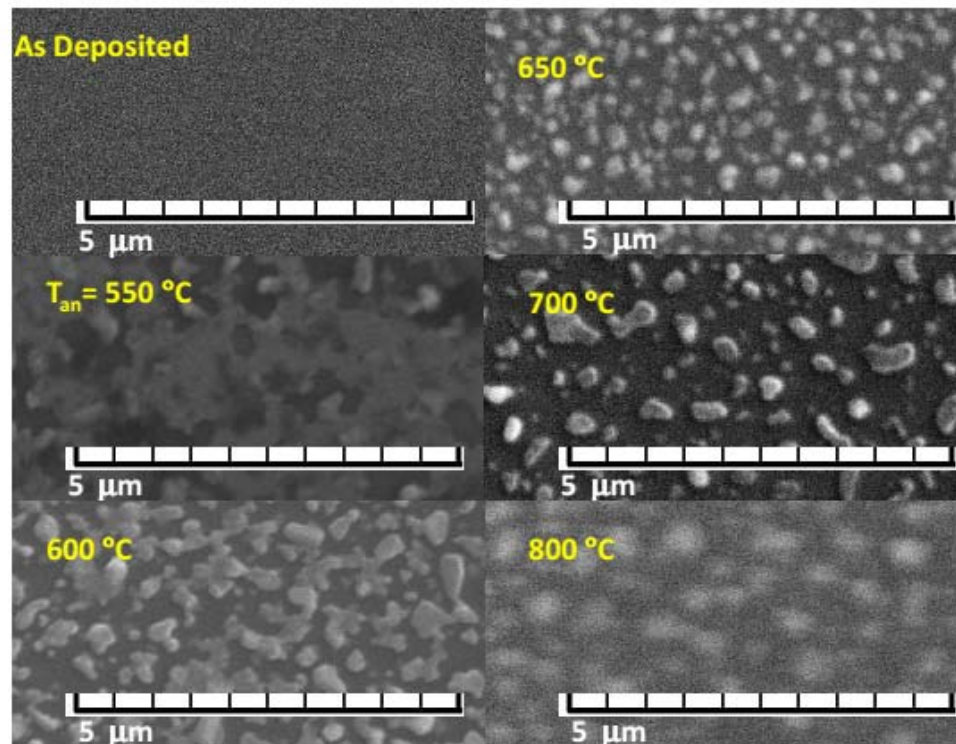


Fig. 3.2: SEM images of the sputter deposited Co films annealed at different temperatures (under a vacuum of 5×10^{-6} mbar for 1 h).

chamber under a vacuum of 5×10^{-6} mbar for 1 h) at different temperatures T_{an} . The films were then coated by a 100 Å silver capping layer at room temperature. The Ag-capping layer was important to prevent the surface oxidation of Co-films, which influences the magnetization data. Surface morphology of the films deposited with different annealing temperatures were studied by scanning electron microscopy. Typical SEM images recorded for Co films are shown in Fig. 3.2. The films exhibit a featureless morphology upto an annealing temperature of 500°C, indicating their amorphous nature which was further confirmed by XRD measurements. However, at higher annealing temperature, the morphology turns granular in nature.

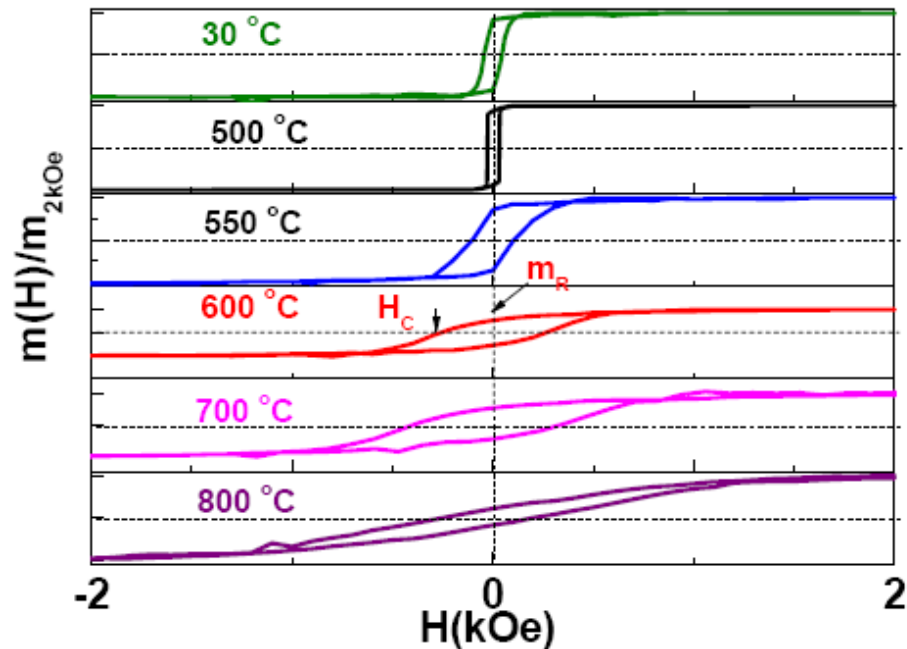


Fig. 3.3 The normalized magnetic moment ($m/m_{2\text{kOe}}$) versus applied field (H) hysteresis loop recorded at 300 K for Co-films annealed at different temperatures T_{an} .

Typical magnetic moment (m) vs applied field (H) plots recorded on different samples mentioned in fig. 3.2 in the field range of ± 2000 Oe at 300 K are shown in Fig. 3.3. During these measurements, the H was applied parallel to the plane of the film. From the m - H loops, the value of coercive field H_C was deduced at 300 K and 10 K (m-H data at 10K not shown), and the obtained results are shown in Fig. 3.4. From Fig. 3.4, it is evident that H_C remains very low until the annealing temperature of 500 °C, after which H_C starts rising and attains a peak (410 Oe) at 700°C. However, at still higher annealing temperature, the H_C decreases. This result is consistent with the SEM morphology shown in Fig. 3.2. The grain growth is not attained until the annealing temperature of 550°C, which yields soft ferromagnetic property of the films. The H_C increases, as the grain size increases owing to the formation of magnetic domains. The H_C decreases at higher annealing temperatures possibly due to the diffusion of Si impurities into the Co-films.

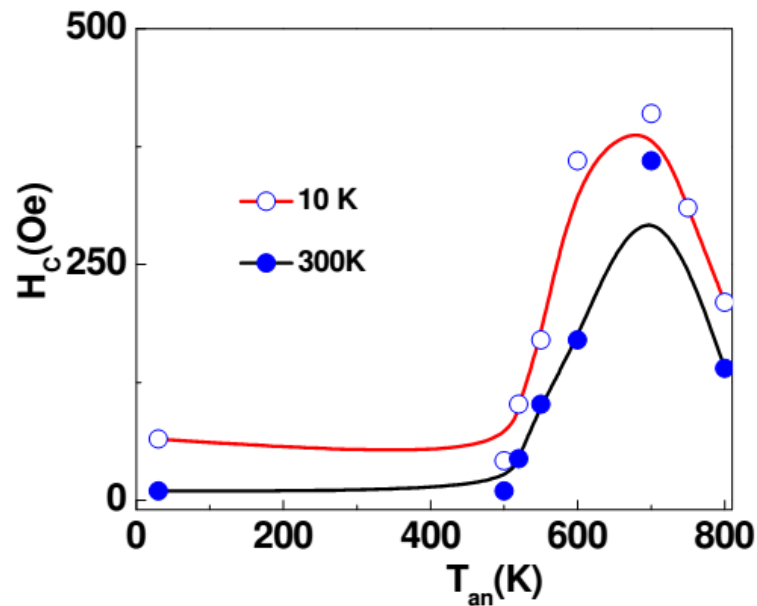


Fig. 3.4: Variation in H_C (10 K and 300 K) for Co-films annealed at different temperatures T_{an} .

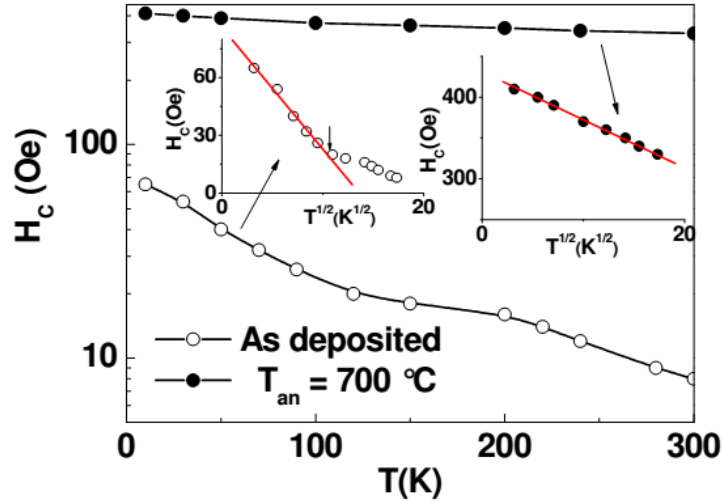


Fig. 3.5: H_C variation with temperature for Co films as deposited (open circles) and Annealed at $700\text{ }^\circ\text{C}$ (closed circles).

The H_C of the films were also investigated as a function of temperature, and the results obtained for the as-deposited Co-films annealed at $700\text{ }^\circ\text{C}$ are given in Fig. 3.5. It is seen that for as-deposited Co-films, the H_C increases significantly as the temperature is lowered down. This is attributed to the very small grain size of the Co, as at high temperature the thermal fluctuation overcomes the magnetic domain orientation. These results are in agreement with those reported by Frolov et al. [82], who observed the change in magnetic properties of nanocrystalline cobalt films annealed above $500\text{ }^\circ\text{C}$. Re-plotting of H_C vs T data shown in the main panel of fig. 3.5 as a function $T^{1/2}$ behavior, as shown in inset of Fig. 3.5, clearly indicates that for as-deposited cobalt films the blocking temperature T_B is lower than 300 K [83, 84]. However, Co-films annealed at $700\text{ }^\circ\text{C}$, exhibit linear behavior in H_C with $T^{1/2}$ until room temperature indicating T_B is higher than

300 K. Due to much larger grain size obtained under this condition, thermal fluctuations have no major effect on the domains. Therefore H_C has a weak dependence on temperature.

The results presented in this Section are important from the viewpoint of the growing bilayers or multilayers. It is evident that the Co-films grown at room temperature are uniform and therefore, ideal for growing bilayers and multilayers. They also possess soft magnetic property. Granular morphology produced when the films are annealed at higher temperatures increases the possibility of surface roughness. Therefore high temperature annealing is not ideally suited for the preparation of bilayer/multilayers. We note that Fe films grow almost in similar fashion as Co. However, Ni has a little different growth, which is described below.

(b) Ni films

Ni films of 100 Å nominal thickness were deposited on Si (111) using DC magnetron sputtering under the conditions identical to those used for Co films.

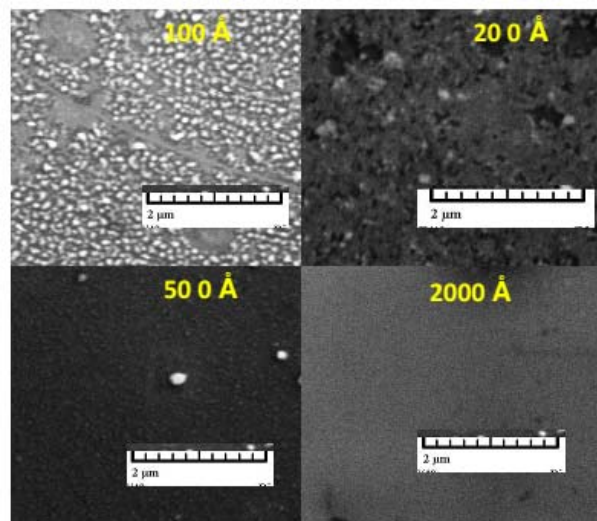


Fig. 3.6: SEM images of Ni films of different thicknesses deposited by sputtering.

The SEM image of such a film is shown in Fig. 3.6 (top-left), which clearly indicates a granular morphology. Therefore, in order to grow smooth Ni films, the film thickness was increased. Typical SEM images of the films of different thicknesses shown in Fig. 3.6 clearly suggest that uniform films are obtained when thickness is greater than 500 Å. It is known that the early stages of thin film formation, i.e. in the thickness range of 50–500 Å, is very sensitive to the processing techniques and parameters used [85, 86].

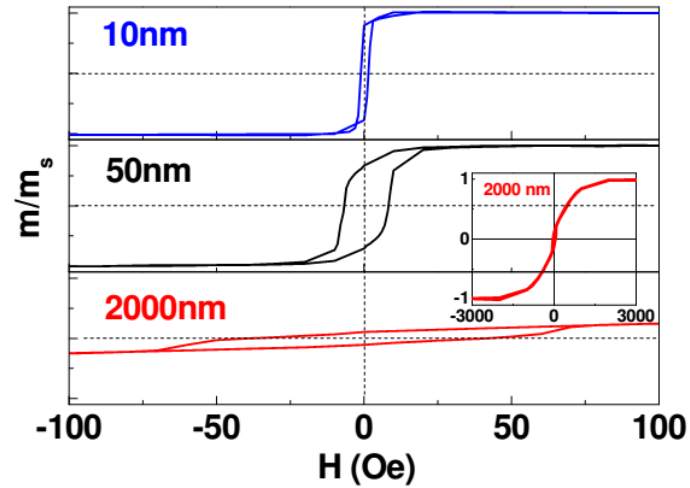


Fig. 3.7: The normalized magnetic moment (m/m_s) versus applied field (H) hysteresis loop recorded at 300 K for Ni-films of different thickness. The full hysteresis loop for 20000 Å Ni films is shown in inset.

H_C and the squareness of hysteresis loop defined as $S = \text{remanent magnetization } (m_R) / \text{saturation magnetization } (m_S)$ for Ni-films (at 300 K) of thickness ranging from 100 to 20000 Å are plotted in Fig. 3.8 as a function of film thickness t . It is seen that H_C increases with t whereas S decreases. This possibly suggests that the easy axis of magnetization, which lies within the plane for low thickness, changes to some random direction with increase in film thickness. Similar behavior i.e. increasing in H_C with t upto

3000 Å was also observed by Kumar et al [87]. However further increase in t resulted in a decrease of H_C .

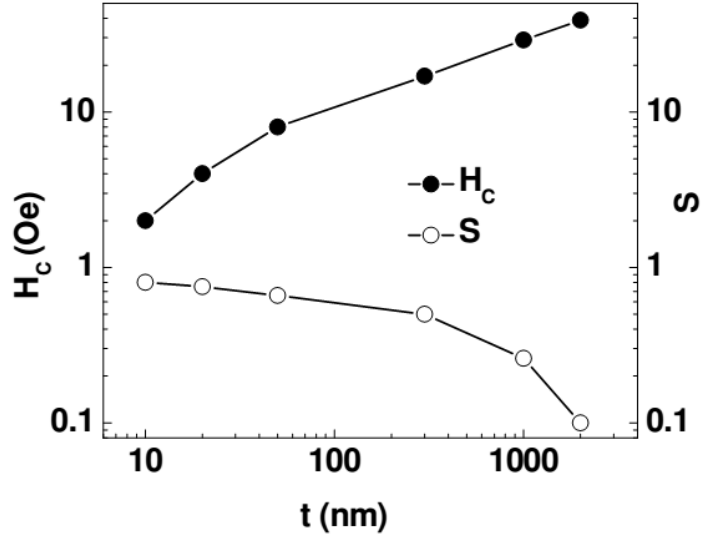


Fig. 3.8: H_C and S plotted with different thickness of sputtered deposited Ni.

(c) Gd films

We have also optimized the growth parameters of the Gd films by DC magnetron sputtering, and found that uniform films are obtained at a thickness of 300 Å. A typical zero field cooled (ZFC) and field cooled (FC) magnetization measurements for an applied field of 100 and 1000 Oe are shown in Fig. 3.9.

The Curie temperature T_{FM} for these films was found to be 290 K which is close to that in bulk Gd. These results are in agreement with those reported by Yamada et al. [88] who observed $T_{FM} \sim 293$ K in a film deposited at a substrate temperature of 600 °C. The value of T_{FM} of ~ 290 K is observed for as-deposited Gd films. A strong irreversibility is seen in ZFC & FC data at 100 Oe while they are reversible at 1000 Oe indicating that 100

$< H_C < 1000 \text{ Oe}$. H_C values extracted from m-H loops recorded at different temperatures (Fig. 3.10) are plotted in Fig. 3.11. H_C increases with decreasing temperature as expected.

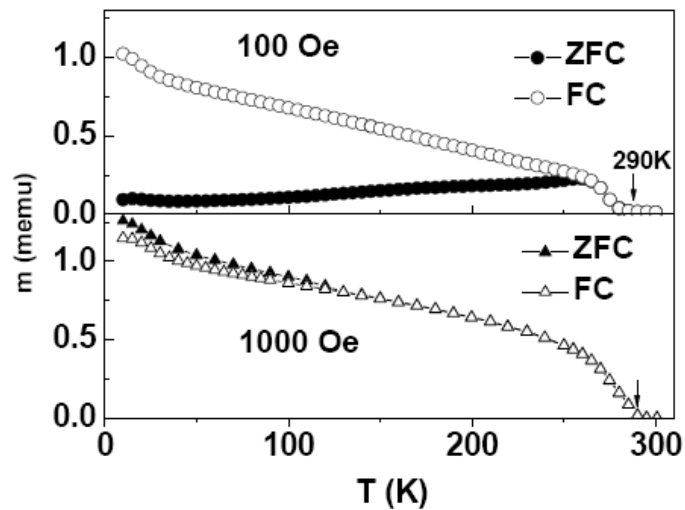


Fig. 3.9: Magnetic moment (m) with temperature (T) is measured in ZFC and FC mode at 100 Oe for 300 Å Gd film.

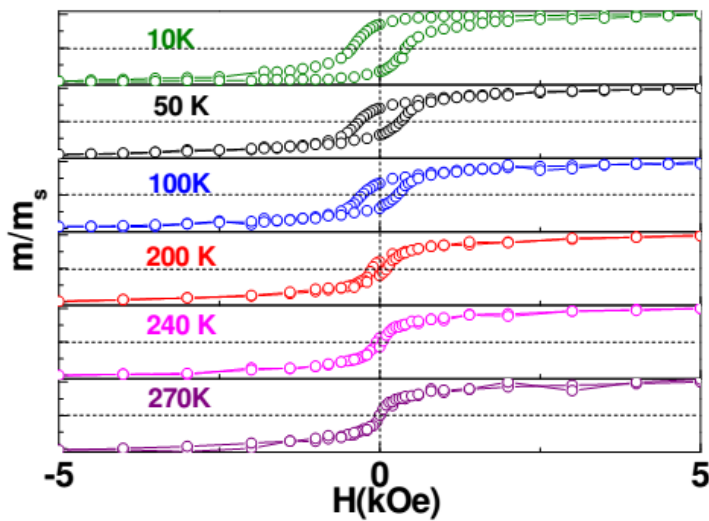


Figure 3.10: Magnetic moment (m) with applied magnetic field (H) at different temperature for Gd film (300 Å) deposited by sputtering.

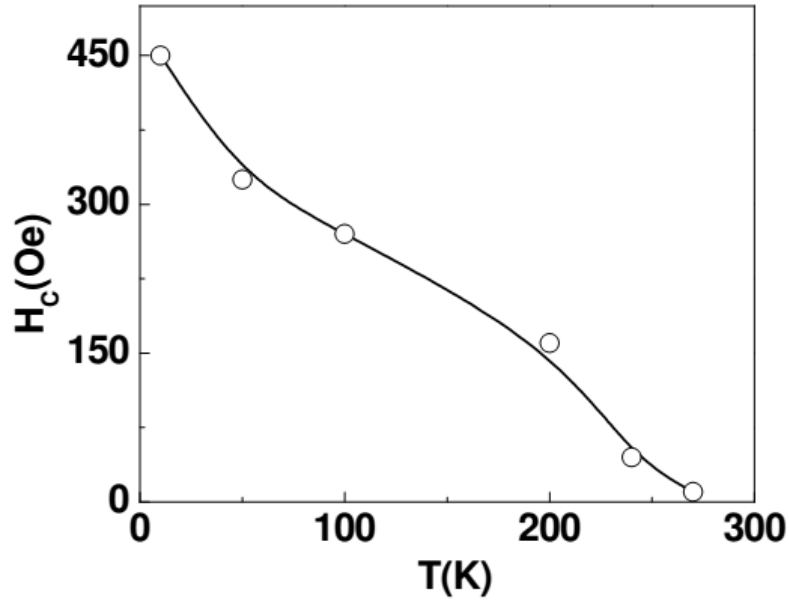


Fig. 3.11: Variation in H_c with temperature for Gd film (300 Å) deposited by sputtering.

3.2.2 Superconducting films

(a) Nb films

Preparation of Nb thin films by sputtering, though widely reported in literature, is difficult as Nb is highly susceptible to gaseous impurities, particularly oxygen. The dissolved impurities not only suppress the superconducting transition temperature but also strongly influence the characteristic length scales and the fields of the superconducting state. Therefore, in the present work we have optimized several deposition parameters, including the base vacuum, sputtering pressure, and sputtering power. It goes without saying that the best base vacuum is essential for obtaining the superconducting Nb films

[89]. However at a base vacuum of 5×10^{-7} mbar, the best achieved by the pumping the sputtering chamber in our system, significant amount of the oxygen is still present. In order to getter this oxygen, Nb (99.999%) was pre-sputtered at a high power of 170 W for 10 minutes, which improved the base vacuum to 1×10^{-7} mbar. Nb films of 500 Å, thickness on Si substrates were prepared soon after pre-sputtering process at room temperature. The four probe temperature dependent resistance data for these Nb films is shown in Fig. 3.12. The films exhibit a sharp zero field superconducting transition, T_{SC} at ~ 9 K. The diamagnetic response shown in Fig. 3.13 also reveals a T_{SC} of ~ 9 K.

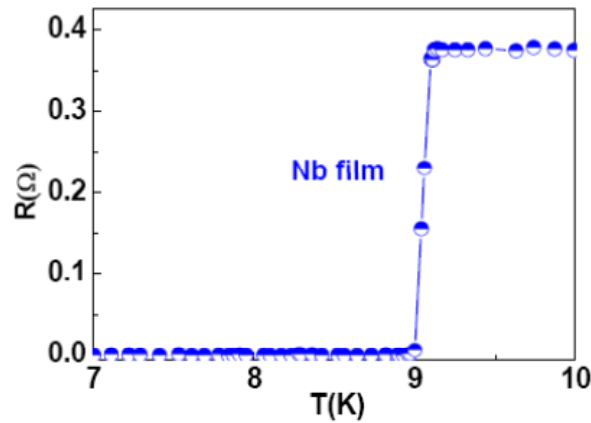


Fig.3.12: Superconducting transition transport electrical resistance with temperature in Nb film.

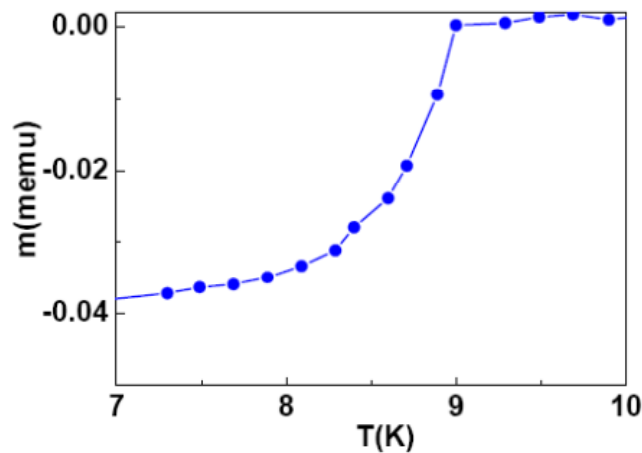


Fig. 3.13: Superconducting transition magnetic moment with temperature in Nb film.

(b) NbN films

The superconducting NbN films can be prepared by reactive sputtering with N_2 using pure Nb target. Here we describe the optimization of various parameters for obtaining NbN on Si(111) substrates. The reactive sputtering was carried out using a mixture of high purity argon and nitrogen (99.999 %) gases. The total pressure of argon and nitrogen is 6.3×10^{-3} mbar, with flow rates of 7 SCCM for nitrogen and 35 SCCM for argon. Following two sets of experiments were carried out.

(i) *Deposition of films at room temperature but varying the sputtering power between 54 -135 W.* The XRD patterns of the NbN films grown at different powers are shown in Fig. 3.14. It is seen that the intensity of (111) and (200) reflections increases with sputtering power, indicating higher the power better is the chance of formation of NbN phase. The normalized resistance of these films are shown in Fig. 3.15.

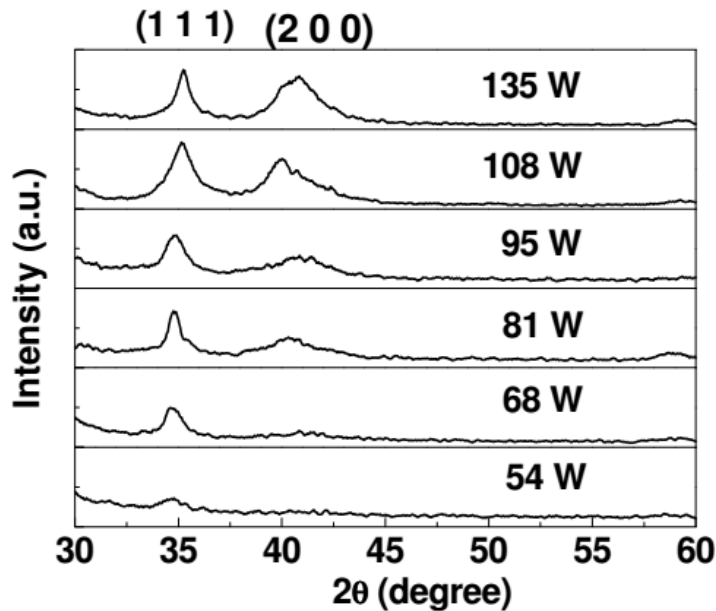


Fig. 3.14: XRD patterns are recorded for all films of NbN (50nm) deposited at different sputtering power from 54 W to 135W.

The results show that at low deposition power (54 W), films are semiconducting and do not exhibit superconductivity down to 4.2 K. Beginning at 68 W, T_{SC} monotonically increases with sputtering power. A highest T_{SC} of 10.8 K was obtained for a sputtering power of 135 W, which is far below the bulk T_{SC} of NbN. Increase T_{SC} with sputtering power was also observed by Chockalingam et al. [90].

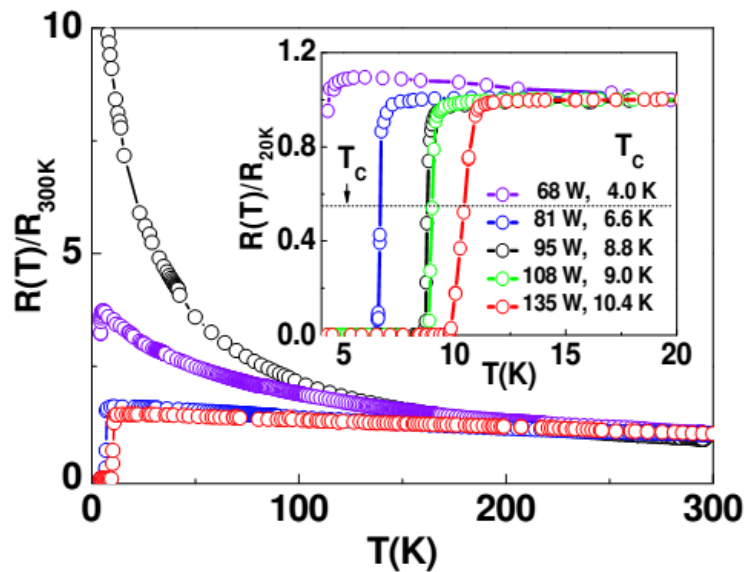


Fig. 3.15: A temperature dependent resistance is measurement from 4.2 K to 300 K. Inset the superconducting transition.

(ii) *Deposition of films at sputtering power of 135 W but varying the substrate temperature between 30 and 800 °C.* The XRD patterns of the films grown at different substrate temperatures shown in Fig. 3.16 clearly show the improved crystallization of the NbN films with increasing substrate temperature. It is seen that NbN has a preferred orientation of (111) at 600 °C, which is same as that of Si (111) substrate. However, at substrate temperature of 800 °C, the preferred orientation of the films turns out to be (200).

The R vs T plots of the films deposited at different substrate temperatures are shown in Fig. 3.17. It is seen that the highest T_{SC} of 16.2 K is obtained at 600 °C, which is close to the bulk T_{SC} of the NbN. At a substrate temperature of 800 °C, T_{SC} slightly decreases to 15.8 K owing to the chemical reaction with the substrate.

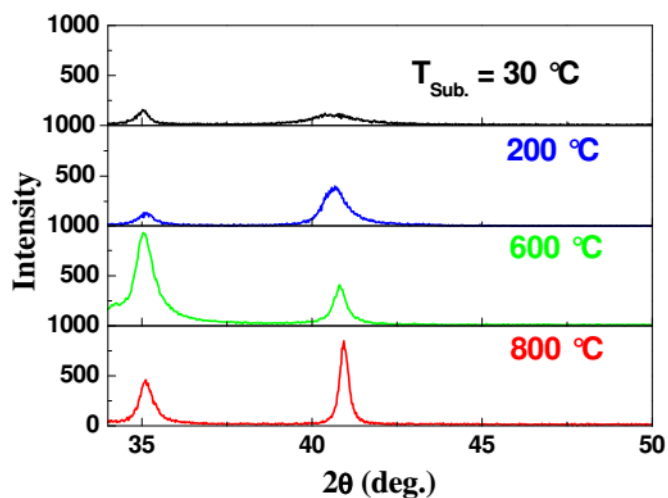


Fig. 3.16: XRD patterns are recorded for all films of NbN (500Å) deposited at different substrate temperature $T_{Sub.}$ from room temperature to 800 °C.

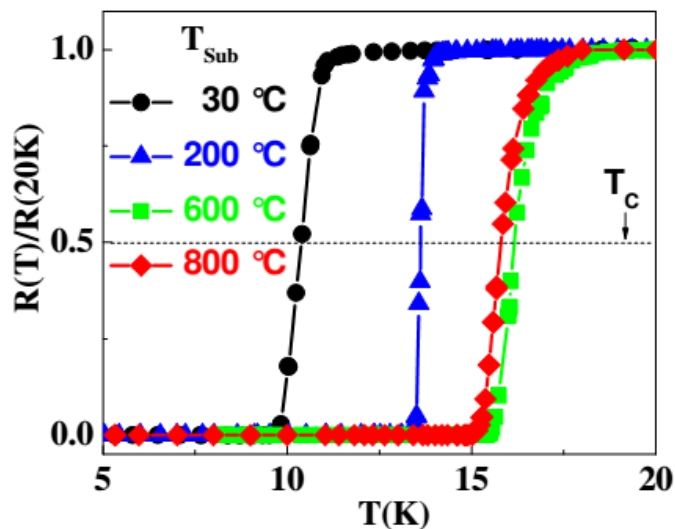


Fig. 3.17: Superconducting transition in films of NbN (500Å) deposited at different substrate temperatures $T_{Sub.}$.

3.3 Metallic S/F bilayers

3.2.1 Ferromagnetic/ non ferromagnetic bilayers

In order to gain hands on experience in the growth of metallic superconductor/ferromagnetic bilayers and multilayers, we have selected simple Fe/Au bilayers. These bilayers were repeated to form stack of multilayers, and their transport and magnetic properties were investigated as a function of thickness. For this purpose, [Fe (50Å) /Au (100 Å)]₁₀ multilayer (i.e. superlattice of ten bilayers) were deposited on Si substrates using magnetron sputtering at room temperature. In some cases the superlattices were vacuum annealed at 100 °C and 150 °C.

The XRR measurements performed on as-deposited and vacuum annealed superlattices are shown in Fig. 3.18 (a). From these results it is seen that with increase in annealing temperature: (i) the reflectivity at higher Q value is reduced, suggesting an increase in interlayer roughness; and (ii) the position of Bragg peaks gradually shifts to larger Q values, which can be due to the release of strain causing reduction in the bilayer thickness. The normalized electron scattering length density (SLD) profile for a bilayer which gave best fit to XRR data are shown in Fig. 3.18(b). On annealing at 100 °C for one hour Fe/Au interface roughness increases from 9 Å to 13 Å. Further annealing at 150°C for one more hour reduces the roughness to 11 Å.

Fig. 3.19 (a) shows the m-H hysteresis curve (open circle with line) and MR data (open triangle) for superlattices annealed at 100°C for one hour, which confirms the

ferromagnetic nature of the superlattices. The magnetoresistance (MR) data for as-deposited sample and vacuum annealed superlattices are shown in Fig. 3.19. No significant change in magnetization was observed on annealing. However, a reduction in MR was observed on annealing. The MR for annealed sample at 100°C and at 150°C are 0.14% and 0.18% respectively, compared to the as-deposited sample (~0.30%). These results are consistent with XRR data that the interface roughness increases on annealing the superlattices.

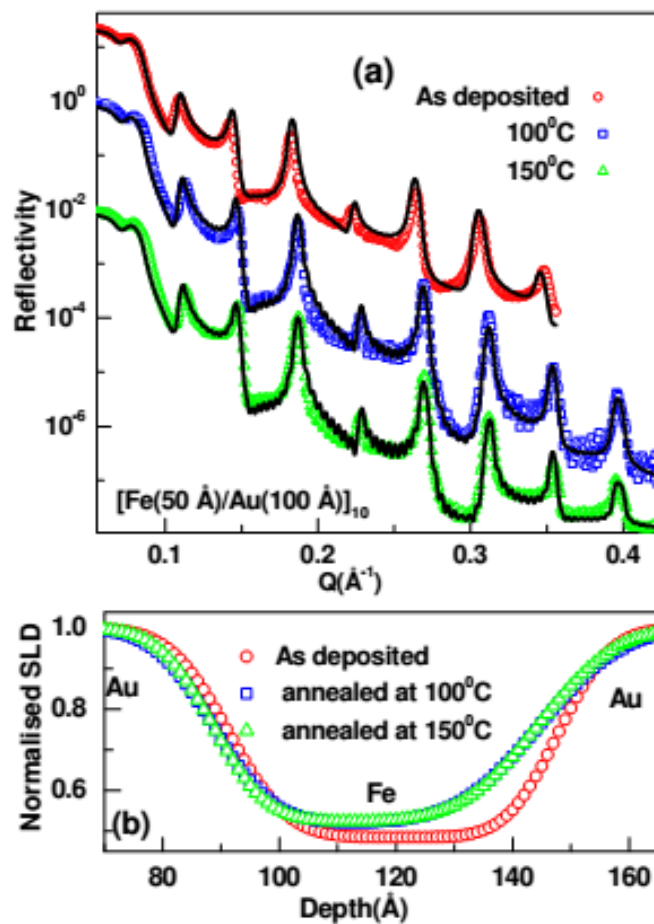


Fig. 3.18: (a): Specular X-ray reflectivity measurements from as-deposited multilayer (open circles) and sample annealed at 100°C (open squares) and 150°C (open triangles) (b) shows the normalized SLD profiles at interfaces extracted from fit to XRR data.

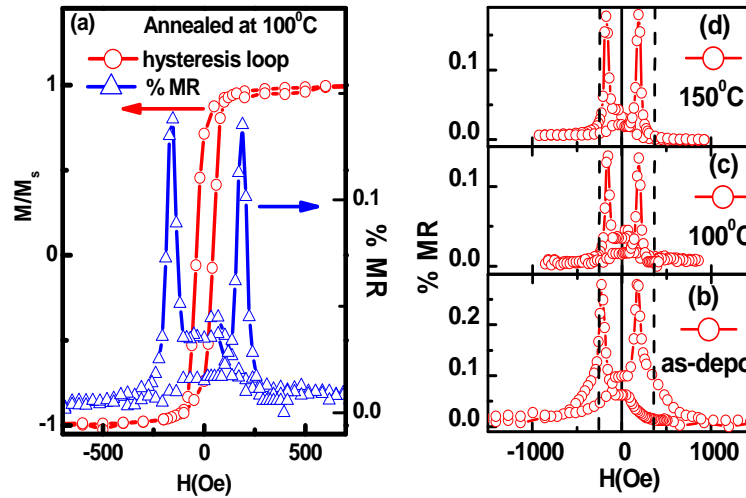


Fig 3.19: (a): $M(H)$ hysteresis curves (open circles) and magnetoresistance (open triangles) as function of applied magnetic field for $[\text{Fe}(50 \text{ \AA})/\text{Au}(100 \text{ \AA})]_{10}$ multilayer after annealing at 100 °C for one hours. (b): MR vs H for as-deposited (b) and sample annealed at 100 °C (c) and 150 °C (d).

Further, a series of Fe/Au multilayer samples of varying Fe and Au layer thickness were grown on Si substrate by DC magnetron sputtering system. In the first series; ten bilayers of Fe (variable thickness of 30, 50 and 100 Å) and Au (fixed thickness of 50 Å) were grown and the structure can be represented as: Si substrate/ $[\text{Fe}(t_{\text{Fe}} \text{ \AA})/\text{Au}(50 \text{ \AA})]_{10}$, with $t_{\text{Fe}} = 30, 50$ and 100 \AA , respectively. In the second series; ten bilayers of Fe (fixed thickness of 50 Å) and Au (variable thickness of 50, 100 and 150 Å) were grown and the structure can be represented as: Si substrate/ $[\text{Fe}(50 \text{ \AA})/\text{Au}(t_{\text{Au}} \text{ \AA})]_{10}$, with $t_{\text{Au}} = 50, 100$ and 150 \AA , respectively. Typical magnetization curves (normalized) with in-plane magnetic field for one multilayer $[\text{Fe}(50 \text{ \AA})/\text{Au}(50 \text{ \AA})]_{10}$ at room temperature (open circle with line) and 5 K (open triangle with line) are presented in Fig. 2.20 (a). This multilayer sample shows the characteristic magnetic behaviour of a good ferromagnet with well

defined saturation value and a remanent magnetization (M_r) $\sim 77\%$ of the saturation magnetization (M_s). Fig. 2.20(b) shows the variation of M_r/M_s ratio as a function of layer thickness. For all the samples the remnant magnetism is in the range of 75 % to 78 % of the saturation magnetism. MR measurements were carried out at room temperature for all. Fig. 2.20(c) depicts the MR measurements from same multilayer same sample at room temperature. The variation of MR at room temperature for different multilayers (different thickness of Fe and Au) are represented in Fig. 2.20(d). MR depends strongly on the magnetic moment in the Fe layer and on coupling between the Fe layers through non-magnetic Au. For higher thickness of Au layer there was a strong drop in MR most likely due to reduced coupling between the magnetic layers.

Both MR values and M_r are increasing with ferromagnetic (Fe) thickness and decreasing with non-ferromagnetic (Au) thickness in Fe/Au multilayer.

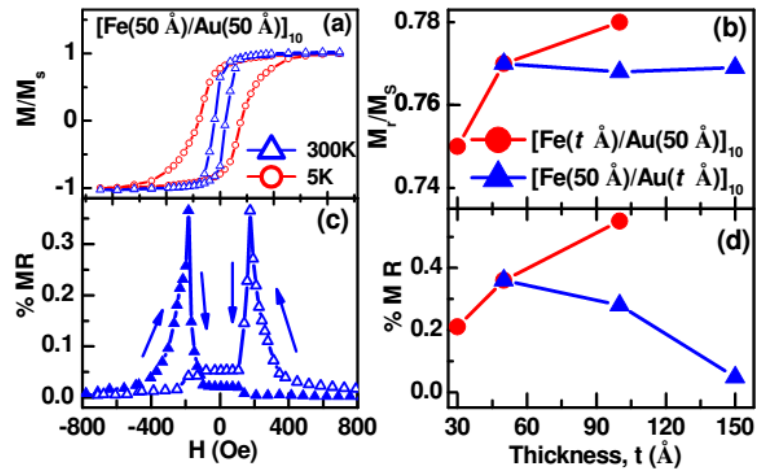


Fig.3.20: $M(H)$ hysteresis curves for $[\text{Fe}(50 \text{ \AA})/\text{Au}(50 \text{ \AA})]_{10}$ multilayer sample at 5 K (open triangles) and 300 K (open circles). (b): variation of M_r/M_s ratio with thickness of Fe (closed circles) and Au (closed triangles) layers. (c): MR vs H plot for $[\text{Fe}(50 \text{ \AA})/\text{Au}(50 \text{ \AA})]_{10}$. (d): variation of MR with thickness of Fe (closed circles) and Au (closed triangles) layer.

3.3.2 Proximity effect in Nb (500 Å)/Ni (500 Å) bilayers

Bilayers of Nb (500 Å)/Ni (500 Å) were deposited on Si (111) substrates by DC magnetron sputtering under optimized growth conditions, as discussed in earlier section. To measure the thickness and roughness of the interface of Nb (500 Å)/Ni (500 Å) bilayers, XRR measurements were carried out and the results are presented in Fig. 3.21. The best fit (solid line) to the experimental data (open circles) yielded the thickness of 540 Å and 490 Å respectively for Nb and Ni layers. The roughness of Si/Nb, Nb/Ni and Ni/air interfaces are 15, 18, and 12 Å respectively. These results show high quality of the Nb/Ni bilayers.

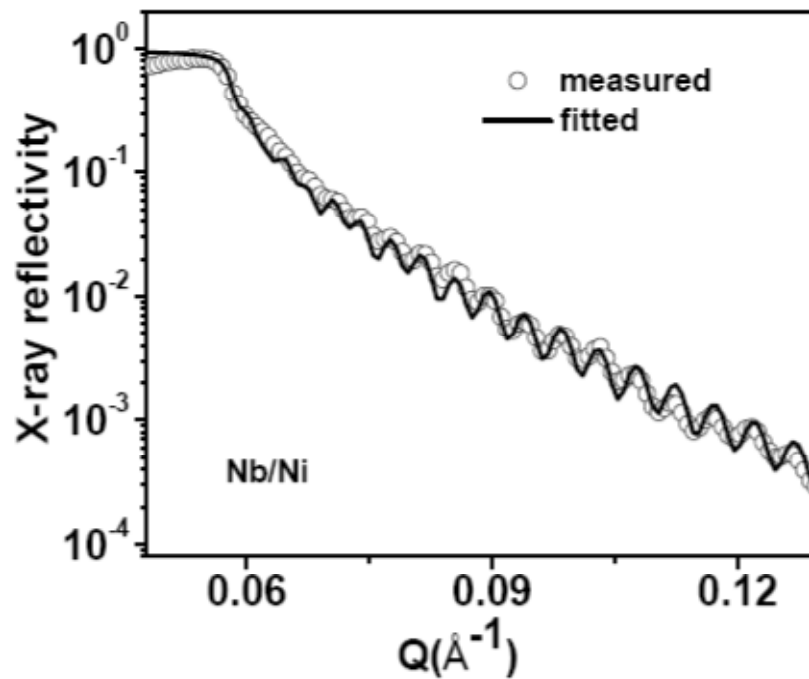


Fig. 3.21: XRR measurement on Nb/Ni bilayers

(a) Superconducting properties

Zero field cooled (ZFC) magnetization data of the Nb/Ni bilayer under a field of 50 Oe applied parallel to the substrate plane is shown in Fig. 3.22. The superconducting transition T_{SC} corresponding to Nb layer is suppressed to 7 K due to proximity of ferromagnetic Ni. The R-T plot shown in the inset of Fig. 3.21, reveals T_{SC} of ~ 7.1 K, which is in agreement with magnetization data.

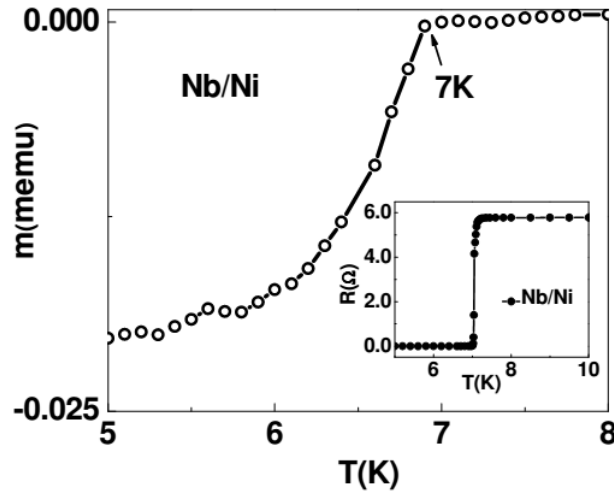


Fig. 3.22: magnetic moment measured with temperature in ZFC mode at 50 Oe for Nb/Ni bilayers. Inset show the superconducting transition in transport measurements.

(b) Magnetic properties

The m-H hysteresis loops for the Nb/Ni bilayers recorded at 10 K ($> T_{SC}$) and 5.5 K ($< T_{SC}$) are shown in Fig. 3.23. Hysteresis loop recorded at 10 K clearly shows the ferromagnetic nature from the Ni layer. The saturation and coercive fields of Ni layer are found to be 100 Oe and 55 Oe respectively indicating soft ferromagnetic nature of Ni layer.

However, the magnetic hysteresis loop shown in Fig. 3.23, measured at 5.5 K shows a peculiar behavior i.e. the magnitude of magnetization increases with decreasing field, which is attributed to the presence of both diamagnetic (due to superconductivity in Nb layer) and ferromagnetism (in Ni bilayer). Since Ni has a ferromagnetic transition (T_{FM}) of ~ 630 K contribution of Ni layer to the total moment of Nb/Ni bilayer is expected to be nearly same at 5.5 K and 10 K. Thus, the diamagnetic contribution in the Nb/Ni bilayer obtained by subtracting the m-H data recorded at 10 K from the one at 5.5 K is shown in Fig. 3.23, which is a characteristic of a superconducting film, except a sharp peak occurring at ~ 55 Oe, which corresponds to the coercive field of Ni layer.

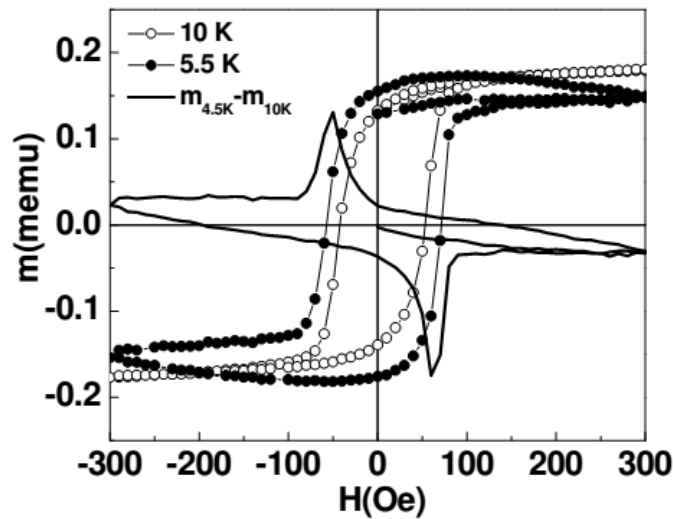


Fig. 3.23: The m-H hysteresis loops for the Nb/Ni bilayers were recorded at 10 K ($> T_{SC}$) and at 5.5 K ($< T_{SC}$).

The typical current-voltage characteristics of the Nb/Ni bilayers at different temperature under demagnetized condition are shown in Fig. 3.24. These curves clearly show the two steps, which can be correlated to the inhomogeneous superconductivity owing to the domain wall superconductivity.

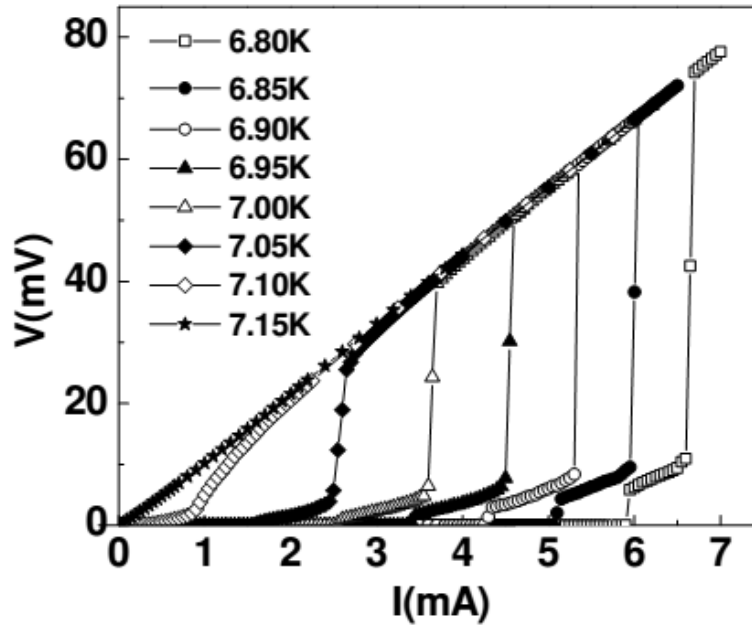


Fig. 3.24: Two step V-I curves of Nb/Ni bilayer at different temperatures.

In principle, the R-T curve of the Nb/Ni bilayers should have shown two steps like transition, which however could not be observed possibly due to the very soft ferromagnetic nature of the Ni.

3.3.3 Domain wall superconductivity in Nb (500 Å)/Gd (500 Å) bilayers

In this Section, we investigate the domain wall superconductivity in Nb/Gd bilayers. Gd was deliberately selected as it is a ferromagnet with T_{FM} of 290 K, i.e., below room temperature. Further Nb and Gd are immiscible and therefore high quality interfaces can be achieved. Nb(500 Å)/Gd(300 Å) bilayers were deposited on Si (111) substrates at room temperature using dc magnetron sputtering. XRR data showed high quality of the

bilayers with interface roughness $< 12 \text{ \AA}$. The magnetic and superconducting properties of these bilayers are presented below.

(a) Magnetic Properties

A typical ZFC and FC magnetization data on Nb/Gd bilayers under a field of 100 Oe applied parallel to the film is shown in Fig. 3.25. Curie temperature T_{FM} was found to be $\sim 285 \text{ K}$, which is close to that observed for Gd films (see Fig. 3.9).

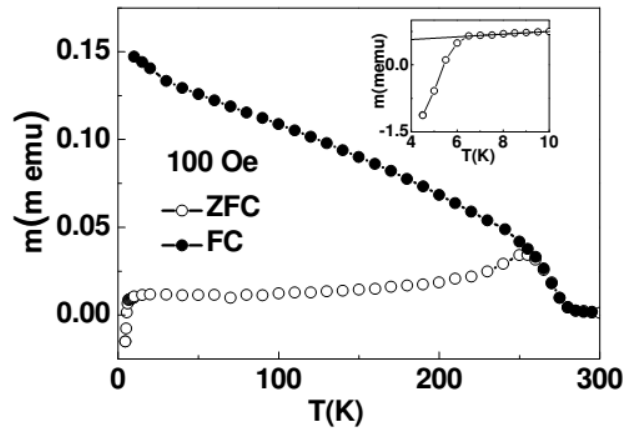


Fig. 3.25: Magnetic moment (m) with temperature (T) is measured in ZFC and FC mode at 100 Oe for bilayers of Nb/Gd.

Onset of the diamagnetic behavior (inset of Fig. 3.24) of the bilayers in the ZFC curve gives the superconducting transition of the Nb layer $T_{SC} \sim 6.6 \text{ K}$, lower than that measured for pure Nb films (see Fig. 3.13), which is attributed to proximity of ferromagnetic Gd layer.

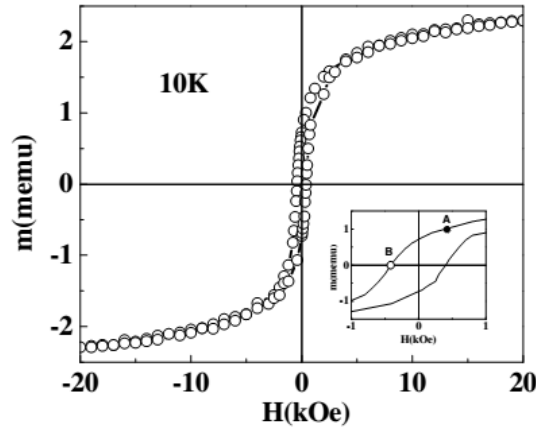


Fig. 3.26: Magnetic moment (m) with applied field measured at 10 K for bilayers of Nb/Gd.

Magnetic hysteresis loop of the Nb/Gd bilayers shown in Fig. 3.26 was measured at 10 K, just above the T_{SC} of the bilayers. The coercive field is 400 Oe, nearly same as that of pure Gd films. The saturation of magnetization does not occur even upto 20 kOe. However, the non-saturation of Gd can possibly be attributed to polycrystalline nature of the films and the canting of ferromagnetic moments away from the c-axis at low temperatures. It is found that the canting angle is as large as 50 degree in nanocrystalline Gd, which itself can be size dependent [91].

(b) Superconducting Properties

In order to investigate the proximity effect of ferromagnetic Gd layer on the superconducting properties of Nb/Gd bilayers, electrical transport measurements were carried out. Typical R-T plot for the bilayer is shown in Fig. 3.27 along with the R-T plot of pure Nb films for comparison. Following inferences can be drawn: (i) the onset of superconducting transition temperature for bilayers decreases from 9.0 K to 6.6 K (also

seen from the magnetization measurements shown in Fig. 3.25); and (ii) for bilayers the transition to superconducting state takes place in two steps, indicating presence of two types of superconducting transitions. This was however not observed in the case of Nb/Ni bilayer as Ni is a soft ferromagnet.

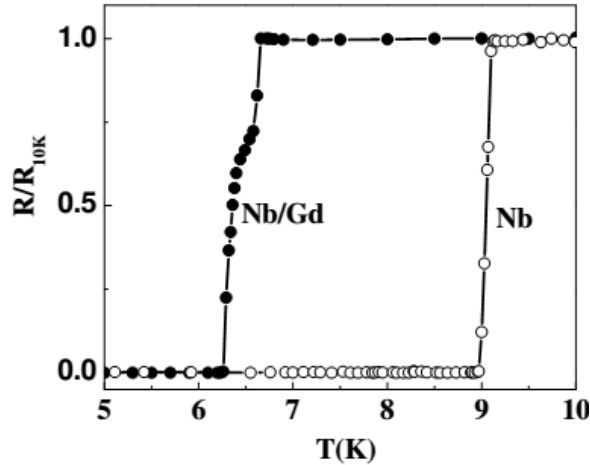


Fig. 3.27: Superconducting transition in transport electrical resistance measured with increasing temperature from 4.5 K to 10 K for Nb Film and bilayer of Nb/Gd.

Two step superconducting transition in bilayers is attributed to the differing pair breaking field experienced by the Nb film lying above the domains and that lying above the domain wall region (Fig. 3.28) resulting in a phenomenon analogous to the domain wall superconductivity in superconducting films deposited on insulating ferromagnets where the influence of exchange field on the superconductor is absent [89, 92-96]. Diffusion of charge carriers of all polarities into the Nb film from the domain wall region of Gd film lying below results in a lower suppression of T_{SC} so long as the width of the domain wall is smaller than the coherence length of the cooper pairs. On the other hand carriers diffusing into the region of Nb film lying above the FM domain of Gd are unipolar,

causing a larger depression of T_{SC} . Therefore, Nb film lying above the network of domain walls exhibits higher transition temperature marked as T_{SC}^W while that lying directly on the domains exhibits lower transition marked as T_{SC}^D . Thus the Nb layer would exhibit inhomogeneous superconductivity with $T_{SC}^W > T_{SC}^D$.

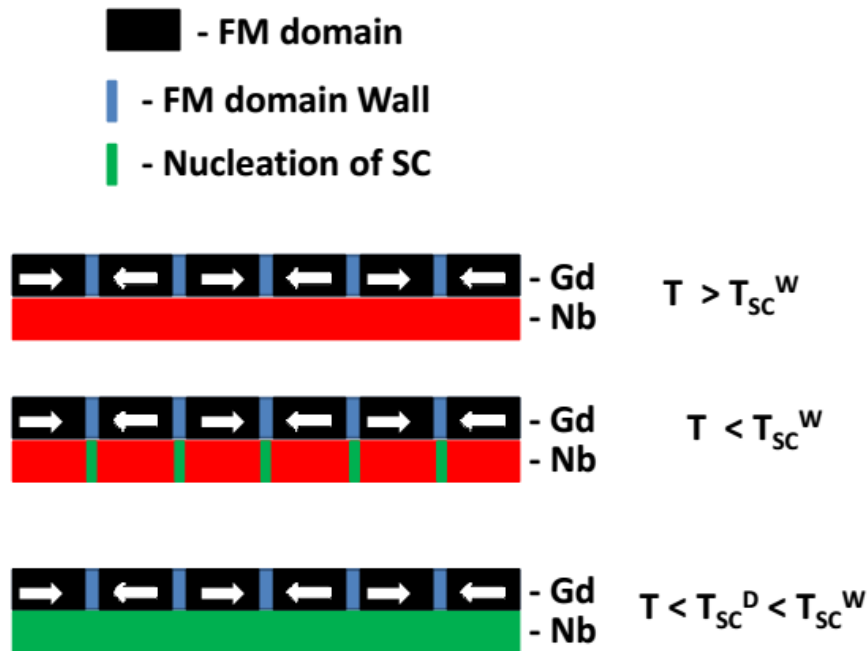


Fig. 3.28: Schematic diagram of nucleation of domain wall superconductivity in the Nb layer of Nb/Gd bilayer where ferromagnetic Gd layer have magnetic domains with domain walls.

In order to understand the role of domains on the two-step superconducting transition in Nb/Gd bilayers, R-T plots (Fig. 3.29) were recorded at different magnetic fields. From this figure following inference can be drawn: while T_{SC} decreases with increasing applied field, the transition broadens and the gap between the two transitions disappears. This is

attributed to the fact that at very high magnetic field, Gd domains align along the field, which diminishes the domain walls, and hence diminishes the high T_{SC} parts in the Nb film.

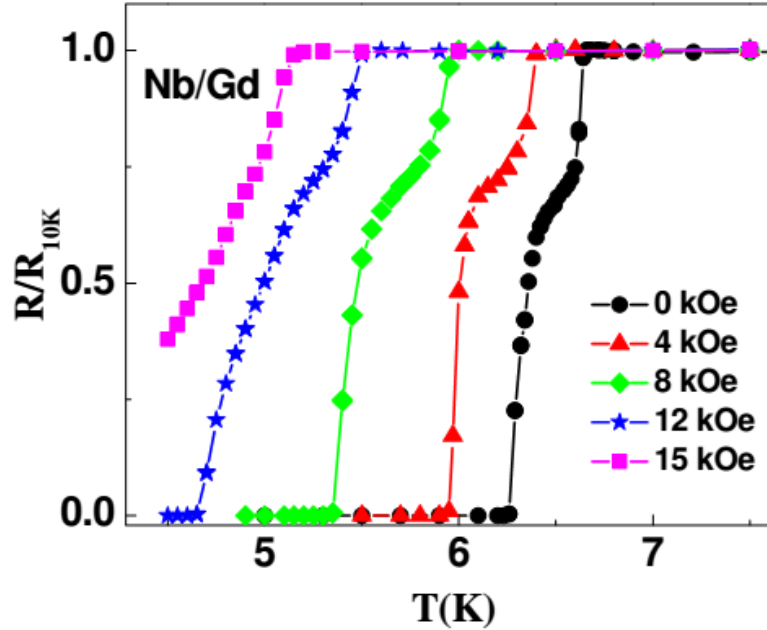


Fig. 3.29: Superconducting transition in transport electrical resistance measured with increasing temperature from 4.5 K to 10 K for Nb Film and bilayer of Nb/Gd.

Following experiment clearly demonstrates the effect of domains on the SC transition. Note the m-H loop of the bilayer shown in the inset of Fig. 3.29. Two points A and B, corresponding to the same magnitude of applied field (+400 and -400 Oe) but having a high (magnetized state) and zero magnetic moments (de-magnetized state), respectively. The point B corresponds to the coercive field of the Gd layer. The R-T plots recorded by establishing the sample under conditions at A and B are shown in the inset of Fig. 3.30. It is clearly seen that the T_{SC} in the case of condition A (magnetized state) is 40 mK lower than that under condition B (de-magnetized state). In the case of Nb/permalloy bilayer similar experiments show increase in T_{SC} of 10 mK in de-magnetized state [95].

Further, we present voltage - current characteristics at 6.15 K under conditions A and B in Fig. 3.31. It is evident that the critical current in the case of de-magnetized state is substantially higher (~8%) than that in the case of magnetized state, which is not only attributed to the higher T_{SC} in the former case but possibly also due to the additional pinning due to attractive interaction between the domain walls in FM layer and flux vortices in the Nb film as it may be noted that such a high enhancement in critical current cannot be accounted solely by 40 mK increase in T_{SC} .

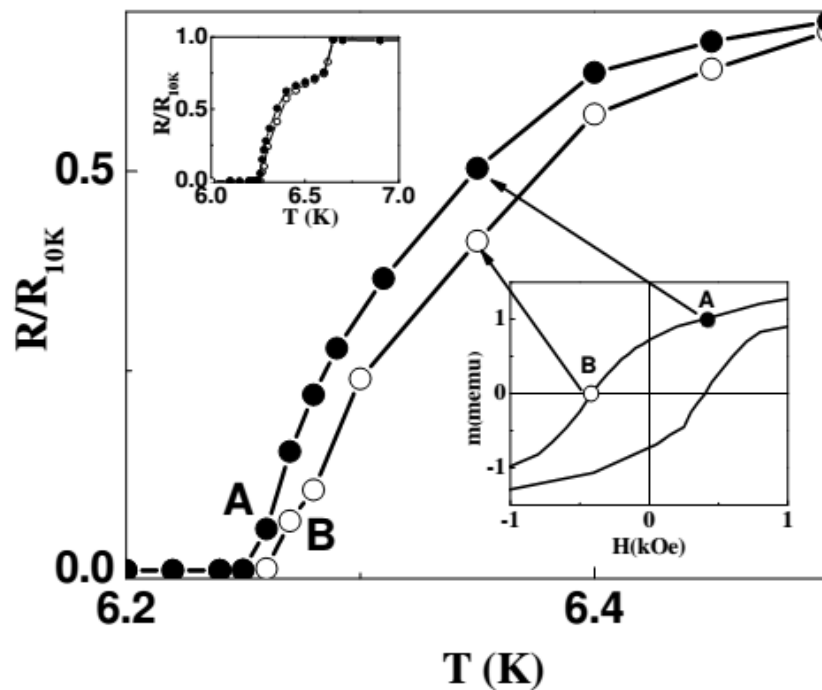


Fig. 3.30: History dependent resistances versus temperature (R-T) curves are recorded with same field (400 Oe) in two different magnetic domains structures.

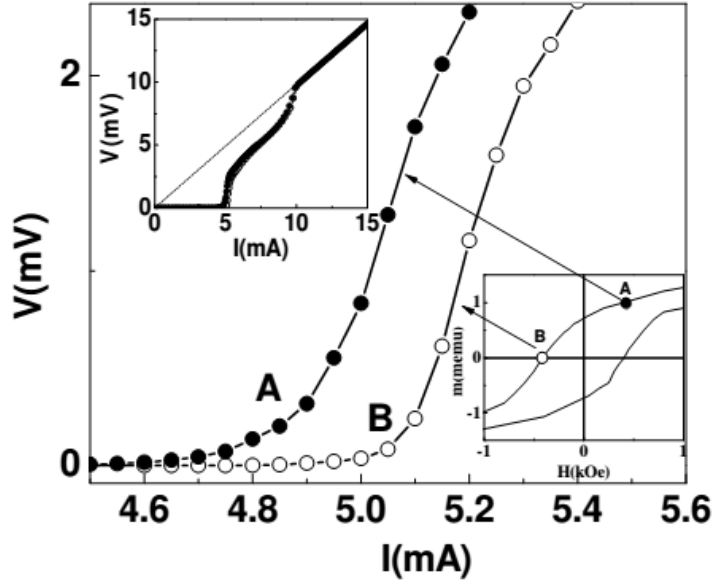


Fig. 3.31: History dependent resistances versus temperature (R-T) curves are recorded with same field (400 Oe) in two different magnetic domains structures.

3.4 Proximity effect in NbN/NbO/Co trilayers

In the Nb/Ni and Nb/Gd bilayers it was demonstrated that the magnetic layer directly affects the superconductivity via exchange field as well as exchange of charge carriers. In order to investigate the effect of only dipolar field on the superconductivity, we have grown a NbN(600 Å)/NbO(100 Å)/Co(100 Å) trilayer (NbO is insulating) using DC magnetron sputtering on Si (111) substrates at room temperature.

The m-H hysteresis loop of the trilayer recorded at 10 K is shown in the inset of Fig. 3.32, which shows the ferromagnetic characteristics of Co layer. Co layer shows saturation at >2 kOe with a coercive field of ~250 Oe. The R-T plot of the trilayer is shown in Fig. 3.32, which clearly shows a T_{SC} of 6.5 K. The R-T plots were recorded at a current of 0.2 mA. For comparison, the R-T plot of the pure NbN films is also shown in

the same figure. Comparing the two curves we note (i) T_{SC} is nearly same for NbN film and trilayer, indicating presence of NbO and Co layers does not affect T_{SC} ; and (ii) observation of the presence of re-entrant resistance for trilayers at temperature below T_{SC} .

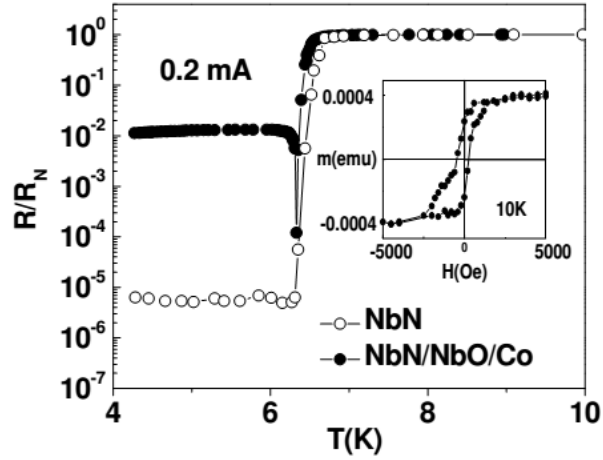


Fig. 3.32: Resistance versus temperature plot of a NbN/NbO/Co trilayer and NbN film measured at applied current of 200 μ A. Inset Inset shows magnetization hysteresis curve measured at 10 K showing ferromagnetic nature of the film.

R-T plots measured with different currents between 0.01 mA and 1mA are shown in Fig. 3.33. It is evident that the re-entrant resistance with a resistance minimum (T_{MIN}) persists over a wide range of currents: We conclude (i) T_{MIN} shifts to lower values on increasing the probe current, which is attributed to the temperature dependent critical current of the superconducting layer, (ii) the value of the reentrant resistance decreases with increasing probe current i.e. highest for the lowest probe current.

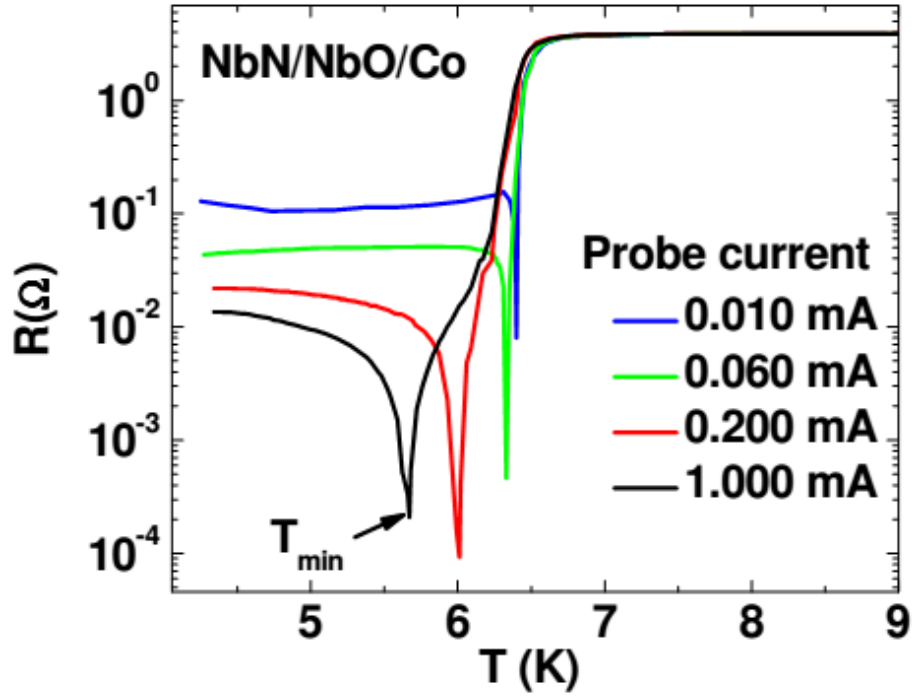


Fig. 3.33: Temperature dependent resistance of NbN/NbO/Co trilayers measured at different probe currents.

These observations have been explained on the basis of the dynamics of vortices and anti-vortices produced in superconducting NbN film due to the ferromagnetic Co layer, as schematically shown in Fig. 3.34. For any probe current, below T_{SC} (which decreases with increasing probe current), the random ferromagnetic domains of Co generate a bound vortex - anti-vortex pairs in NbN layers. In an earlier studied by I. F. Lyuksyutov et al [97] and Feldman et al [98] have predicted a resistive state in SC layer with magnetic dots.

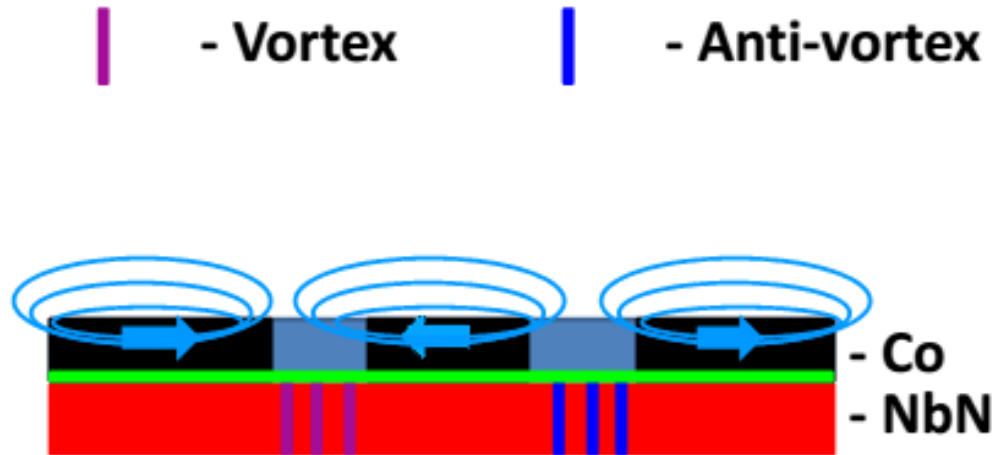


Fig. 3.34: Schematically diagram of production of vortex and anti vortex in NbN due to stray field of Cobalt layer.

Movement of vortex- anti-vortex pairs generates a resistance in the superconductor. When the probe current is very small (e.g. 0.01 mA), the T_{SC} is quite high (i.e. 6.5 K). At high temperature, the thermal energy is quite high, which leads to the instantaneous break of vortices/ anti-vortices pairs, and hence, a sharp rise in the re-entrant resistance. As the probe current increases, the T_{SC} decreases, which results in the lower thermal energy for the breaking of vortices/ anti-vortices pairs. This leads not only the slow increase in the re-entrant resistance but also its values remain low.

3.6 Conclusions

In this chapter, we present magnetic and transport studies on metallic heterostructures grown by DC magnetron sputtering. We have grown several Fe/Au multilayers and studied the effect of post-deposition annealing temperature on the interface

quality of the multilayers using X-Ray reflectivity measurements and correlated to the observed magnetoresistance data. Several bilayers of Nb or NbN with metallic ferromagnetic materials were prepared. Nb/Ni bilayers exhibited two-step resistive transition as observed from current-voltage characteristics. Further, two step transition in the temperature dependent resistance analogous to the domain wall superconductivity observed in Superconducting films deposited on insulating ferromagnets [92] was observed in Nb/Gd bilayers. This was attributed to the domain structure in the underlying ferromagnetic Gd film. We presented an observation of re-entrant resistive transition below T_{SC} in NbN/NbO/Co trilayers. This resistive state was attributed to a vortex dynamics in superconducting NbN layer produced by stray field of Co layer.

**Oxide superconductor/ferromagnet
heterostructures: Growth and
proximity effects**

4.1 Introduction

Due to their matching of lattice constants, superconducting $\text{YBa}_2\text{Cu}_3\text{O}_{7-\delta}$ (YBCO) and ferromagnetic perovskite manganites $\text{La}_{2/3}\text{Ca}_{1/3}\text{MnO}_3$ (LCMO) or $\text{La}_{2/3}\text{Sr}_{1/3}\text{MnO}_3$ (LSMO) are amenable to epitaxial thin film growth with a wide variety of substrate options such as SrTiO_3 (STO), LaAlO_3 (LAO), etc. Heterostructures of these materials grown with high interface quality are ideal candidates for investigating the interaction between mutually antagonistic SC and FM orders. We present a detailed study on growth of YBCO, LCMO and LSMO thin films and heterostructures are prepared by pulsed laser deposition. Structural aspects of LCMO and LSMO films grown on different substrates with varying extents of lattice mismatch and lattice strain and their influence on the magnetic properties are discussed in detail. The magnetoelastic coupling makes the effect of lattice strains very important factor in these materials. Besides varying the substrate, lattice strain can also be introduced by varying the oxygen pressure (P_{O_2}) employed during deposition.

The mainstay of this chapter is the study of magnetic proximity effect in manganite / cuprate heterostructures. We recall the very well established existence of a long range coupling between superconducting cuprate films through ferromagnetic LCMO layers [47, 48, 99]. This is surprising because we know in metallic superconductor / ferromagnet heterostructures, this coupling is of very short range [18, 49]. Further, it is seen in many studies on oxide superconductor / ferromagnet heterostructures, onset of superconductivity modifies the magnetic state of the ferromagnet [39]. We also know that the application of a strain on the substrate affects the magnetic state of the ferromagnetic layer in a FM/SC structure [39]. The aim of our study is to understand if a superconductor separated

electrically from a ferromagnet can influence the magnetic layer, if so what the thickness of the insulator required to decouple the superconductor from the ferromagnet should be. For such study, it is essential to prepare high quality samples with well defined thickness and high interface quality.

The trilayer samples with insulating layers are grown using pulsed laser deposition and characterized by XRD, XRR and magnetization measurements. We studied proximity effect in these structures by polarized neutron reflectivity (PNR) measurements. Detailed analysis of PNR data provide direct evidence for the modification of the magnetic state in LCMO layer across insulating STO below the superconducting transition temperature T_{SC} in LCMO/STO/YBCO trilayer. Magnetization in LCMO is suppressed to zero (magnetic dead layer) near the LCMO/STO interface below T_{SC} .

4.2 Growth of Perovskite manganite films

In this section, optimization of growth conditions for Perovskite manganite LSMO and LCMO and how they affect magnetic properties are described.

4.2.1 Thin films of $\text{La}_{2/3}\text{Sr}_{1/3}\text{MnO}_3$ (LSMO)

(a) Effect of oxygen partial pressure

Thin films of LSMO grown by PLD on STO(111) substrate were studied by varying the P_{O_2} employed during deposition. A pulsed KrF excimer laser (248 nm; 5 Hz)

beam was focused onto the rotating LSMO target. The substrate was maintained at 750°C, which was kept 5 cm away from the LSMO target. Prior to deposition, a base vacuum of order of 5×10^{-6} mbar was created in the deposition chamber and LSMO were deposited by varying P_{O_2} from 0 to 2.0 mbar keeping other parameters identical. The deposition was followed by in-situ post annealing at 750°C for 1 hour in 1000 mbar oxygen pressure and natural cool down to room temperature in the same environment.

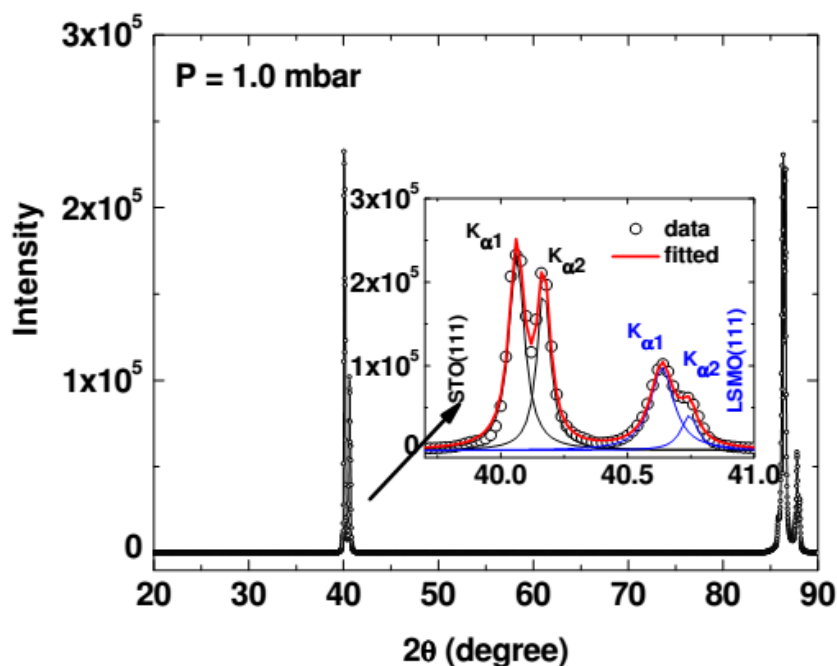


Fig. 4.1: XRD pattern on LSMO film deposited at 1.0 mbar oxygen pressure. Inset shows the enlarged view of (111) doublets of STO and LSMO fitted to lines corresponding to the X-ray source used.

XRD patterns recorded to confirm the phase formation are shown in Fig. 4.1. Observation of only (111) and (222) reflections of LSMO indicates the films are highly oriented in (111) direction. The two doublet (111) peaks around $2\theta \approx 40^\circ$ shown enlarged in the inset of Fig. 4.1 correspond to STO and LSMO respectively. The doublets are due to

$\text{Cu}_{\text{K}\alpha 1}$ (1.5406 Å) and $\text{Cu}_{\text{K}\alpha 2}$ (1.5444 Å) in the X-Ray beam. A set of doublet peaks (222) are also seen between 86°-89°.

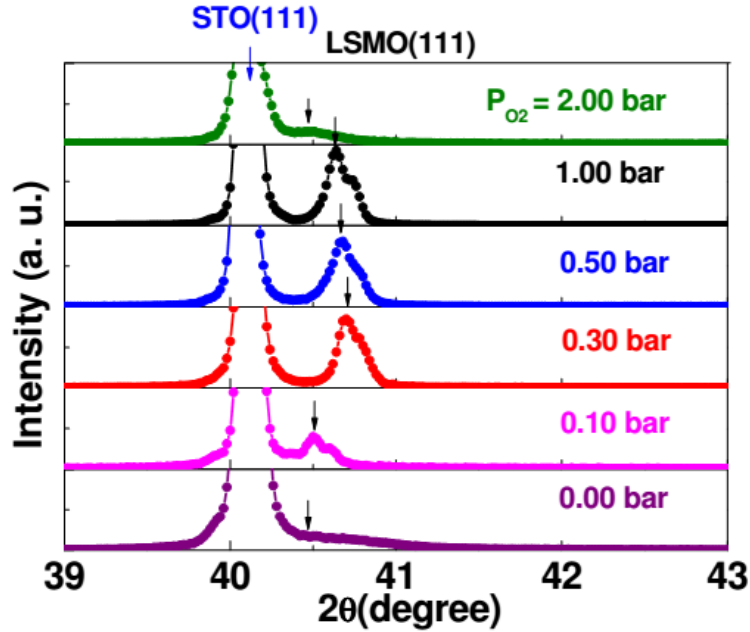


Fig 4.2: (111) peaks of STO/LSMO samples deposited under different P_{O_2} . Arrow shows the peak position.

For each of the films prepared under different P_{O_2} , XRD peaks corresponding to (111) reflections are presented in Fig 4.2. With $P_{\text{O}_2} = 0$ and 2.0 mbar, the nature of LSMO peaks indicate that the films are amorphous while the peak begins to emerge for $P_{\text{O}_2} = 0.1$ mbar. Thickness of the deposited films (750 ± 50 Å) is nearly same for $0.3 \leq P_{\text{O}_2} \leq 1$. Further, grain sizes extracted from the (111) peaks are also comparable. We will focus further part of our discussion mainly on the results obtained for samples prepared under these P_{O_2} values. The inter-planar distance d_{111} along (111) is estimated from XRD peak position to be 2.215, 2.217 and 2.218 Å for $P_{\text{O}_2} = 0.3, 0.5$ and 1.0 mbar respectively. This

amounts to a compressive strain in the out of plane direction considering the bulk value of d_{111} is about 2.24 Å. Assuming the lattice distortion is volume conserving, we calculated the tensile lattice strains in the ab plane to be 0.57%, 0.52% and 0.49% for $P_{O_2} = 0.3, 0.5$ and 1.0 mbar respectively.

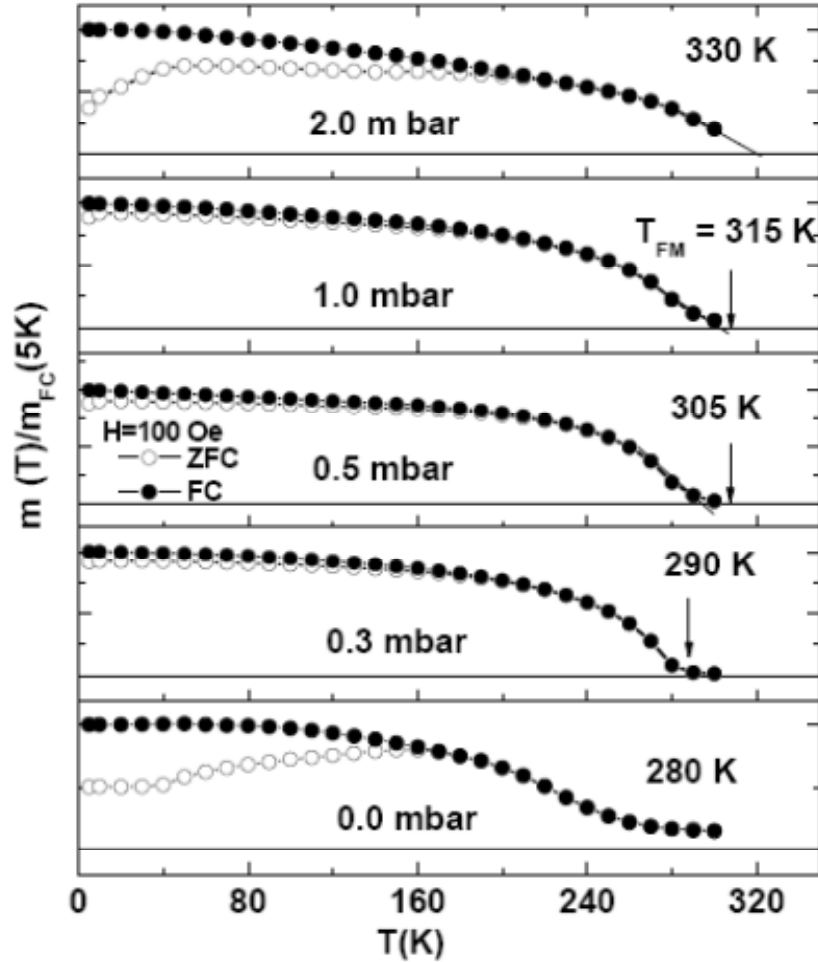


Fig. 4.3: FC and ZFC m (normalized by $m(T=5\text{ K})$) vs T data in 100 Oe field. T_{FM} is marked by an arrow.

Magnetic moment m versus temperature T data recorded under zero field cooled (ZFC) and field cooled (FC) modes in 100 Oe magnetic field applied parallel to the plane of the film is shown in Fig. 4.3. Curie temperature, T_{FM} , extracted from this data indicated

by an arrow in this figure increases from 280 to 330 K as P_{O_2} increases from 0 to 2.0 mbar. The variation in T_{FM} is consistent with the previously observed variation of T_{FM} with lattice strain for films deposited on (100) substrates [100]. Here we note that the films deposited on (100) and (111) substrates undergo tetragonal distortion, while the films deposited on (110) substrates are expected to undergo orthorhombic distortion. Following the theoretical calculations by Böttcher and Henk [101], it seems that the lattice distortions in our samples are volume conserving. We conclude from $m(T)/m(5K)$ vs T/T_{FM} plots in Fig. 4.4 that the magnetic moment increases with increasing lattice distortion, which is consistent with the results of Ref. [100].

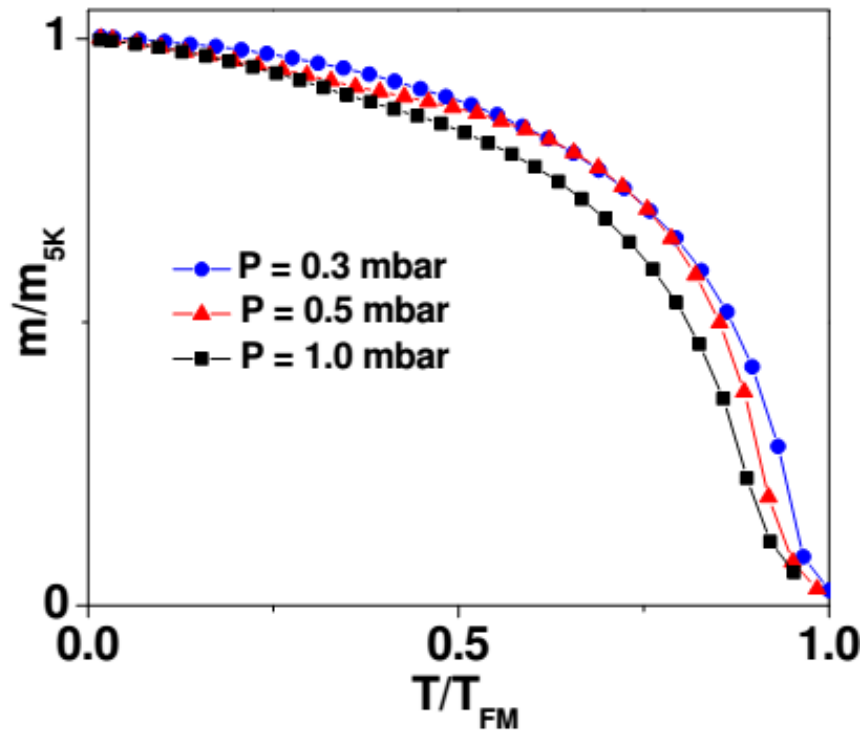


Fig.4.4: Normalized magnetization at 5K vs T/T_{FM} for different films under field cooled condition.

Fig. 4.5 shows m vs applied field H loops recorded on samples prepared under different values of P_{O_2} at $T = 5$ K. The samples with $P_{O_2} = 0.3, 0.5$ and 1.0 mbar show square type hysteresis loops with a well defined coercive field H_C , which increases with increasing P_{O_2} . There are two possible factors contributing to the change in H_C . Firstly, d_{111} is minimum for $P_{O_2} = 0.3$ mbar. This essentially increases the magneto-crystalline anisotropy for field applied parallel to the plane of the film, which should cause H_C to be larger. However, the observed behavior is contrary. As the grain sizes are nearly same in all the three films, this can perhaps be explained by the fact that T_{FM} decreases with lattice strain and at a given temperature, H_C is expected to be lower for smaller T_{FM} .

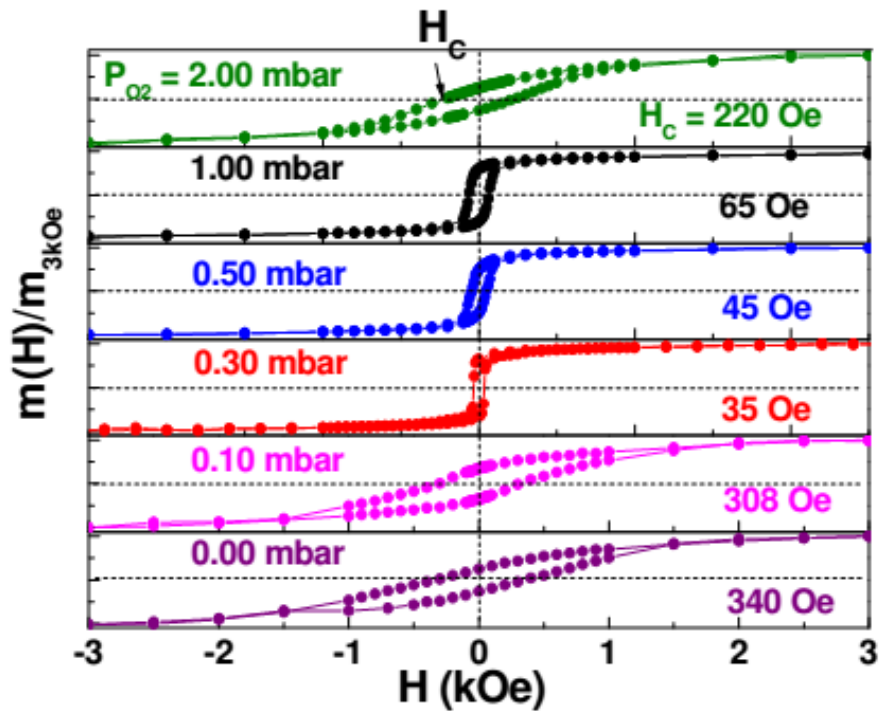


Fig. 4.5: $m - H$ loops measured at 5K for different values of P_{O_2} .

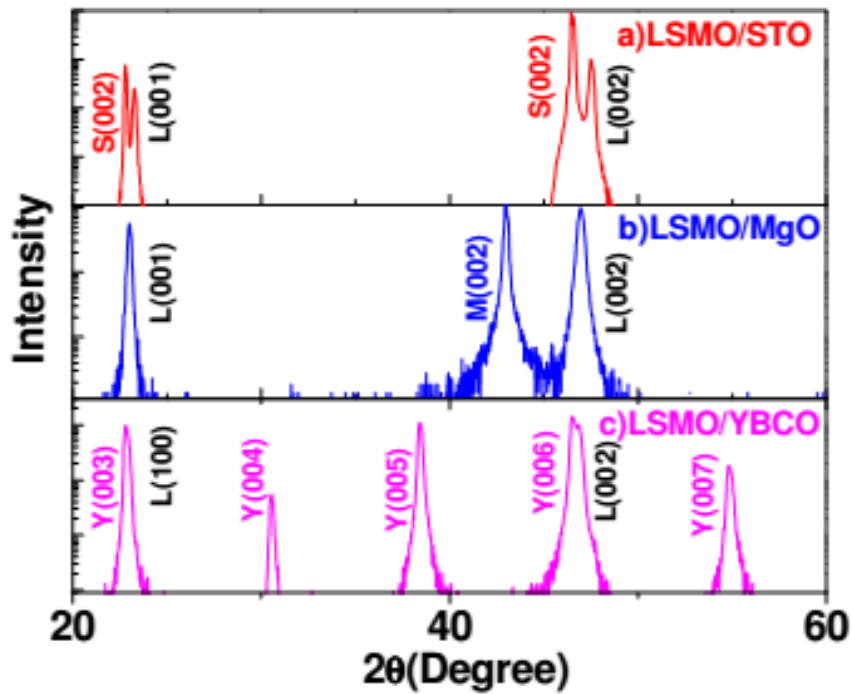


Fig. 4.6: XRD pattern of 500Å LSMO thin films on a) STO(100), b) MgO(100) and c) YBCO substrates.

(b) LSMO films on different substrates

LSMO films of nominal thickness 500 Å were deposited on STO (100), MgO (100) and YBCO (001) substrates (*c*- oriented YBCO film (1000 Å) on STO (100) substrate is here called YBCO (001) substrate) held at 750°C under $P_{O_2} = 0.5$ mbar using PLD. The laser fluence and frequency used were 3.5 J/cm² and 5 Hz respectively. XRD patterns of the grown films are shown in Fig 4.6. It is evident that the films grown on all the three substrates are preferentially oriented with (n00) planes parallel to the substrate plane.

The position (broadening) of LSMO (200) peak on STO, MgO and YBCO substrates are 47.52°(0.23°), 46.92° (0.34°) and 46.82° (0.30°) respectively. It is known that the shift in peak position gives the uniform strain whereas broadening provides the

information about non-uniform strain. The theoretical value of uniform strain (ε_{th}) of LSMO film on different substrates is equal to that of lattice mismatch, which can be estimated using the following equation:

$$\varepsilon_{th} \% = \frac{(a_{substrate} - a_{LSMO})}{a_{substrate}} \times 100$$

The value of ε_{th} obtained for LSMO on STO, MgO and YBCO substrates are 0.6%, 8% and -2% respectively. Since LSMO has a cubic crystal structure, value of c-lattice parameter can be calculated using

$$c_{LSMO} = \frac{n\lambda(h^2 + k^2 + l^2)^{0.5}}{2\sin\theta_{hkl}}$$

The obtained value of c-lattice parameter of LSMO on STO, MgO and YBCO substrates were found to be 3.8267, 3.8728, and 3.8806 Å respectively. In the case of uniform strain in a cubic unit cell, the unit cell volume is expected to remain unchanged. The unit cell volume of LSMO is 59.23 Å³ (lattice parameter a = 3.876 Å for bulk LSMO). Thus using the c-lattice parameter, we have estimated the lattice strains in the *ab* plane to be 0.64%, 0.04% and -0.06% for STO, MgO and YBCO substrates respectively. The positive (negative) sign indicates tensile strain on film deposited on STO and MgO (YBCO) substrates. In the case of STO the theoretical strain is equal to the experimentally measured strain, indicating absence of non-uniform strain, whereas in the case of MgO and

YBCO substrates, the non-uniform strain is predominant. The value of non-uniform strain can be estimated from the broadening of the XRD peak using the equation:

$$\left(\beta_{Exp}^2 - \beta_{In}^2 - \beta_{Grain}^2\right)^{0.5} = 4. \varepsilon. \tan\theta$$

The values of non-uniform strain calculated for LSMO on MgO and YBCO substrates are 0.00252 and 0.00194 respectively.

In order to investigate the effect of strain on magnetic properties of LSMO films, m - T measurements of LSMO films grown on STO, MgO and YBCO were carried out under ZFC and FC conditions in an in-plane field of 100 Oe as shown in Fig 4.7.

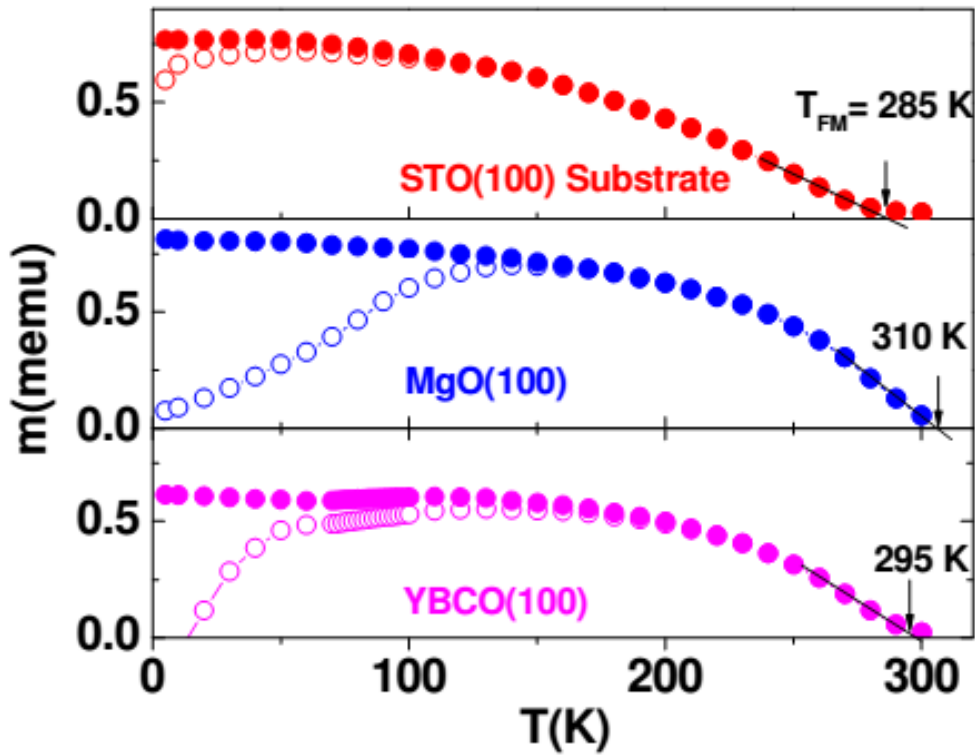


Fig. 4.7: ZFC and FC m vs T in a field of 100 Oe. T_{FM} is marked by arrow.

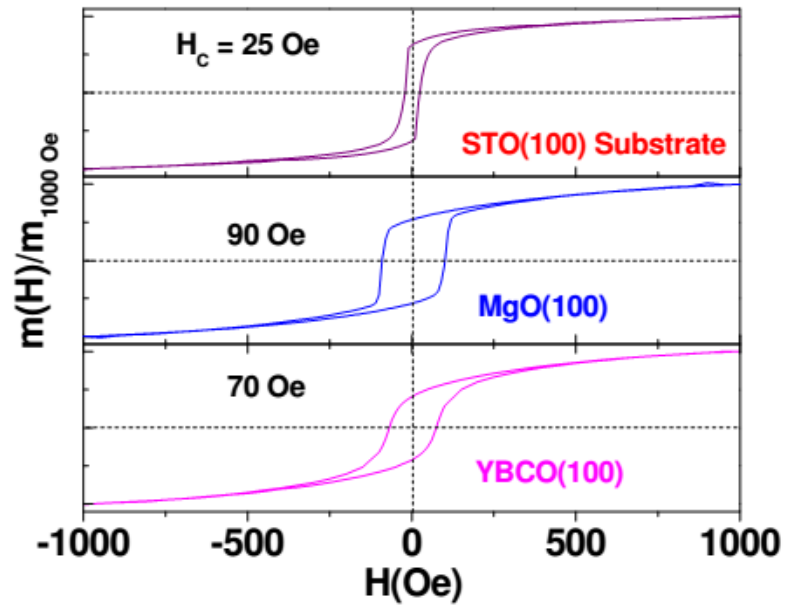


Fig. 4.8: $m - H$ loops measured at 100 K for different LSMO films on different substrates.

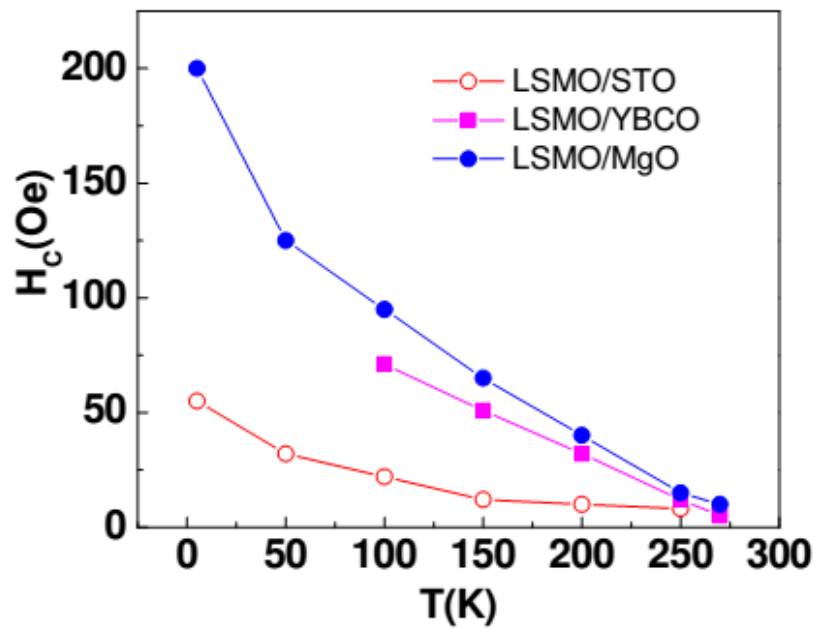


Fig. 4.9: H_c vs T in LSMO films deposited on different substrates.

The results in Fig. 4.7 reveal that (i) T_{FM} increases with increasing strain from 285 K in the film deposited on STO and highest (310 K) for that on MgO; and (ii) Irreversibility between ZFC and FC branches increases with increasing strain. The m - H loops for the three films measured at 100 K are shown in Fig. 4.8. Coercive field H_C also depends on the amount of strain i.e. lowest (25 Oe) for STO and highest (90 Oe) for MgO substrates. H_C vs temperature extracted from m - H loops measured at different temperatures is plotted in Fig. 4.9. H_C of LSMO on MgO being 3-4 times higher than that on STO between 5 and 270 K clearly indicates that strains in LSMO films strongly influence the magnetic properties.

(c) Effect of film thickness

In order to establish the effect of strain on the magnetic properties, LSMO films of varying thickness (100-1000 Å) were deposited on STO and MgO substrates.

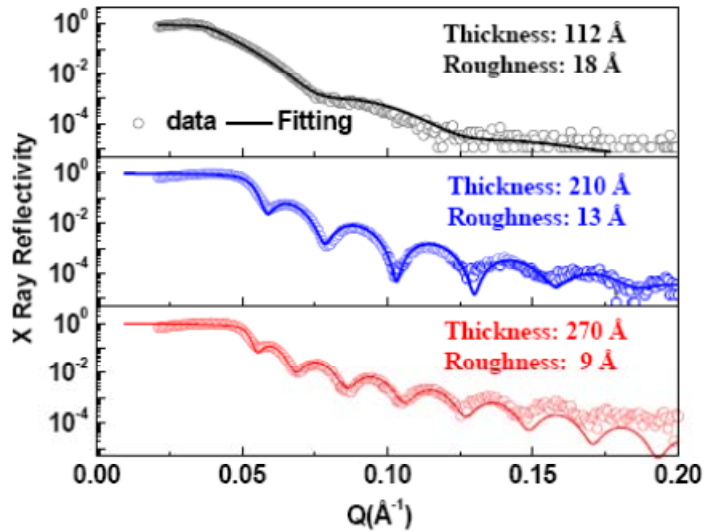


Fig.4.10: XRR patterns of LSMO films with different thickness on MgO (100) substrates.

Thickness of films is varied by varying the deposition time. Further XRR measurements are carried out to confirm the thickness of LSMO film as shown in Fig 4.10. Thickness and roughness of the films were estimated from best fit to XRR data. It shows that the roughness of films decreases with increasing film thickness, which can be attributed to the relaxation in the non-uniform strain.

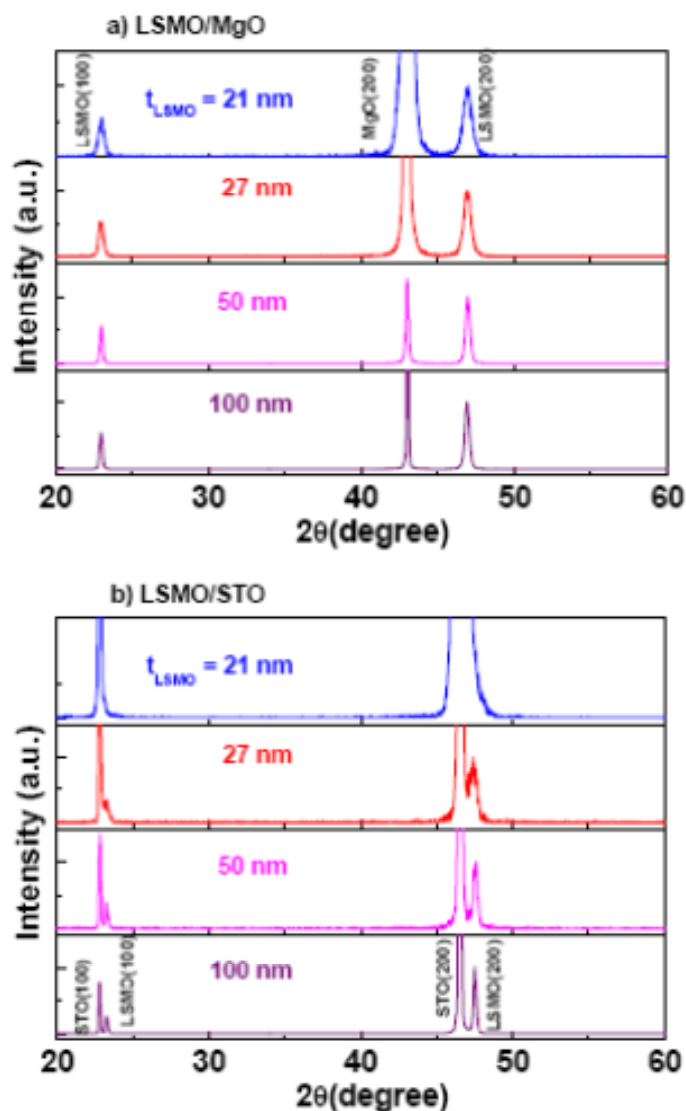


Fig.4.11: XRD pattern of LSMO films with different thickness on a) MgO(100) and b) STO(100) substrates.

Typical XRD patterns of LSMO films grown on MgO and STO substrates are shown in Fig. 4.11(a) and (b). It is noted that the full width at half maxima (FWHM) of peaks decreases with increasing film thickness. This effect is more pronounced in the case of films deposited on MgO. Non uniform strain calculated by broadening and plotted as a function of thickness is depicted in Fig 4.12. It is evident that the strain exponentially decreases with increasing thickness, which is expected as the strain relaxes as the thickness increases.

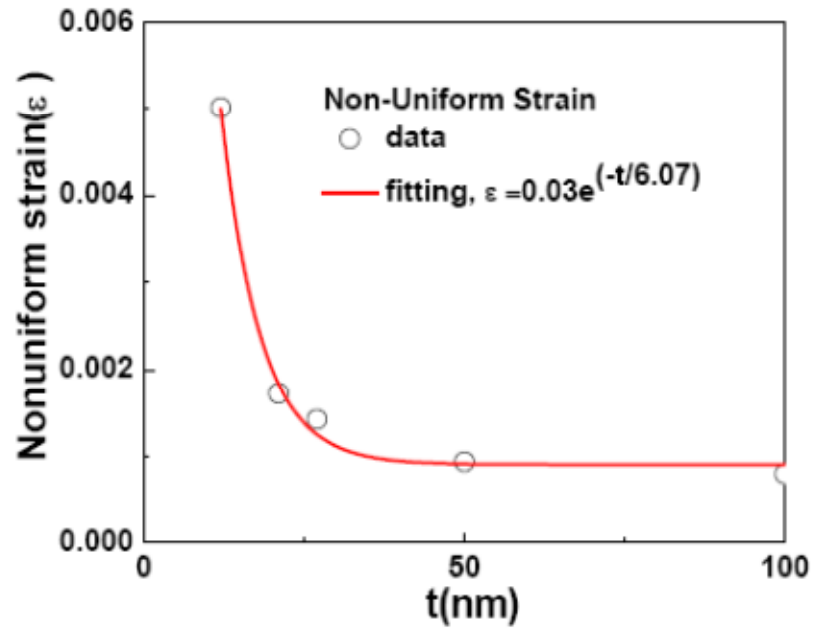


Fig.4.12: Non uniform strain with LSMO thickness on MgO(100) substrates.

ZFC and FC m vs T data recorded for LSMO films of different thickness deposited on MgO substrate in 100 Oe field applied parallel to the film plane are shown in Fig. 4.13. For LSMO films of thickness from 21 nm to 100 nm, the irreversibility in ZFC and FC decreases with increasing thickness. The m - H loops of LSMO films of different thicknesses grown on MgO and STO substrates are shown in Fig. 4.13. H_C values extracted

are plotted as a function of film thickness in Fig. 4.14, which decrease monotonically with thickness in the case of films deposited on MgO whereas in the case of films deposited on STO it is independent of thickness, indicating strain quickly relaxes in the case of STO. On the other hand, in case of MgO, due to larger lattice mismatch the relaxation of stain can occur only at very high film thicknesses.

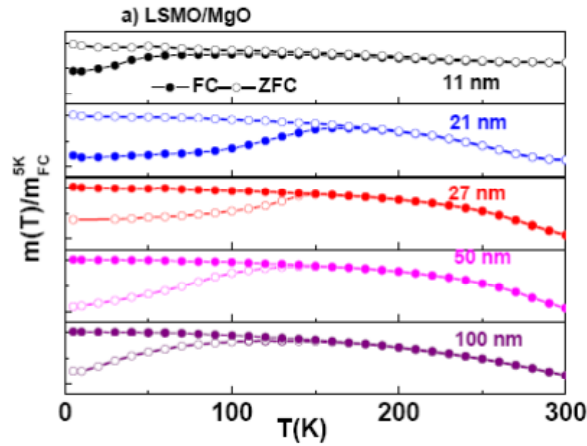


Fig.4.13: m vs T for LSMO film of different thickness on MgO Substrate.

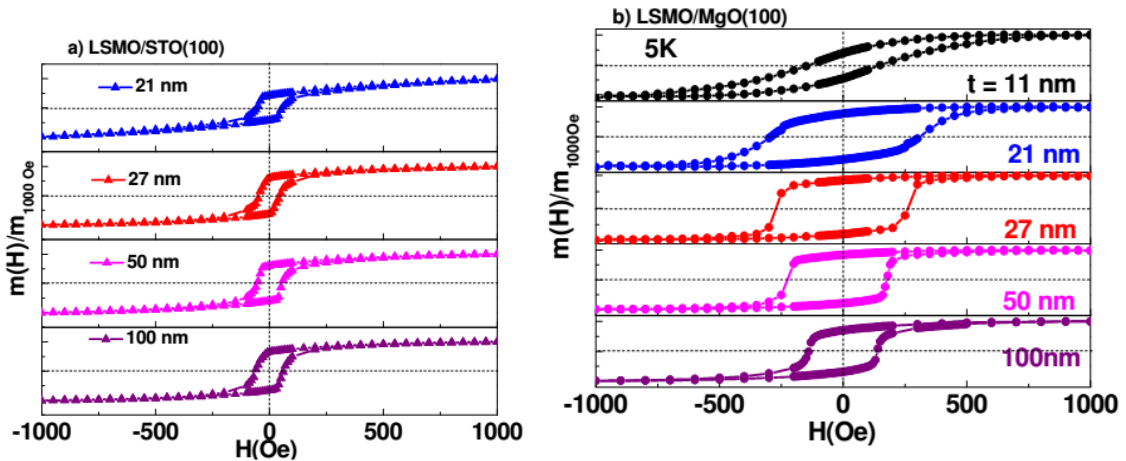


Fig. 4.14: $m - H$ loops measured at 5K for LSMO film with different thicknesses on a) STO(100) and b) MgO(100) substrates.

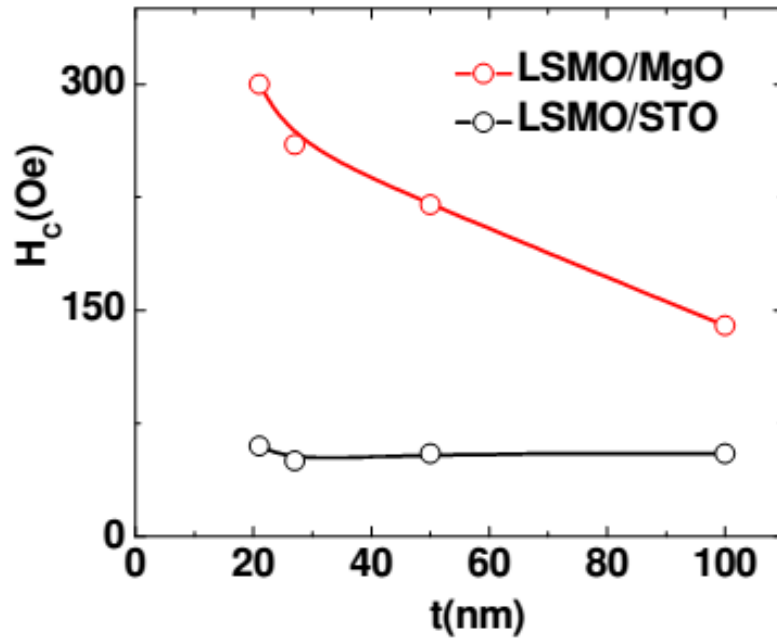


Fig.4.15: Variation in H_c with LSMO film thickness deposited on STO(100) and MgO(100) substrates.

4.2.2 Thin films of $\text{La}_{2/3}\text{Ca}_{1/3}\text{MnO}_3$ (LCMO)

Thin films of LCMO were grown on STO (100) and MgO (100) substrates under identical conditions, i.e. substrate temperature $\sim 750^\circ\text{C}$, oxygen pressure ~ 0.5 mbar, laser fluence (per pulse) of 3.5 J/cm^2 and 5 Hz frequency. The nominal thickness of the films was 200 \AA . Typical XRR plot of the LCMO film is shown in Fig. 4.16. The data fit yielded the film thickness of $\sim 240 \text{ \AA}$, and roughness $\sim 10 \text{ \AA}$.

Magnetic moment (m) versus temperature (T) data recorded in zero field cooled (ZFC) and field cooled (FC) modes in 100 Oe magnetic field applied parallel to the plane of the film is shown in Fig. 4.17. The ferromagnetic transition, T_{FM} is observed at 145 K. It

shows similar behavior, which is observed in case of LSMO. LCMO on MgO have more irreversibility in ZFC and FC, which reveals the hard ferromagnetic nature where as LSMO/STO shows soft nature

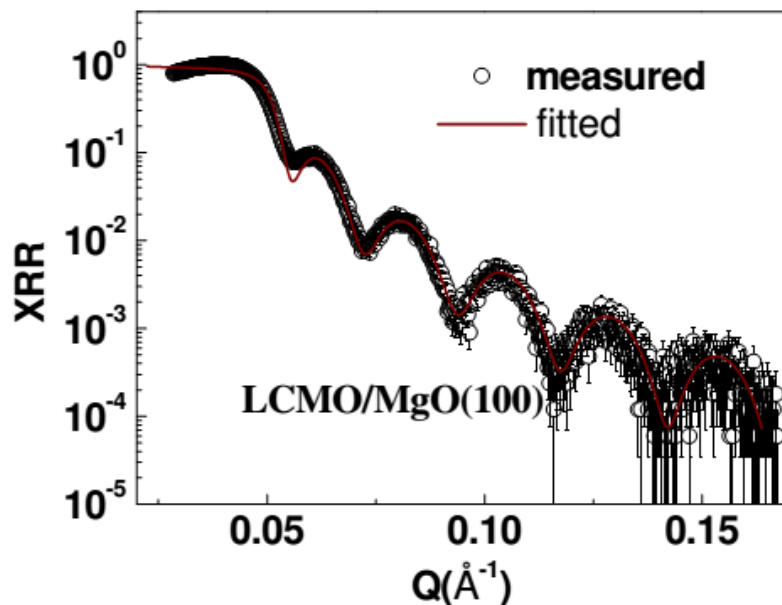


Fig.4.16: XRR pattern of LCMO film with on MgO (100) substrates.

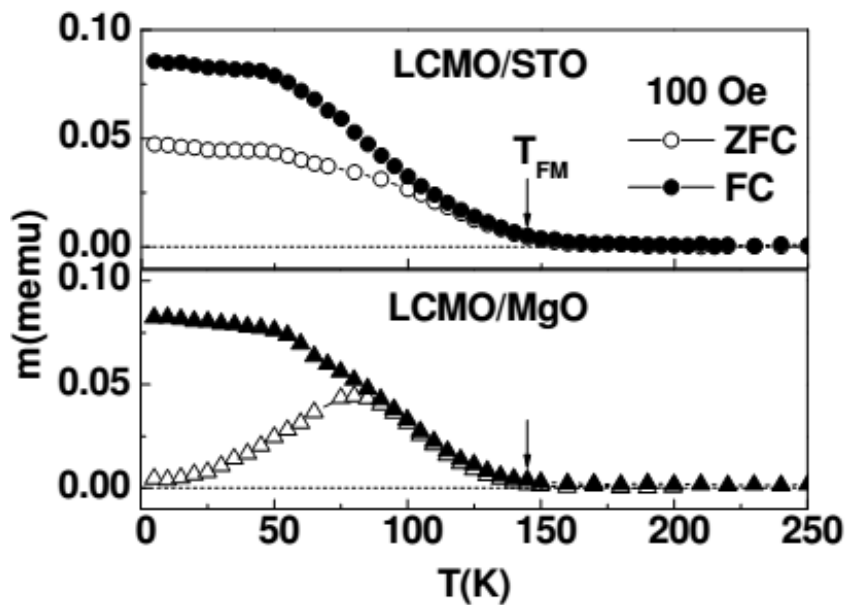


Fig.4.17: ZFC and FC m vs T of LCMO films on STO (100) and MgO (100) substrates.

The results of XRR and magnetization data show that the quality of LCMO films is same as that of LSMO, if grown under identical conditions.

4.3 Growth of $\text{YBa}_2\text{Cu}_3\text{O}_{7-\delta}$ (YBCO) films:

YBCO films of nominal thickness 150 Å were deposited on STO (100) and MgO (100) substrates held at 750°C under $P_{\text{O}_2} = 0.5$ mbar, laser fluence per pulse of 3.5 J/cm² and 5 Hz frequency. XRD patterns are recorded for both films as shown in Fig. 4.18.

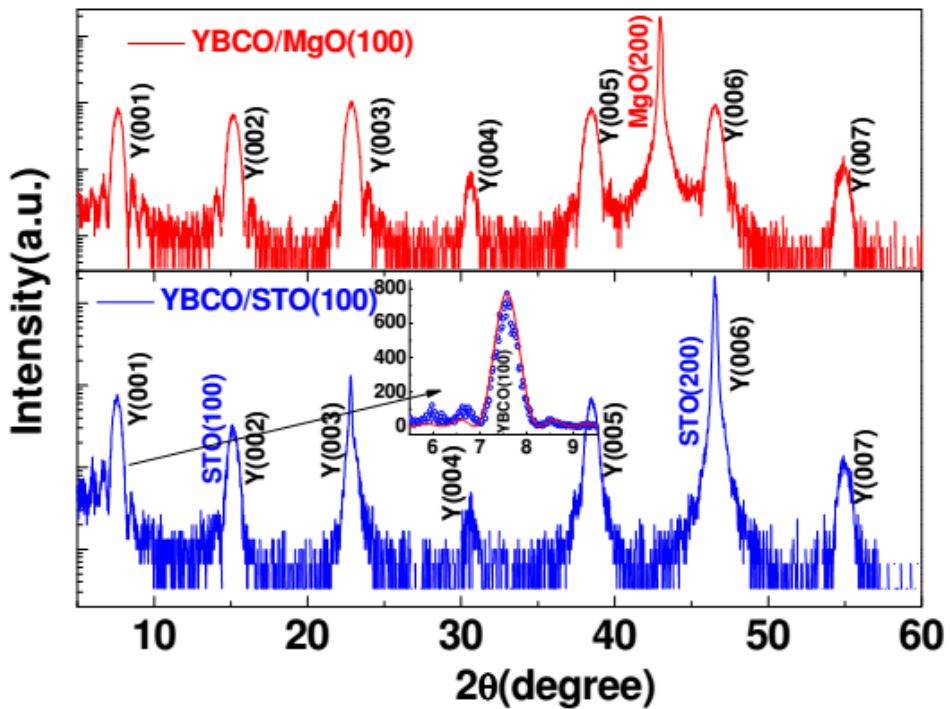


Fig.4.18: XRD pattern of YBCO films on MgO (100) and STO (100) substrates.

In XRD patterns, only (00n) YBCO peaks are observed with side oscillation due to thickness fringes. YBCO on MgO peaks have higher broadening than YBCO on STO. This may be lattice mismatch of YBCO with MgO is higher which may produce strain in YBCO film. The thickness of YBCO, 128Å was estimated by fitting of thickness fringes as shown in inset of lower panel of Fig. 4.18. Which was further confirmed by XRR measurement as shown in 4.19 is same.

A zero field cooled measurement in presence of applied magnetic field (20 Oe) parallel to substrate is shown in Fig 4.20. Which shows the T_{SC} for YBCO thin film on STO is 78 K where is no superconductivity was observed in YBCO on MgO.

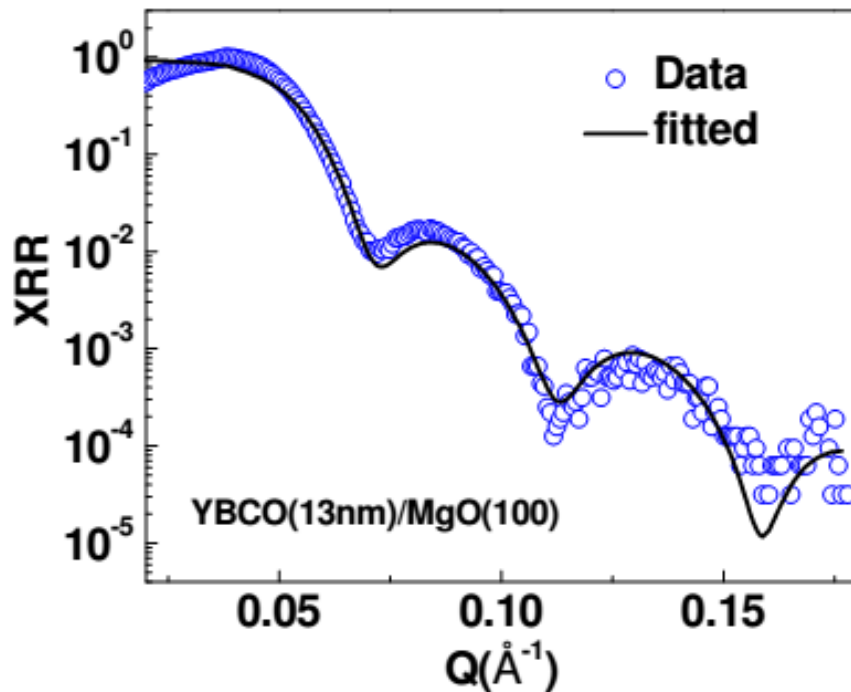


Fig.4.19: XRR pattern of LCMO film with on MgO (100) substrates.

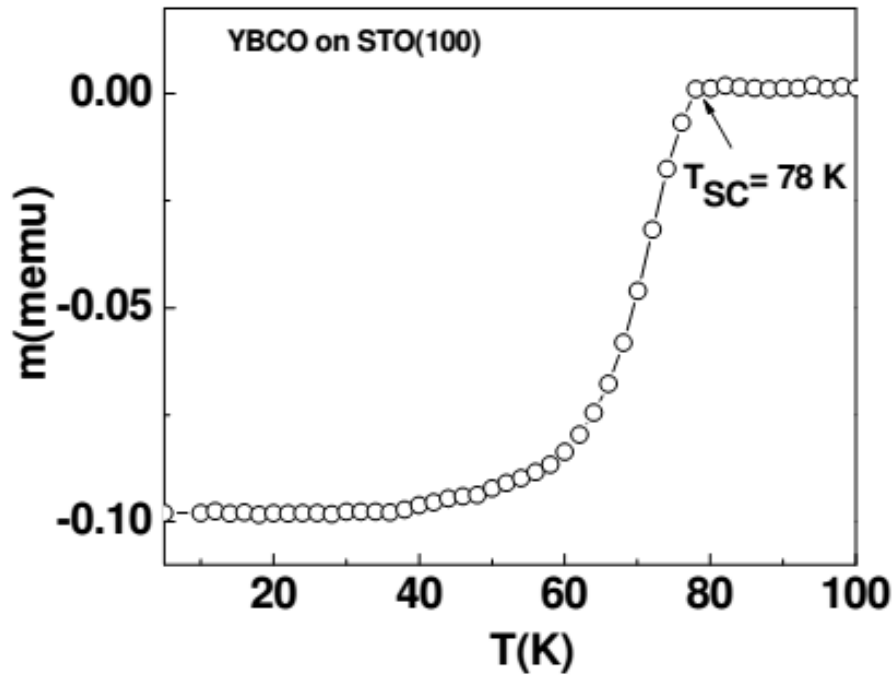


Fig.4.20: Superconducting transition on YBCO film on STO (100) substrates.

4.4 Growth and characterization of LCMO/STO/YBCO heterostructures

In order to optimize the growth conditions for LCMO/STO/YBCO heterostructures on STO (100) substrates by pulsed laser deposition, we have first grown the STO (25 Å)/YBCO (200 Å) bilayers on STO (100) substrates. The XRD pattern of the bilayer of STO/YBCO is presented in Fig. 4.21. Presence of only (00n) reflections shows that YBCO film is highly c-oriented. Typical XRR plots for the STO/YBCO bilayer are shown Fig 4.22. The thickness of the YBCO and STO layers are found to be 185 and 24 Å, respectively. Moreover, the STO/YBCO interface roughness was found to be 12 Å, indicating very smooth interface.

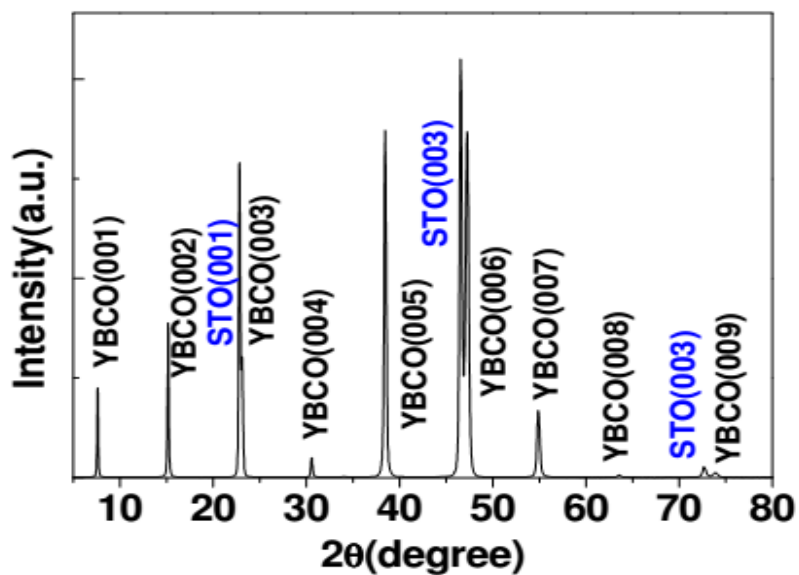


Fig. 4.21: X-ray diffraction data from STO/YBCO bilayer on STO (100) substrate.

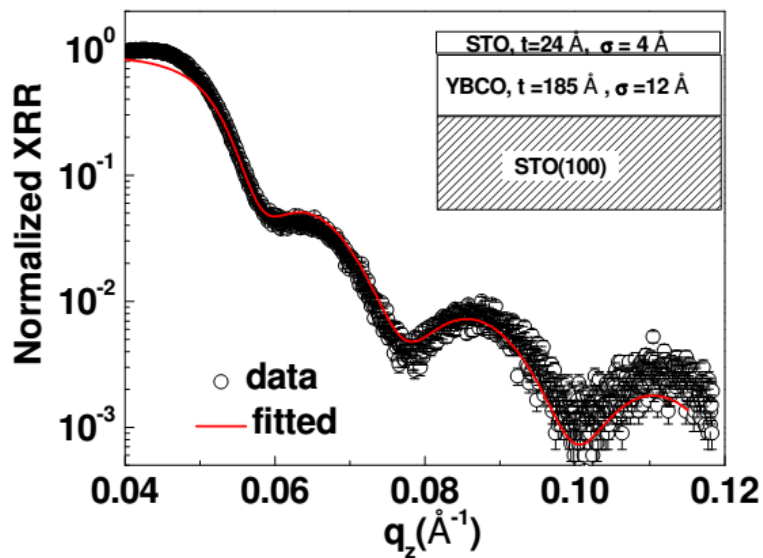


Fig. 4.22: X-ray reflectivity (XRR) pattern from STO/YBCO heterostructures. Inset show the corresponding thickness and roughness of each layer which gave best fit to XRR data.

Growth parameters used for STO (25 Å)/YBCO (200 Å) bilayers were also used for the growth of LCMO (300 Å)/ STO (25 Å)/YBCO (300 Å) and LCMO (200 Å)/STO (50

Å)/ YBCO (200 Å) trilayers on STO (100) substrate. LCMO/STO/YBCO heterostructures were characterized by XRD to confirm the crystalline nature and XRR measurement was carried out to find layer thickness and interface roughness.

4.3.1 X-Ray Diffraction

The degree of crystalline of the heterostructures was evaluated by X-ray Diffraction (XRD) measurements. Typical XRD pattern of the trilayer for LCMO (300 Å)/ STO (25 Å)/YBCO (300 Å) is presented in Fig. 4.23. YBCO layer preferentially grows along the c-axis.

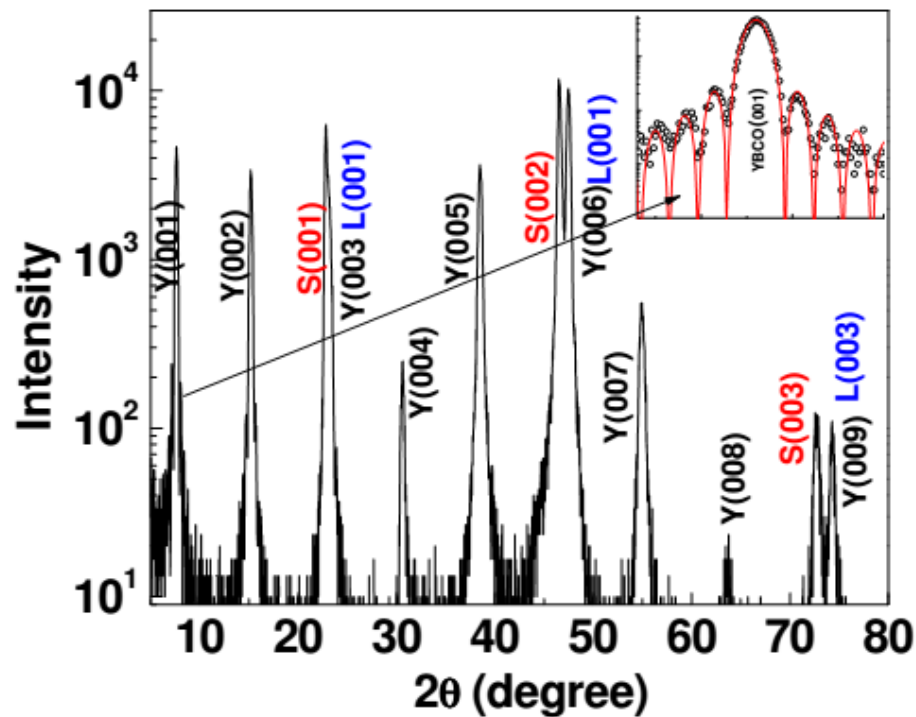


Fig. 4.23: X-ray diffraction data from LCMO/STO/YBCO trilayer on STO (100) substrate.

The inset shows the magnified version of the (001) peak of the YBCO, which has the thickness fringes. YBCO (001) peak was fitted using following equation to estimate the thickness of YBCO in trilayer:

$$I \propto \frac{\text{Sin}^2(NQd)}{\text{Sin}^2(Qd)}$$

Where, N is the number of lattice planes, d is lattice spacing (here for the first peak of YBCO, d is equal to c-lattice parameter, and $Q = \frac{4\pi}{\lambda} \sin \theta$, $\lambda =$ wave length Cu K_{α}). The fit yields film thickness of 28 nm and Lattice parameter $c = 11.67 \text{ \AA}$ corresponding to an oxygen content of 6.7 in YBCO [99, 100] indicating YBCO is in under doped regime.

Table 4.1: parameters obtained from XRR measurements.

LCMO (300 Å)/STO (25 Å)/YBCO (300 Å)				LCMO (200 Å)/STO (50 Å)/YBCO (200 Å)		
heterostructure				heterostructure		
layer	Thickness (Å)	Electron SLD (10^{-5} \AA^{-2})	Roughness (Å)	Thickness (Å)	Electron SLD (10^{-5} \AA^{-2})	Roughness s (Å)
LCMO	320±15	4.97±0.06	13±3	187±12	4.88±0.07	10±3
STO	23±2	4.30±0.05	4±1	50±3	4.25±0.05	5±1
YBCO	285±15	4.76±0.04	12±4	185±11	4.74±0.05	14±4

4.3.2 X-Ray Reflectivity

In order to confirm the thickness of the layers and estimate the interface roughness, the XRR patterns were recorded for LCMO (300 Å)/STO (25 Å)/YBCO (300 Å) and LCMO (200 Å)/STO (50 Å)/YBCO (200 Å) trilayers are shown in Fig 4.24. The inset of Fig 4.24 shows the electron scattering length density (ESLD) profile which gave best fit to XRR data. The obtained parameters of the analyses of the XRR data are presented in Table 4.1.

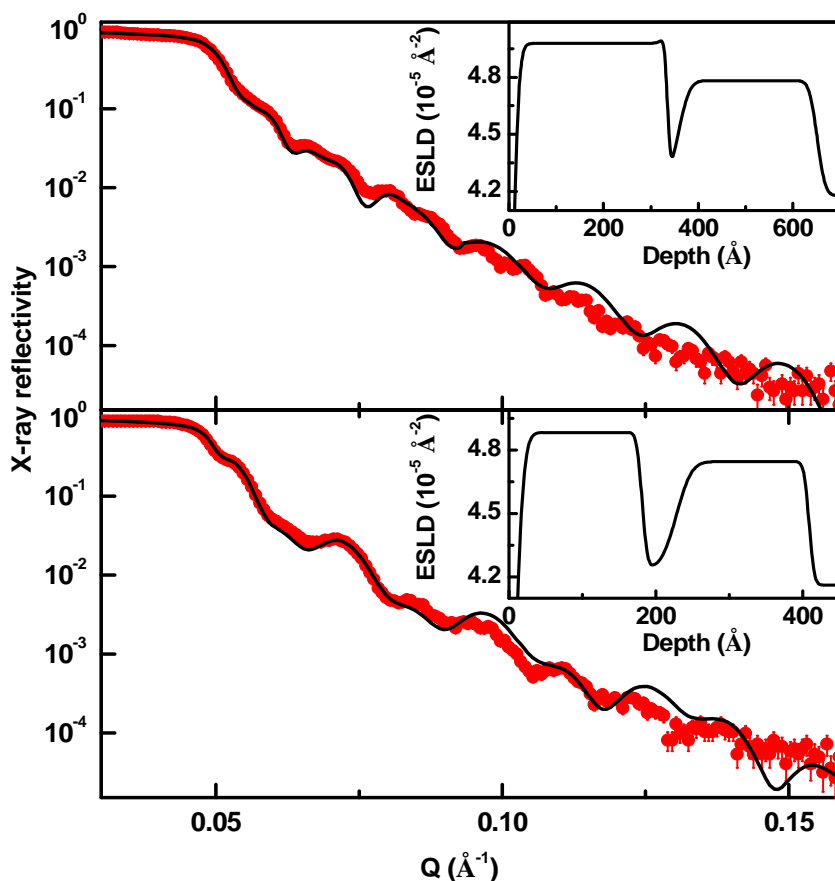


Fig. 4.24: X-ray reflectivity (XRR) pattern from two heterostructures LCMO (300 Å)/STO (25 Å)/YBCO (300 Å) and LCMO (200 Å)/STO (50 Å)/YBCO (200 Å).

4.3.3 Magnetic Properties

Temperature dependent DC magnetization data measured on LCMO (300 Å)/STO (25 Å)/YBCO (300 Å) under FC mode is shown in Fig. 4.25. The ferromagnetic transition is observed at temperature $T_{\text{FM}} = 130$ K, which is slightly lower (150 K) than the individual LCMO layer. Superconducting transition $T_{\text{SC}} = 60$ K is inferred from ZFC data shown in the inset of Fig. 5.5. The lower T_{SC} of the trilayer is attributed to proximity effect and/or low oxygen content, as revealed from XRD data. From the oxygen content estimated earlier, T_{SC} reduction is expected to be 78 K. This implies that there is a strong magnetic proximity effect.

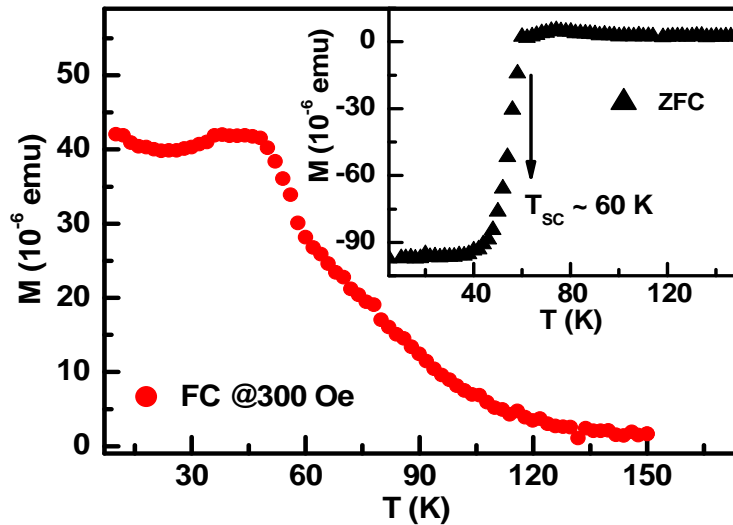


Fig. 4.25: FC Magnetization of LCMO (300 Å)/STO (25 Å)/YBCO (300 Å) trilayer in 300 Oe field showing the FM transition at around 130 K. Inset show ZFC showing $T_{\text{SC}} \sim 60$ K.

4.3. Investigation of magnetic proximity effect in LCMO/STO/YBCO heterostructures using PNR

In order to study the magnetic proximity effect, PNR measurements were carried out as a function of temperature under FC condition. PNR data with neutron spin polarized in the field direction (R^+) and that opposite to the field (R^-) recorded at 300 and 10 K are shown in Fig. 4.26 (a). The solid line in Fig. 4.26(a) is a fit to experimental data. The difference between spin dependent neutron reflectivity ($R^+ - R^-$), is plotted in Fig. 4.26 (b) at 300 K where R^+ and R^- are the same indicating zero net magnetization.

In order to extract the information from PNR measurements, we first optimized the nuclear scattering length density (NSLD) profile from PNR data at 300 K by constraining layer thicknesses and interface roughness to be within 95% confidence limit [102], i.e., $2\text{-}\sigma$ error, established from the analysis of XRR data. The reflectivity was calculated using the dynamical formalism of Parratt [77] and parameters of the model were adjusted to minimize the value of weighted measure of goodness of fit χ [101]. The NSLD was fixed and then only magnetization depth profile $M(z)$ was optimized to the PNR data taken at 10 K. Fig. 4.26 (c) and (d) correspond to NSLD and $M(z)$ depth profiles at 300 K and 10 K respectively which fitted the PNR data well for given temperatures (Fig. 4.26(a) and 5.6(b)). The interface roughness for air/LCMO (surface), LCMO/STO (LCMO on STO), STO/YBCO (STO on YBCO) and YBCO/substrate interface were obtained from XRR and PNR to be $13 \pm 3 \text{ \AA}$, $4 \pm 1 \text{ \AA}$, $12 \pm 4 \text{ \AA}$ and $6 \pm 2 \text{ \AA}$ respectively. Thus LCMO/STO interface roughness ($\sim 4 \text{ \AA}$) was about one third of the other interfaces grown by PLD.

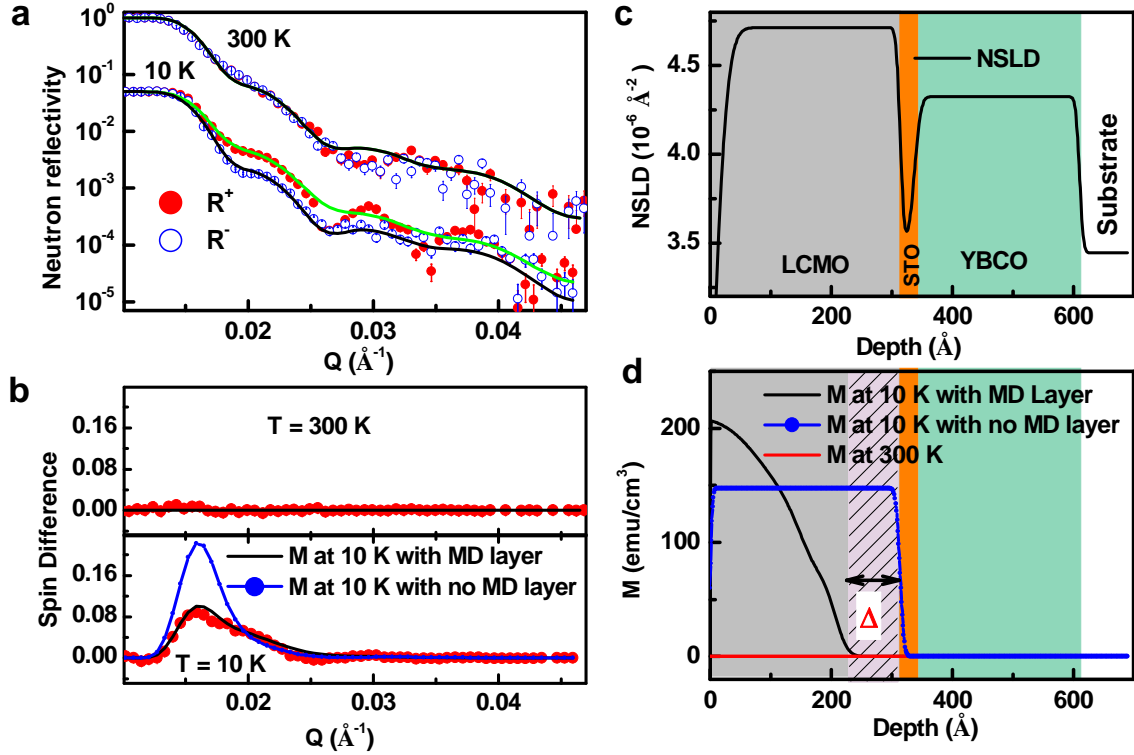


Fig. 4.26: (a) Polarized neutron reflectivity (PNR) measurements and their modeling. a, PNR (spin up, R^+ and spin down, R^-) data from the LCMO (300 \AA)/STO (25 \AA)/YBCO (300 \AA) trilayer at 300 K and 10 K. Reflectivity data at different temperature are shifted by a factor of 20 for the sake of clarity. (b) Spin difference ($R^+ - R^-$) data at 300 K (upper panel) and 10 K (lower panel). (c) Nuclear scattering length density (SLD) depth profile extracted from fitting PNR data at 300 K as shown in a, b. (d) Magnetization (M) depth profile corresponding to PNR data shown in (a) and (b). Two magnetization models, with and without magnetic dead (MD) layer at LCMO/STO interface, at 10 K are depicted in d and the corresponding fits to PNR data are shown in b (lower panel).

The important finding in this study is the magnetization depth profile of the sample at 10 K (Fig. 4.26) measured well below T_{SC} . A detailed comparison of different models of magnetization depth profile and corresponding fits to measured PNR data at 10 K is shown in Fig. 4.27. We used different models for the magnetization depth profile by considering

uniform and non uniform magnetization across LCMO layer. A comparison of three models which gave better fit (with smaller χ^2) to PNR data at 10 K are shown in Fig. 4.27(b). These three models are (a) Where the magnetization is homogeneous throughout LCMO layer, (b) magnetization is suppressed (or formation of magnetic dead layer) at LCMO/STO interface but uniform magnetization in the rest of LCMO layer and (c) formation of magnetic dead layer at LCMO/STO interface and non uniform magnetization in the rest of LCMO layer. Fig 4.27 clearly depicts that model (c) best fit (with smallest χ^2) the PNR data at 10 K, suggesting modulation in magnetization depth profile LCMO layer.

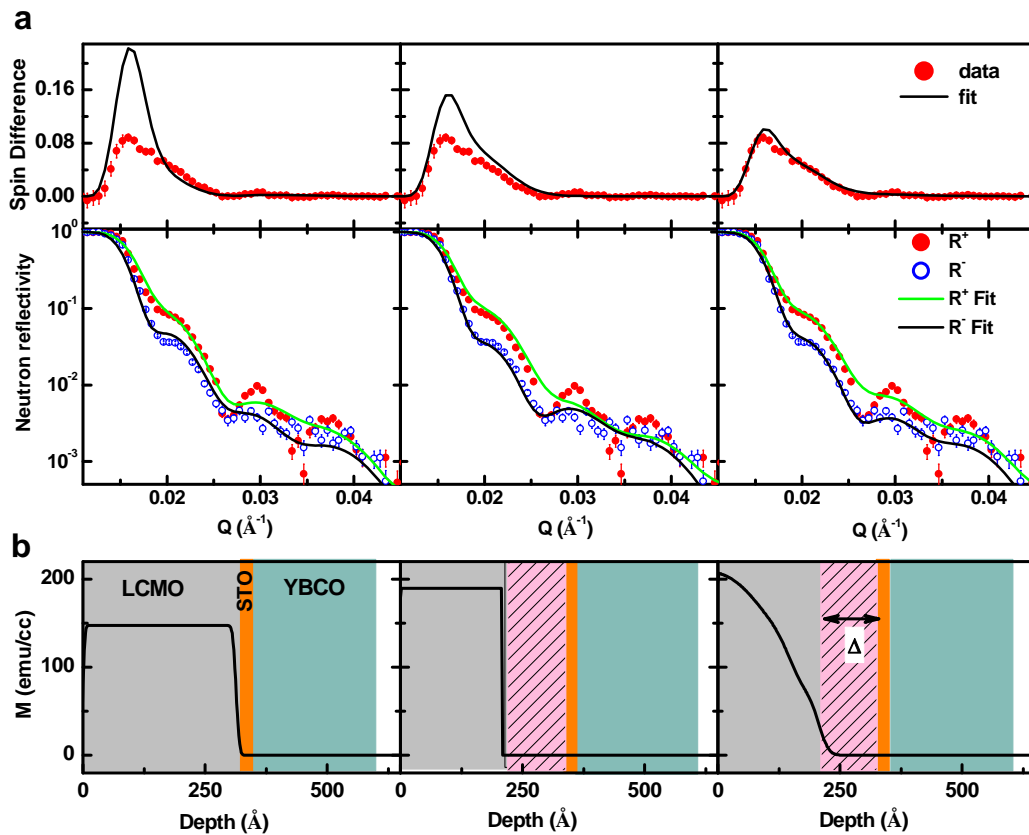


Fig. 4.27: **a**, PNR (spin up, R^+ and spin down, R^-) data from the LCMO (300 \AA)/STO (25 \AA)/YBCO (300 \AA) sample at 10 K. upper panel show the spin difference ($R^+ - R^-$) data at 10 K. **b**, shows the corresponding magnetization depth profiles which fitted PNR data at 10 K.

A comparison of two models, with and without magnetic dead layer at LCMO/STO interface, is shown in Fig. 4.27. Assuming uniform magnetization over the whole LCMO layer didn't fit PNR data well at 10 K as shown in Fig. 4.26 (a) and (b). The fit to PNR data at 10 K and solid curve in the lower panel of Fig. 4.27 with minimum χ^2 was obtained with magnetic depth profile shown as a solid line in Fig. 4.27(b), suggesting a magnetic dead layer (graded area in Fig. 4.27 (b) at LCMO/STO interface of thickness, $\delta \sim 100 \text{ \AA}$ and a non-uniform magnetization in the rest of LCMO layer, which increases to a maximum value $\sim 205 \text{ emu/cc}$ near the surface.

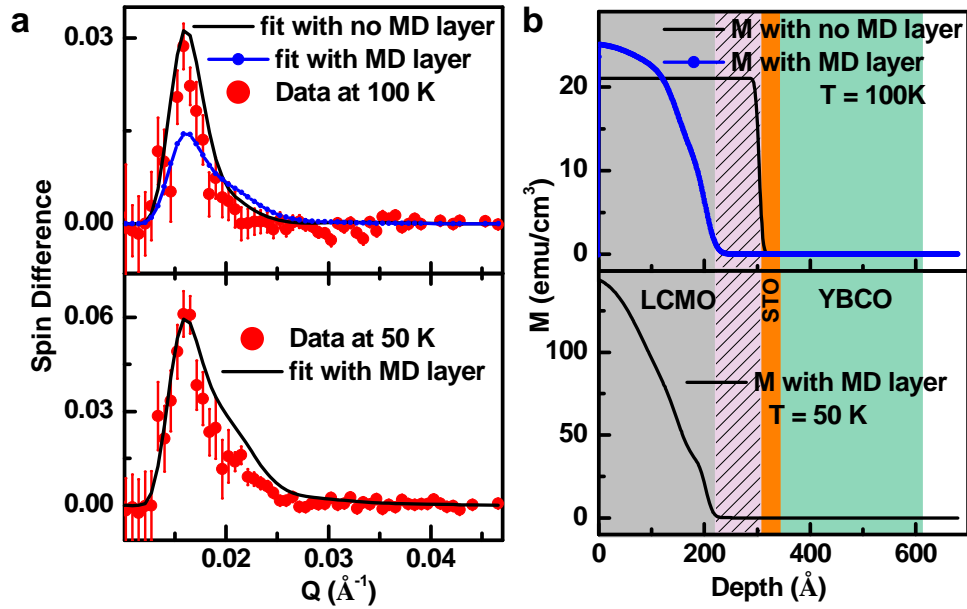


Fig. 4.28: Polarized neutron reflectivity (PNR) measurements and their modeling across superconducting transition temperature. (a) Spin difference ($R^+ - R^-$) data the LCMO (300 Å)/STO (25 Å)/YBCO (300 Å) sample at 100 K (upper panel) and 50 K (lower panel). (b) Magnetization (M) depth profile at 100 K (upper panel) and 50 K (lower panel) corresponding to spin difference data shown in a. Two magnetization models at 100 K are depicted in the upper panel of (b) and the corresponding fits to PNR data are shown in upper panel of (a).

In order to confirm the effect of superconductivity on magnetic modulation in sample A, we carried out PNR measurements at 100 K ($> T_{SC}$) and 50 K ($< T_{SC}$). Upper and lower panels of Fig. 4.28(a) show PNR (Spin difference) data at 100 K and 50 K respectively. A comparison of different magnetization models to fit PNR data at 100 K is shown in the upper panel of Fig. 4.28(b) which clearly suggests a small but uniform magnetization (solid curve) for whole LCMO layer. The other model with magnetic dead layer at LCMO/STO interface is not consistent with the PNR data at 100 K. On the other hand the PNR data at 50 K (lower panel of Fig. 4.28(a) and (b)) is consistent with the magnetization model profile used at 10 K. These results clearly suggest that the magnetic dead layer emerges below the superconducting transition.

We recall the observation of suppressed magnetization at the LCMO/YBCO interface over a thickness of 2-3 unit cells in LCMO as a result of charge transfer across the interface [44]. However, magnetization suppression in our case occurs over much larger length scales upto several nanometers, which is comparable to long range coupling seen across LCMO/YBCO superlattices [47]. Thus our result might be a first indication of the depletion of magnetization in the LCMO layer induced by possible tunneling of the SC order parameter into LCMO through an insulating STO layer.

We now focus on the result of the PNR experiments at 10 K under similar conditions on LCMO (200 Å)/STO (50 Å)/ YBCO (200 Å) where the thickness of the insulating STO is larger at 5 nm. Fig. 4.29 shows the PNR data (spin difference) at 300 K and 10 K. NSLD profile of the sample (upper panel of Fig. 4.29 (a) and (b)) is obtained from 300K PNR data. PNR data at 10 K (lower panel of Fig. 4.29 (a) and (b)) clearly suggests a modification of the magnetization in LCMO layer. A comparison of different

magnetization models and corresponding fits to PNR data are illustrated in the lower panel of Fig. 4.29 (a) and (b). We again observe a magnetic dead layer of thickness $\sim 40 \text{ \AA}$ at LCMO/STO interface. However the magnetization profile beyond this dead layer in LCMO is uniform with $M = 100 \text{ emu/cc}$. We note that the length scale of magnetic dead layer ($\approx 40\text{-}100 \text{ \AA}$) formed at LCMO/STO interface is significantly larger than the interface roughness ($\approx 0.5 \text{ nm}$) obtained from XRR and PNR data.

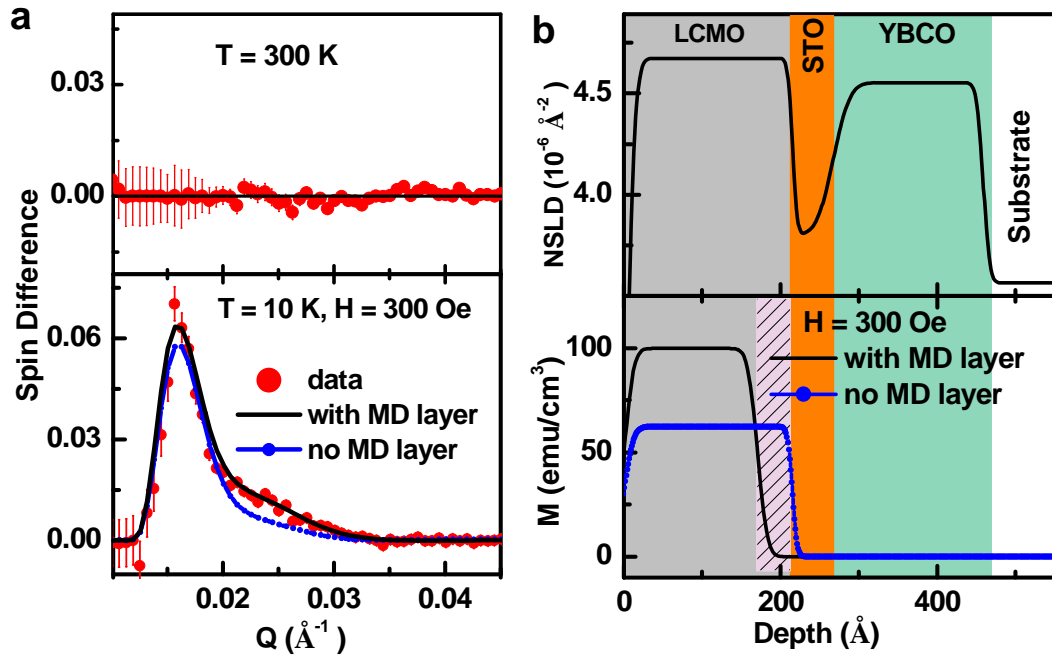


Fig. 4.29: Polarized neutron reflectivity (PNR) measurements and their modeling from the sample with double thickness of insulator layer. (a) Spin difference data from the LCMO (200 \AA)/STO (50 \AA)/ YBCO (200 \AA) trilayer at 300 K (upper panel) and 10 K (lower panel). (b) Nuclear scattering length density (NSLD) depth profile (upper panel) and magnetization depth profile (lower panel) extracted from fitting PNR data at 300 K and 10 K as shown in a. Two magnetization models at 10 K are depicted in the lower panel of (b) and the corresponding fits to PNR data are shown in lower panel of (a).

Further, the average magnetization 120 ± 10 emu/cc of LCMO (300 Å)/STO (25 Å)/ YBCO (300 Å) (taking into account the magnetic dead layer of thickness ~ 100 Å) estimated from PNR data at 10 K is in good agreement with a value of 110 emu/cc obtained from macroscopic SQUID magnetometer (Fig 4.30). This value is well below the saturation magnetization (M_s) ≈ 400 emu/cc observed for single layer LCMO thin films [103]. However the magnetization of LCMO layer highly depends on the thickness of YBCO layers.

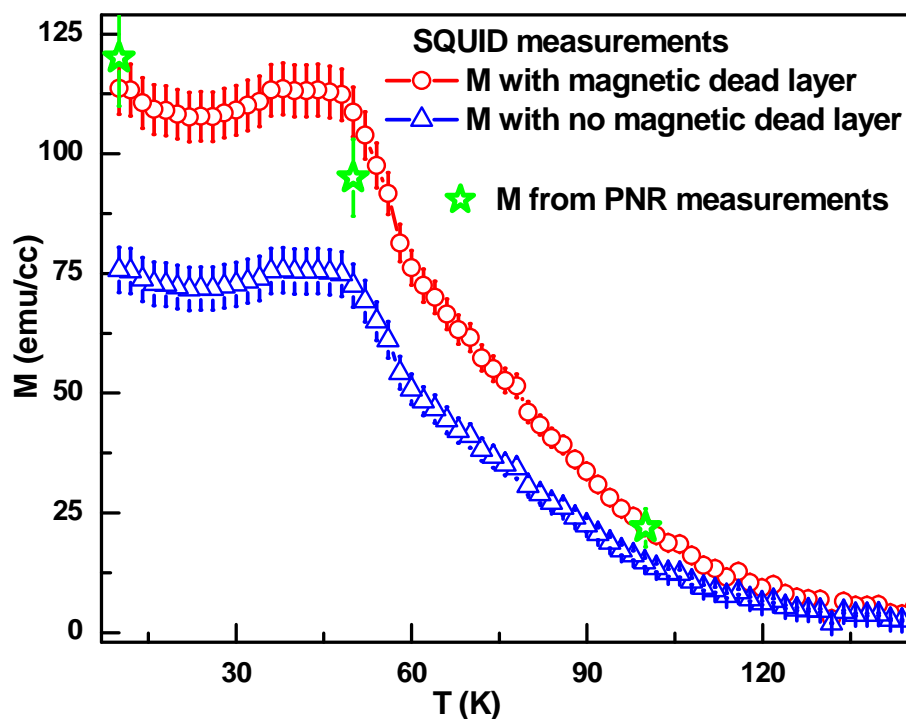


Fig. 4.30: Variation of magnetization (M) as a function of temperature for field cooled condition in a magnetic field of 300 Oe using SQUID (open circle) and PNR (open star) for LCMO (300 Å)/STO (25 Å)/YBCO (300 Å) trilayer.

It is a distinct possibility that the depletion of magnetization in the LCMO layer is caused by superconducting order parameter tunneling into the LCMO layer. Both ferromagnetism and the superconducting state derive their existence from the local density of states. Primarily, presence of superconducting order in LCMO consumes a part of the local density of states at the cost of the strength of the magnetic state. However, SC order persisting over long distances is not expected in the presence of large exchange field, which causes the SC wave function to oscillate and decay rapidly. However, possibility of long range presence of superconducting order for opposite spin cooper pairs is theoretically discussed by Bobkova and Bobkov [104] under non-equilibrium conditions, which compensate the non-zero momentum acquired by the pairs upon their interaction with the exchange field of the ferromagnet.

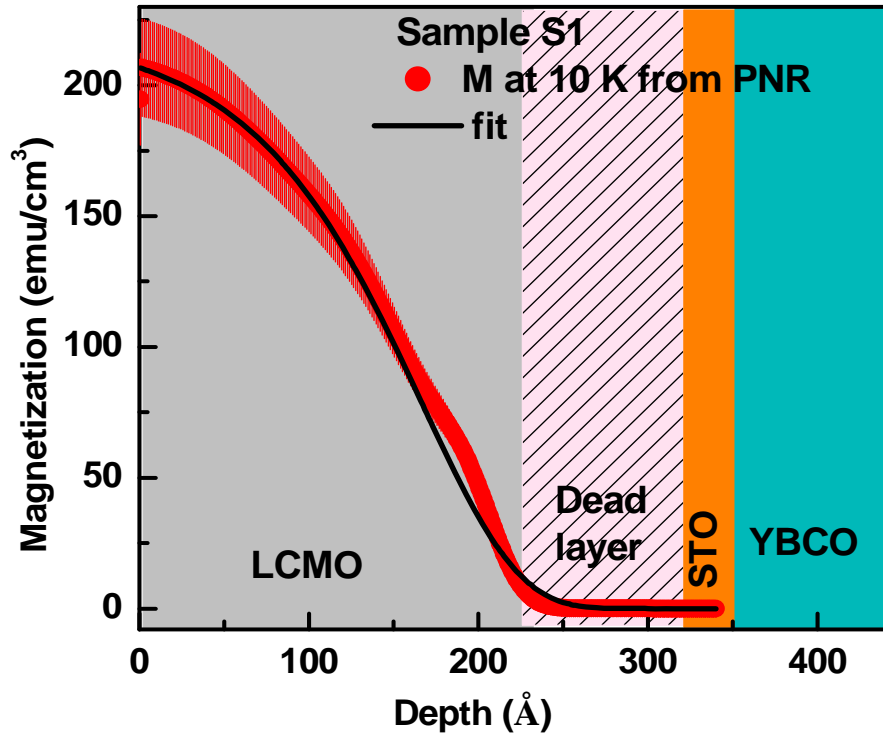


Fig. 4.31: Fitting of magnetization depth profile of $\text{YBa}_2\text{Cu}_3\text{O}_{7-\delta}$ (300 Å)/ SrTiO_3 (25 Å)/ $\text{La}_{2/3}\text{Ca}_{1/3}\text{MnO}_3$ (300 Å) sample at 10 K obtained from PNR data using Eq. 4.1.

We argue that the system prepared under field cooled conditions is also a non-equilibrium state with not only a nanoscopic phase coexistence of FM and charge ordered states but also with ferromagnetic domain walls. We argue that in systems with phase coexistence and domain walls, the random direction and strength of the local in-plane vector potential may also compensate for the net momentum acquired by the pairs on their interaction with the exchange field.

The randomness may result in several length scales in the FM system, which is evident from our attempt to fit the magnetization profile in the LCMO layer obtained from PNR data to the form

$$M(x) = M_0 \left[1 - \exp\left(-\frac{x}{\xi}\right) \right]^\alpha \dots\dots\dots \text{(Eq. 4. 1)}$$

With a large value for $\alpha = 18$ and M_0 is the magnetization sufficiently far from the LCMO/STO interface (Fig. 4.31). The magnetization profile may thus indicate the presence of a large number of length scales in the system.

4.4 Conclusions

Influence of oxygen partial pressure on phase formation and magnetic properties of LSMO ($\text{La}_{2/3}\text{Sr}_{1/3}\text{MnO}_3$) thin films on STO grown by PLD were studied. Strain were calculated by XRD and observed that T_{FM} and H_C increased with strain in LSMO film. Further strain in LSMO films were produced by depositing LSMO films on MgO, STO and YBCO (c- oriented YBCO (100 nm) on STO) substrates. Highly c-oriented LSMO films

are confirmed by XRD patterns. Uniform and non-uniform strains were calculated by XRD peak position and broadening.

We prepared several LCMO/STO/YBCO trilayers using pulsed laser deposition and thoroughly characterized by X-Ray diffraction and X-Ray reflectivity measurements to ascertain the high degree of epitaxy and high quality of interfaces. Some of the samples were chosen for performing Polarized Neutron Reflectivity measurements. We have unambiguously demonstrated that a superconducting YBCO separated from a ferromagnetic LCMO layer by an insulating STO induces magnetic modulation in the LCMO layer. The modulation is in the form of a magnetic dead layer at the LCMO/STO interface below superconducting transition temperature. The depth of the magnetic dead layer is seen to increase when the insulating layer is made thinner. In addition to the magnetic dead layer at LCMO/STO interface we observed non uniform magnetization depth profile in rest of LCMO layer in LCMO/STO/YBCO heterostructure with thinner insulator layer.

Summary and Conclusions

Investigation of the proximity effects in artificially grown ferromagnetic/superconductor heterostructures has been a field of active research for past several decades. Essentially superconductivity and ferromagnetism are antagonistic phenomena. This antagonism has an origin at the microscopic level, i.e., attraction between electrons creates Cooper pairs in a singlet state, whereas exchange interaction that produces ferromagnetism, tends to arrange electron spins parallel to one another. Therefore, when the Zeeman energy of the electrons of a pair in an exchange field I exceeds superconducting gap Δ , the superconducting state is destroyed. For the above reasons, the coexistence of the superconducting and ferromagnetic order parameters is unlikely in a uniform system. However, in nature there are few materials, such as, (RE)Rh₄B₄ and (RE)Mo₆X₈ (RE- rare earth, X- S, Se), RuSrGdCu₂O₈, UGe₂, URhGe etc., in which magnetism and superconductivity coexist. It has been demonstrated that s-wave superconductivity coexists with antiferromagnetism, for example in (RE)Rh₄B₄ and (RE)Mo₆X₈ (RE- rare earth, X- S, Se), and the triplet-pairing superconductivity coexists with ferromagnetism in UGe₂, URhGe, RuSrGdCu₂O₈.

The coexistence of ferromagnetism and superconductivity has been mainly investigated in artificially prepared ferromagnet/superconductor (F/S) heterostructures consisting of alternating F and S layers e.g. Fe/Nb/Fe, Nb/Gd, NbN/Co, YBa₂Cu₃O_x/LaCaMnO₃, YBa₂Cu₃O_x/LaSrMnO₃, etc. In these heterostructures, owing to the proximity effect, a superconducting order parameter can be induced in the F layer; on the other hand, the neighboring pair of F layers can interact with one another via the S layer. Such systems exhibit rich physics: (i) oscillations in superconducting transition temperature with increasing thickness of ferromagnetic layer in three-layer structures (F/S/F), which were

ascribed to the appearance of π -phase superconductivity; (ii) in S/F/S Josephson junctions the relative phase can be π instead of the usual zero (known as π -junction) depending on the thickness of the F layer. Relative strengths of the two order parameters and their interplay can be varied by growing bilayers and trilayers different thickness in controlled manner.

Mainstay of this thesis is the growth of Ferromagnet/Superconductor heterostructures based on metallic (Nb/Gd, Nb/Ni and NbN/NbO/Co) and oxide materials (YBa₂Cu₃O_x/SrTiO₃/La_{2/3}Ca_{1/3}MnO₃). The metallic thin films and FM/SC heterostructures were grown on Si substrates using DC magnetron sputtering; while oxide thin films and heterostructures were grown by pulsed laser deposition. Oxide thin film heterostructures were widely studied, with an objectives to understand if the proximity effect persists even when an insulating layer between superconducting and ferromagnetic layers is introduced. Thin films and heterostructures grown during thesis work were characterized using a host of techniques, such as, scanning electron microscopy; X-ray diffraction; X-ray reflectivity and polarized neutron reflectivity (PNR). The temperature dependent magnetization was measured using the SQUID magnetometer. The temperature dependent electrical transport was measured using four probe method. The main results obtained during the thesis work are summarized as follows:

- Superconducting thin films of Nb and NbN prepared using DC sputtering exhibited T_{SC} of 9 K and 16.2 K respectively.
- The ferromagnetic thin films of Co were prepared and in situ annealed up 800 °C, Change in surface morphology was correlated with magnetic properties. Co films

deposited at room temperature exhibited soft ferromagnetic behaviour whereas those annealed at high temperature exhibited hard ferromagnetic behaviour.

- For Ni films, thickness dependence of the magnetic properties was studied. It is observed that coercive field increases with thickness whereas remanant magnetization decreases with thickness.
- The growth parameters of the Gd films were optimized and it was shown that for films having thickness of 300 Å exhibited Curie temperature ~ 290 K.
- Two series of Fe/Au multilayers were grown: one with varying Fe layer thickness from 30-100 Å keeping Au thickness at 50 Å, and the other with varying Au layer thickness from 50-150 Å keeping Fe thickness at 50 Å. Magnetoresistance and remanant magnetization increase (decrease) with thickness of Fe (Au) film. Annealing of multilayers at 100 °C causes increase in interface roughness and decrease in magnetoresistance.
- Nb/Ni bilayers exhibit anomalous (i.e. two step behaviour) current-voltage characteristics near superconducting transition temperature, which can be correlated to the inhomogeneous superconductivity owing to the domain wall superconductivity.
- Nb/Gd bilayers exhibit two step superconducting transition, reminiscent of domain wall superconductivity in superconducting layers deposited on insulating ferromagnetic substrates [90]. The superconducting region lying right below a domain wall exhibits a higher transition temperature compared to that right below a ferromagnetic domain. Such a conclusion is consistent with (a) the disappearance of the two step behaviour with increasing applied field, b) the observed magnetic

history dependent $R(T)$ transitions and (c) the magnetic hysteresis dependent $V(I)$ characteristics.

- The re-entrant resistance was observed in NbN/NbO/Co trilayer below the superconducting transition. This re-entrant resistance around 1% of the normal state resistance which is compare with similar deposited NbN film. R-T curves are recorded at different probe currents. The observed resistance is found to decrease on increasing the probe currents. A possible reason for re-entrant resistance might be the vortex dynamics in NbN superconducting layer due to the stray fields created by Co layer.
- The magnetic proximity effect in YBCO/STO/LCMO trilayers has been investigated by polarized neutron reflectivity (PNR). PNR measurements were carried out across the both superconducting and ferromagnetic transitions. The suppression of ferromagnetic ordering in a LCMO layer was observed, which is separated by STO insulator from superconductor YBCO. The PNR analys suggested an emergence of a thin magnetic “dead layer” in LCMO adjacent to the STO layer below the superconducting transition temperature of the trilayer. The dead layer is seen even for STO layer as thick as 5 nm, suggesting a possible tunnelling of the superconducting order parameter through the insulating barrier thereby modifying the magnetic state of LCMO.

This thesis work has clearly demonstrated that by inserting an insulator layer between superconducting and ferromagnetic layers, new effects are observed. For example, in case of NbN/NbO/Co, a re-entrant resistance below superconducting transition

temperature is observed, while in case of YBCO/STO/LCMO a magnetic dead layer is observed in LCMO. These results provide further scope for future research in the following areas:

- (i) Investigation of re-entrant superconductivity in superconductor/insulator/ferromagnet heterostructures by varying the thickness of insulating layer, using superconducting layers of different coherence lengths and/or using soft or hard ferromagnetic layers.
- (ii) Investigation of magnetic proximity effect in YBCO/STO/LSMO as a function of STO thickness.
- (iii) Further investigation of domain wall superconductivity in superconductor/ferromagnetic bilayers using different superconducting and ferromagnetic materials.

BIBLIOGRAPHY

- [1] Kamerlingh Onnes, *Commun. Phys. Lab. Univ. Leiden* **12** (1911) 120.
- [2] W. Meissner and R. Ochsenfeld, *Naturwissenschaften* **21** (1933) 787.
- [3] J. Bardeen, L.N. Cooper and J.R. Schrieffer, *Phys. Rev.* **108** (1957) 1175.
- [4] J.G. Bednorz and K.A. Muller, *Z. Phys. B* **64** (1986) 189.
- [5] C. P. Poole, H.A. Farach, R. J. Creswick, *Superconductivity*, Academic Press, San Diego (1995).
- [6] M. K. Wu, J.R. Ashburn, C. J. Torng, P. H. Hor, R. L. Meng, L. Gao, Z. J. Huang, Y. Q. Wang and C. W. Chu, *Phys. Rev. Lett.* **58** (1987) 908.
- [7] E. Kaldis, J. Karpinski, S. Rusiecki, B. Bucher, K. Conder, E. Jilek, *Physica C* **185-189** (1991) 190.
- [8] A. Maignan, C.Martin, V. Hardy, Ch. Simon, M. Hervieu, B. Raveau, *Physica C* **219** (1994) 407.
- [9] J. J. Capponi, J.L. Tholence, C. Chaillout, M. Marezio, P.Bordet, J. Chenavas, S.M. Loureiro, E.V. Antipov, E. Kopnine, M.F. Gorius, M. Nunez-Regueiro, B. Souletie, P. Radaelli, F.G.erhards, *Physica C* **235-240** (1994) 146.
- [10] J. D. Jorgensen, B. W. Veal, A. P. Paulikas, L. J. Nowicki, G. W. Crabtree, H. Clauss and W. K. Kwok, *Phys. Rev. B* **41** (1990) 1863.
- [11] P. Weiss, *J. Phys.* **6** (1907) 661.
- [12] E. C. Stoner, *Philos. Mag.* **15** (1933) 1080.
- [13] R. von Helmolt, J. Wecker, B. Holzapfel, L. Schultz and K. Samwer *Phys. Rev. Lett.* **71** (1993) 2331.

- [14] K. Chahara, T. Ohno, M. Kasai and Y. Kozono *Appl. Phys. Lett.* **63** (1993) 1990.
- [15] E. O. Wollan and W. C. Koehler, *Phys. Rev.* **100** (1955) 545.
- [16]
- [17] L. N. Bulaevski, A. I. Buzdin, M. L. Kubic, and S. V. Panjukov, *Adv. phys.* **34** (1985) 175.
- [18] A. I. Buzdin, *Rev. Mod. Phys.* **77** (2005) 935.
- [19] N. R. Werthamer, *Phys Revs* **132** (1963) 2440.
- [20] G. Deutscher and P. G. de Gennes: *Superconductivity*, ed. R. D. Parks (Marcel Dekker, New York, **1969**).
- [21] A. I. Buzdin and M. Y. Kuprianov, *JETP Lett.*, **52** (1990) 487.
- [22] J. S. Jiang, D. Davidovic', D. H. Reich, and C. L. Chien, *Phys. Rev. Lett.* **74** (1995) 314.
- [23] V. Mercaldo, C. Affanasio, C. Coccorese, L. Maritato, S. L. Prischepa, and M. Salvato, *Phys. Rev. B* **53** (1996) 14040.
- [24] Y. Obi, M. Ikebe, T. Kubo, and H. Fujimori, *Physica C* **317-318** (1999) 149.
- [25] A. S. Sidorenko,, V. I. Zdravkov, A. A. Prepelitsa, C. Helbig, Y. Luo, S. Gsell, M. Schreck, S. Klimm, S. Horn, L. R. Tagirov, and R. Tidecks, *Ann. Phys.* **12** (2003) 37.
- [26] Th. Mühge, N. N. Garif'yanov, Yu. V. Goryunov, G. G. Khaliullin, L. R. Tagirov, K. Westerholt, I. A. Garifullin, and H. Zabel, *Phys. Rev. Lett.* **77** (1996) 1857.
- [27] A. Y. Garifullin, *J. Magn. Magn. Mater*, **240** (2002) 571.

- [28] L. Lazar, K. Westerholt, H. Zabel, L. R. Tagirov, Yu. V. Goryunov, N. N. Garifyanov, and I. A. Garifullin, *Phys. Rev. B* **61** (2000) 3711.
- [29] A. I. Buzdin, A. V. Vedyayev, and N. V. Ryzhanova, *Europhys. Lett.* **48** (1999) 686.
- [30] L. R. Tagirov, *Phys. Rev. Lett.* **83** (1999) 2058.
- [31] J. J. Hauser, *Phys. Rev. Lett.* **23** (1969) 374.
- [32] C. A. R. Sá de Melo, *Phys. Rev. Lett.* **79**, 1933 (1997).
- [33] S. Soltan, Albrecht, J. and H. –U. Habermeier, *Phys. Rev. B* **70** (2004) 144517.
- [34] Z. Sefrioui, et al. *Phys. Rev. B* **67** (2003) 214511.
- [35] P. P. Deen, *Phys. Rev. B* **74** (2006) 224414.
- [36] J. Chakhalian, et al., *Nature Phys.* **2**, 244-248 (2006).
- [37] V. Peña, Z. Sefrioui, D. Arias, C. Leon, J. Santamaria, J. L. Martinez, S. G. E. Velthuis, and A. Hoffmann, *Phys. Rev. Lett.* **94** (2005) 057002.
- [38] Takahashi, I. Imamura, and S. Maekawa, *Phys. Rev. Lett.* **82** (1999) 3911.
- [39] J. Hoppler, J. Stahn, Ch. Niedermayer, V. K. Malik, H. Bouyanfif, A. J. Drew, M. Rossle, A. Buzdin, G. Cristiani, H. U. Habermeier, B. Keimer, C. Bernhard, *Nature Mater.* **8** (2009) 315.
- [40] M. A. Uribe-Laverde et al, *Phys. Rev. B* **87** (2013) 115105.
- [41] D. K. Satapathy et al, *Phys. Rev. Lett.* **108** (2012) 197201.
- [42] Y.-h. Liu, X.-d. Ma, and L.-M. Mei, *Phys. Rev. B* **45** (1992) 10459.
- [43] Kowalewski, M. et al. , *J. Appl. Phys.* **87** (2000) 5732.
- [44] A. Hoffmann, et al., *Phys. Rev. B.* **72** (2005) 140407(R).
- [45] J. Stahn et al, *Phys. Rev. B* **71** (2005) 140509.

- [46] M. Varela, A. R. Lupini, S. J. Pennycook, Z. Sefrioui, J. Santamaria, *Solid-State Electron.* **47** (2003) 2245.
- [47] V. Pena, Z. Sefrioui, D. Arias, C. Leon, J. Santamaria, M. Varela and S. J. Pennycook, *Phys. Rev. B* **69** (2004) 224502.
- [48] T. Holden, H.-U. Habermeier, G. Cristiani, A. Golnik, A. Boris, A. Pimenov, J. Humlíček, O. I. Lebedev, G. Van Tendeloo, B. Keimer, and C. Bernhard, *Phys. Rev. B* **69** (2004) 064505.
- [49] I. F. Lyuksyutov and V. L. Pokrovsky, *Advances in Physics* 54 (2005) 67.
- [50] Yu. A. Izyumov, Yu. N. Proshin, M. G. Khusainov, *Physics – Uspekhi* **45** (2002) 109.
- [51] A. Yu. Aladyshkin, A. V. Silhanek, W. Gillijns, and V. V. Moshchalkov, *Supercond. Sci. Technol.* **22** (2009) 053001.
- [52] S. Singh, S. Basu, C.L. Prajapat, M. Gupta, A. K. Poswal, D. Bhattacharya, *Thin Solid Films*, **550** (2013) 326.
- [53] C. L. Prajapat, G. Yashwant, M. R. Singh, S. K. Gupta, G. Ravikumar, *J. Supercond. Nov. Magn.* **25** (2012) 1455.
- [54] P. Sigmund, *Phys. Rev.* **184** (1969) 383.
- [55] L. I. Maissel and R. Glang, *Handbook of thin film technology*, McGrawHill Book Company, (1970).
- [56] John A. Thornton, *J. Vac. Sci. Technol.* **15** (1978) 171.
- [57] Donald M. Mattox, *Hand book of physical vapor deposition (PVD) processing*, Noyes Publication (1998).
- [58] F Hartmut, editor. Band 1, *Plasmaphysik – Plasmadiagnostik – Analytik*.

- Vakuumbeschichtung. VDI-Verlag, Dusseldorf, 1995. ISBN 3-18-401313-6.*
- [59] Y. Tamamura and H. Tawara, *Atomic data and nuclear data tables* **62** (1996) 149.
- [60] D. B. Chrisey and G. K. Hubler, *Pulsed Laser Deposition of Thin Films*, John Wiley & Sons, New York (1994).
- [61] P. R. Willmott and J. R. Huber, *Rev. Mod. Phys.* **72** (2000) 315.
- [62] M. N. R. Ashfold, F. Claeysens, G.M. Fuge, S. Henley, *Chem. Soc. Rev.*, **33** (2004), 23.
- [63] D. Dijkamp and T. Venkatesan, X. D. Wu, S. A. Shaheen, N. Jisrawi, Y. H. Minlee, W. L. Mclean, and M. Croft, *Appl. Phys. Lett.* **51**(1987) 619.
- [64] B S H Pang, R I Tomov and M G Blamire, *Supercond. Sci. Technol.* **17** (2004) 624.
- [65] H.-U Habermeier and G. Cristiani, R. K. Kremer, O. Lebedev, G. Van Tendeloo, *Physica C* **364-365** (2001) 298.
- [66] Y. Zhang, H. Gu, and S. Iijima, *Appl. Phys. Lett.* **73**, 3827 (1998).
- [67] D.B. Geohegan, A.A. Puretzky, and D.L. Rader, *Appl. Phys. Lett.* **74** (1999) 3788.
- [68] J. T. Cheung, I.M. Gergis, J. James and R.E. DeWames, *Appl. Phys. Lett.* **60** (1992) 3180.
- [69] J. A. Greer and H.J. Van Hook, *Mater. Res. Soc. Symp. Proc.* **191** (1990) 171.
- [70] B. D. Culty, *Elements of x-ray diffraction*, Wesley Publishing Company (1978).
- [71] M. R. Fitzsimmons and C. Majkrzak, *Modern Techniques for Characterizing Magnetic Materials*, Springer, New York, (2005).
- [72] S. Singh, S. Basu, M. Gupta, C. F. Majkrzak, and P. A. Kienzle, *Phys Rev. B* **81**, (2010) 235413.

- [73] G.P. Felcher, R.O. Hilleke, R.K. Crawford, J. Haumann, R. Kleb, and G. Ostrowski, *Rev. Sci. Instrum.* **58** (1987) 609.
- [74] H. Zabel, *Festkörperprobleme*, **30** (1990) 197.
- [75] H. Dosch, *Physica B*, **192** (1993) 163.
- [76] J.F. Ankner and G.P. Felcher, *JMMM* **200** (1999)741.
- [77] L. G., Parratt, *Phys. Rev.* **95**, 359-369 (1954).
- [78] B. Voutou and Eleni-Chrysanthi Stefanaki, *Physics of advanced materials winter school* (2008).
- [79] Keithley, *Low level measurement handbook*, 6th edition, www.keithley.com.
- [80] B. D. Josephson, *Phys. Lett.* **1** (1962) 251.
- [81] Manual, MPMS5, *Quantum Design* (1992).
- [82] G. I. Frolov, V. S. Zhigalov, and V. K. Maltsev, *Physics of the Solid State* **42** (2000) 334.
- [83] E.F. Kneller, F.E. Luborsky, *J. Appl. Phys.* **34** (1963) 656.
- [84] X. Batlle, M. Garcia del Muro, J. Tejada, H. Pfeiffer, P. Goand, E. Sinn, *J. Appl. Phys.* **74** (1993) 3333.
- [85] J. Yang, Y. Huang and K. Xu, *Surf. Coat. Technol.* **201** (2007) 5574.
- [86] T. Nishimura, J. Takeda, Y. Asami, Y. Hoshino, Y. Kido, *Japan Surface Science* **588** (2001) 71.
- [87] P. Kumar, M. G. Krishana and A. K. Bhattacharya, *Bull. Mater. Sci.* **32** (2009) 263.
- [88] Y. Yamada, M. Okada, P. Jin, M. Tazawa, and K. Yoshimura, *Thin Solid Films* **459** (2004) 191.
- [89] D. Stamopoulos, M. Pissas, and E. Manios, *Phys. Rev. B* **71** (2005) 014522.

- [90] S. P. Chockalingam, M. Chand, J. Jesudasan, V. Tripathi, and P. Raychaudhuri, *Phys. Rev. B* **77** (2008) 214503.
- [91] D. H. Ryan, A. Michels, F. Dobrich, R. Birringer, Z. Yamani, and J. M. Cadogan, *Phys. Rev. B* **87** (2013) 064408.
- [92] Z. Yang, M. Lange, A. Volodin, R. Szymczak and V. V. Moshchalkov, *Nature* **3** (2004) 798.
- [93] R. Werner, A. Yu. Aladyshkin, S. Gu'enen, J. Fritzsche, I. M. Nefedov, V. V. Moshchalkov, R. Kleiner, and D. Koelle, *Phys. Rev. B* **84** (2011) 020505(R).
- [94] Z. Yang and V. V. Moshchalkov, *J. Appl. Phys.* **109** (2011) 083908.
- [95] A. Yu. Rusanov, M. Hesselberth, J. Aarts, and A. I. Buzdin, *Phys. Rev. Lett.* **93** (2004) 057002.
- [96] A. I. Buzdin, L. N. Bulaevskii, and S. V. Panyukov, *Sov. Phys. JETP* **60**, 174 (1984).
- [97] I. F. Lyuksyutov, and Pokrovsky, *Phys Rev. Lett.* **81** (1998) 2344.
- [98] D. E. Feldman, I. F. Lyuksyutov, V. L. Pokrovsky, and V. M. Vinokur, *Europhys. Lett.*, **51**, 110 (2000).
- [99] C. Thiele, K. Dörr, O. Bilani, J. Rödel, and L. Schultz, *Phys. Rev. B* **75** (2007) 054408.
- [100] D. Böttcher and J. Henk, *J. Phys.: Condens. Matter* **25** (2013) 136005.
- [101] Press, W. H., Flannery, B. P., Teukolsky, S. A. & Vetterling, W. T. *Numerical Recipes in Fortran: The Art of Scientific Computation*, 2nd ed. (Cambridge University Press, Cambridge, 1992).

- [102] G. Campillo, A. Berger, J. Osorio, J. E. Pearson, S. D. Bader, E. Baca, and P. Prieto, *J. Magn. Magn. Mater.* **237** (2001) 61.
- [103] I. V. Bobkova and A. M. Bobkov, *Phys. Rev. Lett.* **108** (2012) 197002.